Micromechanics and Plasticity in Laves Phases and Nanomechanical Testing Under Extreme Conditions

Von der Fakultät für Georessourcen und Materialtechnik der
Rheinisch-Westfälischen Technischen Hochschule Aachen

zur Erlangung des akademischen Grades eines

Doktors der Ingenieurwissenschaften

genehmigte Dissertation

vorgelegt von

M. Sc. Christoffer Zehnder

Berichtende: **Univ.-Prof. Dr. Sandra Korte-Kerzel**
Univ.-Prof. Dr. Jochen Schneider

Tag der mündlichen Prüfung: 27.10.2023

D 82 (Diss. RWTH Aachen University,2023)

- **Zehnder, C.,** Czerwinski, K., Molodov, K. D., Sandlöbes-Haut S., Gibson, J. S. K. L, Korte-Kerzel, S., *Plastic deformation of single crystalline C14 Mg2Ca Laves phase at room temperature. Materials Science and Engineering*: A 759, 2019, pp. 754-761.

- **Zehnder, C**., Pelzer, J.-N., Gibson, J. S. K. L, Mönke, D., Korte-Kerzel, S., *Non-Newtonian Flow to the Theoretical Strength of Glasses via Impact Nanoindentation at Room Temperature*, Scientific Reports 7, 2017, Article number: 17618

- Gibson, S.K.L., Schröders, S., **Zehnder, C.**, Korte-Kerzel, S., *On extracting mechanical properties from nanoindentation at temperatures up to 1000 °C*, Extreme mechanics Letters 17, 2017, p. 43- 49

- Freund, M., Andre, D., **Zehnder, C.,** Rempel, H., Gerber, D., *Plastic deformation of the Mg2Ca C14-Laves phase from 50 – 250 °C RT C36/C15*, Materialia 20, December 2021, 101237

,,Man überschätzt wohl leicht das eigene Wirken und Tun in seiner

Wichtigkeit gegenüber dem, was man nur durch andere geworden ist.“

D. Bonhoeffer

TABLE OF CONTENTS

DANKSAGUNG

Wie es das oben genannte Zitat bereits sagt, ist diese Arbeit letztendlich auch ein Resultat der Bemühungen vieler Einzelner, denen ich meinen tiefsten Dank schulde. An erster Stelle sei hier Prof. Dr. Sandra Korte-Kerzel genannt. Abgesehen von der Überlassung dieses spannenden Themas gilt mein großer Dank ihrer außerordentlichen Betreuung meiner Arbeit. Neben der ausgezeichneten fachlichen Betreuung habe ich hier auch immer ein offenes Ohr für persönliche Anliegen gefunden.

Mein nächster Dank geht an Dr. James Gibson. Bedanken möchte ich mich für die unzähligen Stunden, die er zusammen mit mir zusammen verbracht hat, wenn die Nanoindenter wieder ihren eigenen Kopf hatten oder sich die Formel für das Aktivierungsvolumen nicht auflöste. Nicht minder dankbar bin ich Dr. Steffi Sandlöbes für ihre unermüdliche Hilfe bei den TEM Untersuchungen und beim Atome zählen und ihre vielen Gespräche über alles Mögliche. Beiden sei auch ganz herzlich gedankt für alle Korrekturarbeiten an meinen Veröffentlichungen.

Ohne die technische Abteilung hier am IMM wäre kein einziges der hier publizierten Experimente zustande gekommen. Ganz herzlicher Dank geht deshalb an David Beckers, Thomas Burlet, Arndt Ziemons und (stellvertretend für die gesamte Werkstatt) Detlef Fuchs für die Zeit die ihr investiert habt. Jedes Mal, wenn ich Doktoranden von anderen Einrichtungen erzählt habe, wie schnell ihr arbeitet habe ich nur erstaunte Blicke geerntet – das ist sicher nicht selbstverständlich!

Als nächstes sind meine studentischen Aushilfskräfte, Bachelor- und Masterarbeiter zu nennen die mir bei vielen experimentellen Aufgaben unter die Arme gegriffen haben und oft hilfreiche Ideen und Hinweise übrig hatten.

Weiterer Dank geht an die Kollegen für viele unvergessliche Stunden während und neben der Arbeitszeit. Angefangen von hilfreichen Diskussionen über Forschungsergebnisse und -probleme über Scherze, wenn unsere Nanoindenter wieder einen schlechten Tag hatten bis hin zu Mario Kart und James Bond – für jede Situation war etwas dabei. Besonderer Dank gilt hier meinen Bürokollegen Dr. Mehran Afshar und Dr. Sebastian Schröders für die Freundschaft und ständige Hilfsbereitschaft auch über die Arbeitszeit hinaus.

Ohne die ständige Hilfe meiner Freunde und ganz besonders meiner Familie wäre ich sicher nicht an diesem Punkt angekommen. Meinen Eltern möchte ich danken für all die Jahre, die sie mich ermutigt

und unterstützt haben und das Fundament, das sie mir so mit auf den Weg gegeben haben. Meinem Bruder danke ich für all die Gespräche über verschiedenste Themen und sein stets offenes Ohr und hilfreiche Meinung – ich bin froh ihn an meiner Seite zu wissen. Kürzer mit auf dem Weg aber sicher nicht weniger hilfreich waren meine Schwiegereltern, die immer eine helfende Hand übrighatten.

Eine Person hat diese Arbeit wohl am meisten mitgetragen: ich danke meiner wundervollen Frau Julia, die in dieser Zeit immer Rücken an Rücken mit mir zusammengestanden hat. Mit ihrer ruhigen und zuversichtlichen Art hat sie mir immer den nötigen Ruhepol gegeben, den ich gebraucht habe um bis hier hin zu kommen. Die schweren Zeiten der vergangenen Jahre hätte ich ohne sie und ihre unvergleichlich liebevolle und starke Art sicher nicht durchgestanden – wir haben es zusammen hierher geschafft! Letztendlich möchte ich noch meinen beiden Kindern danken, die für mich die zwei wunderbarsten Wesen auf dieser Welt sind und mich immer wieder in Staunen versetzen.

ABSTRACT

Nanomechanical test methods offer significant advantages compared to macroscopic test methods: next to the possibility to test materials which are only present in small sizes (e.g., precipitations) the indentation size effect plays an important role: due to a change of deformation mechanism, nanomechanical testing can be used to introduce plastic deformation into materials which are brittle at room temperature. The mechanical and elastic properties can then furthermore be used in simulations or models to predict complex, macroscopic systems where the tested materials are present, e.g., an Mg alloy with small precipitations of brittle Laves phases inside.

Next to these advantages, there are of course as well limitations, one of them being the scarcity of nanomechanical test methods besides the standard quasi-static nanoindentation or micropillar compression experiments. The first part of this thesis therefore aims to extend the accessible region of nanoindentation into two directions, which were not fully usable up to now: high temperatures and high strain rates. The second part of this thesis then applies nanomechanical test methods on a specific material group, Laves phases in the Mg-Al-Ca system. By means of (HT)-nanoindentation and (HT)-micropillar compression experiments in conjunction with electron microscopy (SE / EBSD) and atomic force microscopy (AFM) it was possible to study the effect of temperature as well as composition on the deformation mechanism of Laves phases, making an important step towards the use of light-weight Mg alloys in motor blocks.

For the first part, a super alloy was used to perform nanoindentation experiments up to a temperature of 1000 °C. This is the first time that nanoindentation was used at these high temperatures. The main difficulties with this kind of experiments are the wear of the indenter tip as well as the massive amount of creep deformation even in very short test periods. Next to high temperatures, the high strain rate regime is as well difficult to access in nanoindentation experiments. In this thesis, a pendulum-based nanoindentation system was used, making it possible to ensure a sufficiently high accuracy of the data acquisition. Different glass materials ranging from the most anomalous (densification) glass, fused silica, to the most normal (shear deformation) glass system, a bulk metallic glass (BMG) were tested. It could be proven for the first time that non-Newtonian behaviour exists at room temperatures showing a linear decrease in viscosity with strain rate. This results that after the hardness increases for low strain rates with increasing strain rate, it then levels off to a constant hardness value. Finally, it could be shown that

this hardness value is around 70 – 80 % of their theoretical hardness for all tested glass materials despite their different deformation behaviour.

In the second part, the deformation behaviour of Laves phases in the Mg-Al-Ca system was investigated. The Mg-Al-Ca alloys show a significantly increased creep strength compared to standard Mg-alloys which is based on an intermetallic skeleton precipitating inside the alloy. Understanding the deformation behaviour of these intermetallic compounds would help to modify the existing Mg-Al-Ca alloys to be specially aligned for creep resistance.

At room temperature, nanoindentation was used to determine the frequency of activation of different slip systems in the hexagonal C14 Mg2Ca Laves phase. These values were compared to a geometrical study to determine the likeliness of a slip plane to be activated and then set in correlation to critical resolved shear stresses (CRSS) from micropillar compression experiments. Both data sets showed excellent correlation.

CRSS values as well as activation of slip system is measured up to 250 °C. Next to this, one can observe a decrease in serrated yielding as well as a decrease of clearly indexable slip lines with increasing temperature. This is correlated to the occurrence of a Portevin-le-Chatelier (PLC) effect. At low temperatures, dislocation movement is controlled by obstacles, e.g. solute atoms. Dislocation movement therefore is taking place in jumps resulting in large slip steps on the surface. With increasing temperature, dislocations are more likely to overcome obstacles due to thermal activation, so that deformation becomes more homogeneous.

Finally, the effect of composition was investigated by comparing the deformation behaviour of (Mg,Al)2Ca (C36), Mg2Ca (C14) and Al2Ca (C15) phase. A change in the occurrence of serrated yielding and localization of slip planes is discussed behind the background of off-stoichiometry in the C36 phase. For the cubic C15 phase, the activated slip systems are analyzed.

KURZZUSAMMENFASSUNG

Nanomechanische Test Methoden bieten deutliche Vorteile gegenüber makroskopischen Testverfahren: neben der offensichtlichen Möglichkeit Materialien zu testen, die nur in kleinen Größen vorkommen bietet der Indentation Size Effect (ISE) die Möglichkeit Materialien zu verformen, die in makroskopischer Form sich spröder verhält. Die dadurch gewonnen elastischen und mechanischen Konstanten können wiederum verwendet werden um Simulationen und Modelle zu erstellen, welche die mechanischen Eigenschaften komplexer Systeme vorhersagen können, z.B. Mg-Legierungen in denen kleine, intermetallische Phasen vorkommen.

Neben diesen Vorteilen gibt es natürlich auch Nachteile, unter anderem die geringe Verfügbarkeit von Testmethoden, die über die Standard-Verfahren (quasi-statische Indentierung, Mikrosäulen Kompression) hinausgehen. Der erste Teil dieser Arbeit beschäftigt sich demnach damit die Grenzen der nanomechanischen Testverfahren zu auszuloten: hohe Temperaturen und hohe Dehnraten. In einem zweiten Teil beschäftigt sich diese Arbeit mit der Anwendung dieser Verfahren auf Laves Phasen im Mg-Al-Ca System. Mittels (HT)-Nanoindentierung und (HT)-Mikrosäulen Kompression sowie Elektronenmikroskopie (EBSD / SE) und Rastkraftmikroskopie (AFM) war es möglich den Effekt von Temperature und Zusammensetzung auf die Verformungmechanismen von Laves Phasen zu untersuchen, was ein wichtiger Schritt in die Richtung ist, Leichtmetall Mg Legierungen industriell einzusetzen.

Für den ersten Teil der Arbeit wurde zum ersten Mal Nanoindentierung bis zu einer Temperatur von 1000 °C an einer Superlegierung durchgeführt. Die größten Schwierigkeiten bei diesen Versuchen waren die hohe Korrosion der Indenterspitze bei solch hohen Temperaturen sowie der große Anteil an Kriechverformung, selbst bei geringer Testdauer. Neben hohen Temperaturen ist es außerdem schwierig den Bereich der hohen Dehnraten in der Nanoindentierung zu erreichen. In dieser Arbeit wurde ein Indentersystem, das den Aufbau eines Pendels verwendet, so modifiziert, dass die Weg-Zeit-Kurve mit ausreichender Genauigkeit aufgenommen werden konnte um die Versuchsreihen auswerten zu können. Verschiedene Glas Systeme, von dem am meisten anormalem (Verdichtung) System, Fused Silica, bis hin zum am stärksten normal (Scherverformung) verformendem System, einem metallischen Glas (BMG) wurden getestet. Zum ersten Mal konnte Nicht-Newtonsches Verhalten bei Raumtemperatur nachgewiesen werden. Hierfür konnte gezeigt werden, dass die Viskosität linear abfällt, sodass bei kleinen Dehnraten die Festigkeit linear mit der Dehnrate ansteigt während sie bei hohen Dehnraten

konstant bleibt. Schließlich konnte gezeigt werden, dass die konstante Festigkeit bei hohen Dehnraten bei jedem Glas System ~ 70 – 80 % der theoretischen Festigkeit beträgt, trotz der stark unterschiedlichen Verformungsmechanismen.

Im zweiten Teil der Arbeit wurde des Verformungsverhalten von Laves Phasen im Mg-Al-Ca System untersucht. Mg-Al-Ca Legierungen bieten stark erhöhte Kriechfestigkeiten im Vergleich zu standardmäßigen Mg-Legierungen aufgrund eines intermetallischen Skelets innerhalb der Mg-Matrix. Es ist ein wichtiger Schritt das Verformungsverhalten dieses intermetallischen Skelets zu verstehen um diese Legierungen industriell anwenden zu können.

Bei Raumtemperatur wurde Nanoindentierung verwendet um statistisch sinnvoll die Aktivierung von Gleitsystemen der hexagonalen Mg2Ca Laves Phase zu bestimmen. Diese Werte wurden mit einer geometrischen Studie vergleichen um den Widerstand ein bestimmtes Gleitsystem zu aktivieren zu bestimmen und dann mit Kritischen Schubspannungen (CRSS) aus Mikrosäulen Kompressionsversuchen in Verbindung zu setzen. Beide Datensätze zeigen eine gute Korrelation.

CRSS Werte sowie die Aktivierung von Gleitsystemen wurde daraufhin bis zu Temperaturen von 250 °C durchgeführt. Weiterhin wurde beobachtet, dass Stufen in der Last-Weg-Kurve sowie der Anteil an deutlich sichtbaren Gleitstufen auf der Oberfläche mit höheren Temperaturen zurück geht. Dies wurde mit dem Auftreten des Portevin-le-Chatelier (PLC) Effekt in Verbindung gebracht. Bei niedrigen Temperaturen ist die Versetzungsbewegung von Hindernissen bestimmt, z.B. Fremdatome. Versetzungsbewegung tritt daher in Schüben auf, wann immer sich eine Versetzung wieder losreisen kann, sodass Sprüngen in der Kraft-Weg-Kurve sichtbar sind und es zu hohen Gleitstufen auf der Oberfläche kommt. Mit höheren Temperaturen wird es für die Versetzungen durch thermische Aktivierung leichter sich von den Fremdatomen loszureißen und damit wird die Verformung gleichmäßiger.

Schließlich wurde der Effekt der Zusammensetzung untersucht, indem das Verformungsverhalten von (Mg,Al)2Ca (C36), Mg2Ca (C14) und Al2Ca (C15) untersucht wurde. Die C36 Phase zeigte sich verändernde Anteile von Gleitstufen und PLC Effekt, dies wurde vor dem Hintergrund von nicht-stöchiometrischer Zusammensetzung diskutiert. Die aktivierten Gleitsysteme der kubischen C15 Phase wurden bestimmt.

LIST OF FIGURES

LIST OF ABBREVIATION

HT	High temperature
RT	Room temperature
CRSS	Critical resolved shear stress
FIB	Focused ion beam
AFM	Atomic force microscopy
SEM	Scanning electron microscopy
TEM	Transmission electron microscopy
EBSD	Electron backscatter diffraction
SE	Secondary electrons
Ω_{exp}	Experimentally measured activation of a certain slip system
Ω_{theo}	Theoretically determined activation of a certain slip system (geometrical analysis)
Δ	Difference between Ω_{exp} and Ω_{theo}
PLC	Portevin-le-Chatelier
(n)SRS	(negative) Strain rate sensitivity
SFE	Stacking fault energy
DSA	Dynamic strain ageing
DAF	Diamond area function

1 STRUCTURE OF THE RESEARCH PAPERS AND CONTRIBUTION OF THE AUTHOR

This work comprises four research papers:

1. **Zehnder, C.,** Czerwinski, K., Molodov, K. D., Sandlöbes-Haut S., Gibson, J. S. K. L, Korte-Kerzel, S., *Plastic deformation of single crystalline C14 Mg2Ca Laves phase at room temperature. Materials Science and Engineering*: A 759, 2019, pp. 754-761.
2. **Zehnder, C**., Pelzer, J.-N., Gibson, J. S. K. L, Mönke, D., Korte-Kerzel, S., *Non-Newtonian Flow to the Theoretical Strength of Glasses via Impact Nanoindentation at Room Temperature*, Scientific Reports 7, 2017, Article number: 17618
3. Gibson, S.K.L., Schröders, S., **Zehnder, C.**, Korte-Kerzel, S., *On extracting mechanical properties from nanoindentation at temperatures up to 1000 °C*, Extreme mechanics Letters 17, 2017, p. 43-49
4. Freund, M., Andre, D., **Zehnder, C.,** Rempel, H., Gerber, D., *Plastic deformation of the Mg2Ca C14-Laves phase from 50 – 250 °C RT C36/C15*, Materialia 20, December 2021, 101237

Furthermore, a fifth paper is in preparation which investigates the influence of the composition on the deformation behaviour in the $(Mg,Al)_2Ca$ system (C36 / C14 / C15 phases)

Paper Nr. 1 investigates the room temperature deformation mechanism of the C14 Laves phase Mg_2Ca. As this is the first of the paper focusing on mechanical properties of the Mg-Al-Ca system, emphasis was set on connected nanoindentation and micropillar compression experiments. By restraining to the RT behaviour of only the C14 phase, it was possible to investigate the orientation dependence in small steps. The focus of this paper therefore lies on investigating the statistics of slip systems activation in the C14 phase at room temperature and their CRSS values.

Paper Nr. 2 adds high strain rates to the investigated field of mechanical testing on the nano-scale. By combining different indentation as well as micropillar compression methods, several order of magnitude of strain rates were tested and set into comparison. Since glasses show a fundamental change of deformation mechanism with increasing strain rate, different glasses with varying portion of densification and shear where investigated and analysed regarding their dominant deformation mechanism.

Paper Nr. 3 aims on extending the maximum temperature up to which nanoindentation experiments can be conducted to 1000 °C. While this temperature is unreasonable to be applicate to the Laves phases tested in this study, it will be important when these findings are transferred to Laves phases having a higher melting point, e.g. in the Fe system.

Paper Nr. 4 extended the results of paper Nr. 2 to temperatures up to 250 °C. In order to keep the size of the data set in a reasonable order, only three orientation have been tested. Next to the change in slip systems activation and CRSS values with increasing temperature, the strain rate sensitivity (SRS), the activation volume and the occurrence of planar slip have been investigated for this temperature range.

Finally, paper Nr. 5 (still under construction) investigates the deformation mechanism of the other two Laves phases C15 and C36 in the Mg-Al-Ca system. As the C36 phase can form with different Mg/Al ratios, three orientations were investigated as well. Due to the large amount of possible composition-orientation combinations, this paper focused on nanoindentation and did not include micropillar compression experiments. The results span therefore from the statistics of slip system activation in the C36 and the C15 phase to the occurrence of a PLC effect and the SRS for a change in composition rather than in temperature.

Contribution of the author to the publications listed above

Paper 1 and 2: The candidate conceptualized the experimental setup and test structure. He performed most of the experimental work. Analysis was performed by the candidate. Furthermore, the candidate wrote the script and amended the co-author`s and reviewer`s comments.

Paper 3: The candidate conceptualized the experimental setup and performed the experimental work together with S. Schröder.

Paper 4: The candidate conceptualized the experimental setup and test structure. He performed most of the experimental work. The experimental analysis as well as the embedding of the work into the literature was performed by the candidate. Furthermore, the candidate wrote a first draft of the script.

2 MOTIVATION AND RESEARCH QUESTIONS

The aim of this work is to investigate the deformation mechanisms of brittle materials at low homologous temperatures (< 70 % of the melting point). This was investigated on two examples: glasses at room temperature and Laves phases in the Mg-Al-Ca system in the temperature range between RT and 250 °C. Special focus lies on the activation of slip systems, the determination of CRSS values and dislocation structures as well as deformation mode (e.g. uniformity of deformation, serrated flow and activation volume) in the Laves phases. For this, samples containing all three Laves phases, the hexagonal C14 (Mg_2Ca) and C36 ($(Mg,Al)_2Ca$) and the cubic C15 (Al_2Ca) were produced and (in-situ) nanoindentation and micropillar compression experiments were conducted. Electron microscopy and AFM were used to analyse the results. The results are discussed against the background of the crystal structure. The exact research questions are the following:

- **How can nanomechanical test methods be used to investigate the deformation mechanisms of brittle materials?** Nanoindentation uses the size effect as well as a confining pressure to introduce mechanical deformation in materials which show brittle failure in macroscopic testing otherwise. Besides the standard methods of nanoindentation (Strain Rate Jump Tests (SRJ), Constant Strain Rate (CSR) test), which are well understood, there are areas of nanoindentation which are less well investigated. These comprise the high strain rate testing (impact) as well as high temperature (HT) testing of nanoindentation. These methods are investigated in the paper 2 and 3.
- **What are the room temperature deformation mechanism of the C14 Laves phase?** This topic includes the activation and CRSS values of different slip systems and in how far these values can be correlated to the atomic structure. To investigate this, nanoindentation was used to get a statistical analysis of the activation of different slip systems. Micropillar compression offered the possibility to determine the respective CRSS values. Especially the basal slip system is of interest and a possible correlation of the syncroshear mechanism to the basal (and other) planes. Though the exact determination of all possible Burgers vectors would comprise a complete thesis itself, exemplary Burgers vectors are determined. This topic is discussed in Paper 1.
- **How do the RT deformation mechanisms change when the testing temperature reaches application temperatures?** As Laves phases are brittle at room temperature, they are not used at ambient conditions but more likely used to stabilise matrixes that are prone to creep

deformation or soften significantly at higher temperature. Therefore, the next research question was to investigate how the C14 Laves phase changes its deformation behaviour when temperatures increase up to 250 °C. Next to the activation and CRSS values of slip systems, special focus lies on the activation volume and the dislocation motion (homogeneity of deformation). This topic is discussed in Paper 4.

- **How does a change in crystal structure change the deformation behaviour?** In the Mg-Al-Ca system, all three Laves phases are present, the hexagonal C14 and C36 phase as well as the cubic C15 phase. Starting from the C14 Mg_2Ca phase, it is investigated how the deformation behaviour changes with increasing Al content covering the $(Mg,Al)_2Ca$ C36 phase in different compositions up to the cubic Al_2Ca C15 phase. The activation of different slip systems as well as the occurrence of a PLC effect and the homogeneity of deformation are discussed. This topic is discussed in Paper 5 which is still under construction.

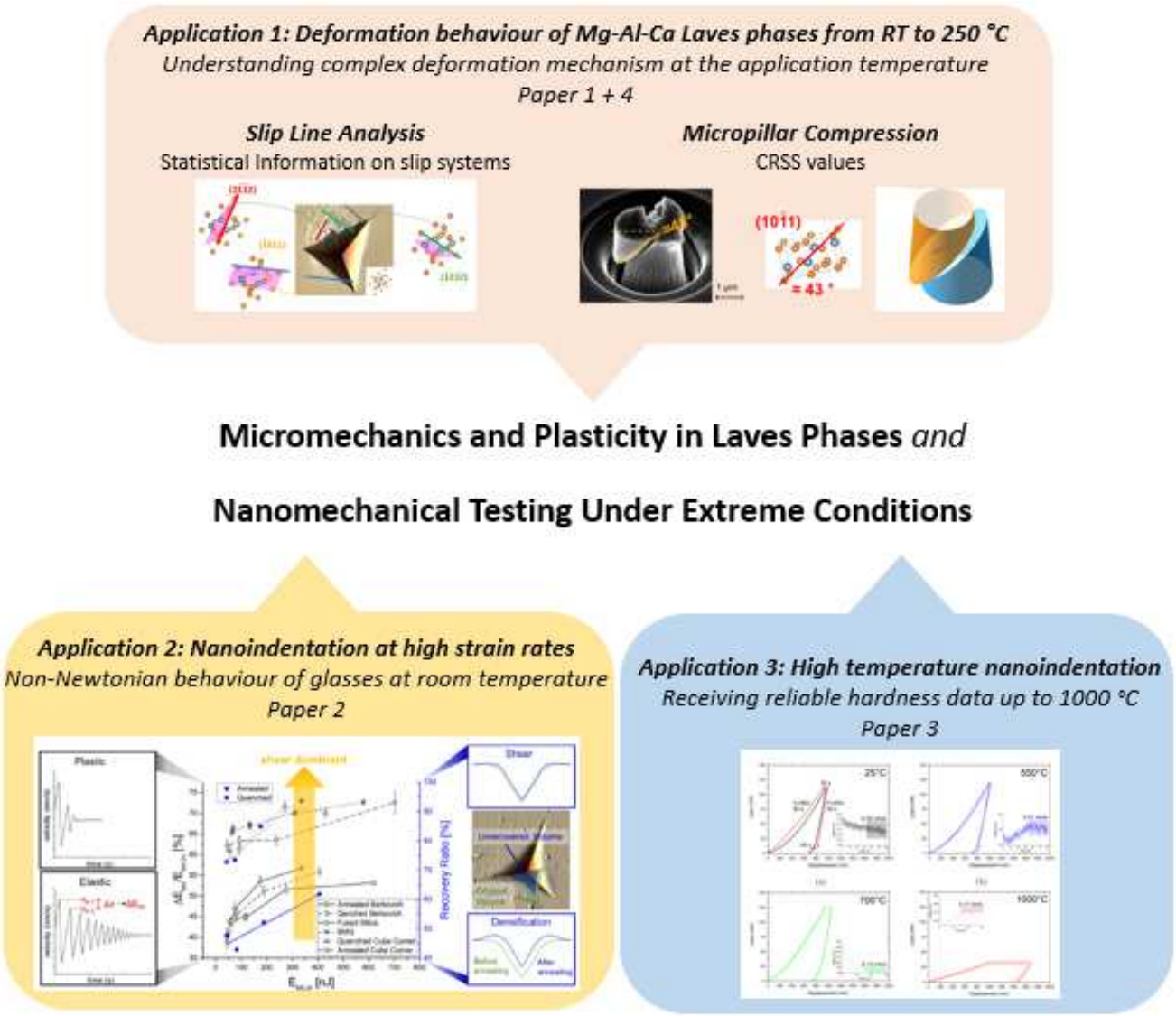

FIGURE 1: GRAPHICAL ABSTRACT DISPLAYING THE STRUCTURE OF THIS WORK

3 THEORETICAL BACKGROUND

3.1 MG-AL ALLOYS

In terms of saving non-renewable resources, light weight structures and materials occupy a central role. Magnesium, as the structurally useable metal with the lowest density is an excellent opportunity to build energy efficient cars e.g., by using Mg as material for motor blocks. Next to its low-weight potential and high specific strength, Mg possesses also negative properties, one of those being the low creep resistance. Recently, a concerted effort was taken to develop creep resistant Mg alloys, with Mg-Al-Ca alloys being a promising example [1-18]. The reason for the drastically improved creep resistance was found to be the precipitation of intermetallic phases forming a fully connected skeleton [1-3, 7, 8, 10]. This skeleton consists mainly of the three Laves phases Mg_2Ca (C14, hexagonal), Al_2Ca (C15, cubic) and $(Mg,Al)_2Ca$ (C36, hexagonal) [6, 7, 13, 14, 19-25]. Next to these, the $Mg_{17}Al_{12}$ phase is also present, but has been ruled out to be the reason for the improved creep resistance due to a significant softening process at 150 °C [26].

3.2 LAVES PHASES IN THE MG-AL-CA SYSTEM

Laves phases belong to the Frank-Kasper phases and crystallise very close to the ideal composition AB_2 with their atomic ratio proportion being close to $\frac{r_A}{r_B} = 1.225$ [19, 27, 28].They are built up by several layered structures with the ordering of these layers determining if a C14, C15 or C36 structure develops. There are two structures, a Kagomé net, consisting of only the smaller atom B (e.g. Mg) and a triple layer consisting of both the smaller and the bigger atom in the order A-B-A (e.g. Mg and Ca), s. Figure 2 .

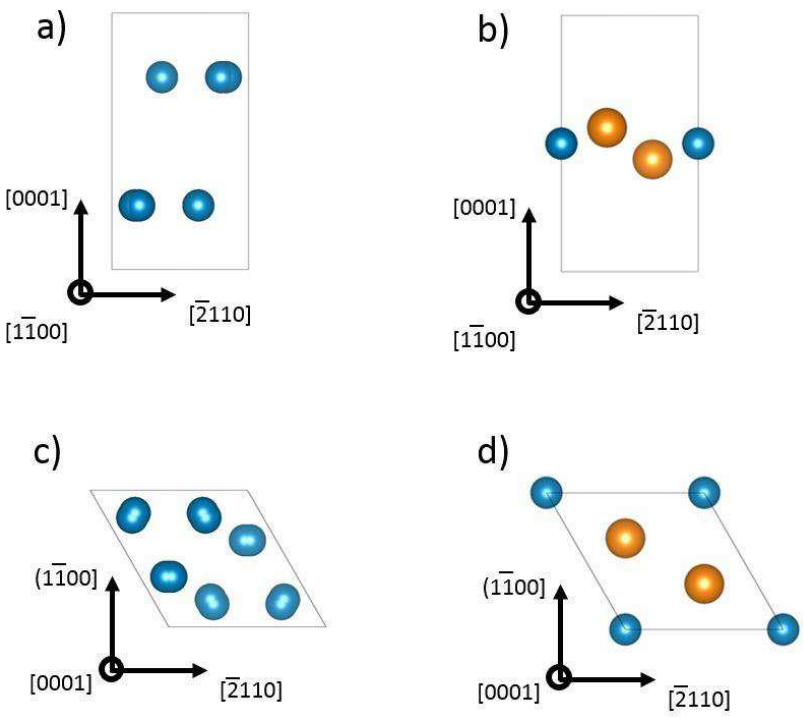

FIGURE 2: LAYERED STRUCTURES THAT BUILD UP LAVES PHASES. THE C14 UNIT CELL CONSISTS OF TWO KAGOMÉ NET LAYERES (A AND C) CONSISTING SOLELY OF MG ATOMS AND A TRIPLE LAYER (B AND D) CONSISTING OF BOTH MG AND CA ATOMS. THE ORDERING OF THESE LAYERED STRUCTURES DETERMINES WHETHER THE UNIT CELL BELONGS TO THE C14, THE C15 OR THE C36 PHASE.

The exact ordering of these layered structure determines whether the unit cell belongs to the hexagonal C14 or C36 or to the cubic C15 phase (Figure 3). Each of these structures has a distinct chemical composition with varying Mg-Al-ratios: While C14 (Mg_2Ca) and C15 (Al_2Ca) consist of only two different chemical elements, the C36 phase can vary between $(Mg_{0.33}Al_{0.66})_2Ca$ and $(Mg_{0.78}Al_{0.22})_2Ca$ [19].

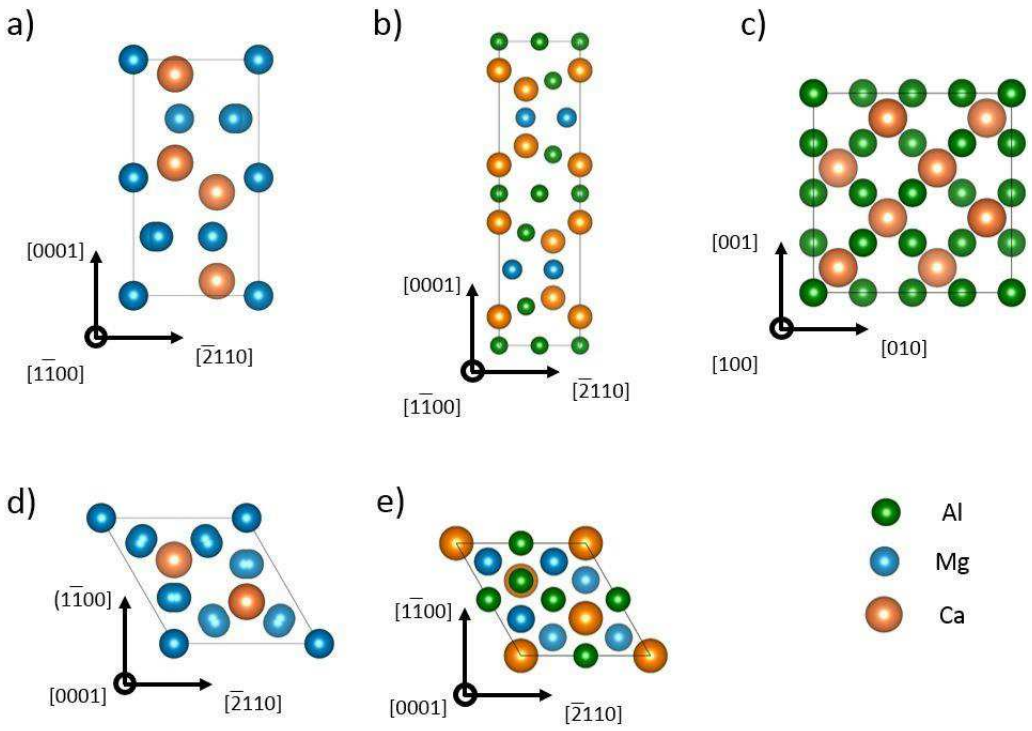

FIGURE 3: DEPENDING ON THE BUILT UP OF THE SINGLE LAYERED STRUCTURES, DIFFERENT UNIT CELLS CAN DEVELOP: THE C14 PHASE (A AND D) AS WELL AS THE C36 (B AND E) PHASE ARE HEXAGONAL, WHILE THE C15 PHASE (C) IS CUBIC.

3.3 MECHANICAL PROPERTIES OF LAVES PHASES

Though there are quite a few studies investigating the mechanical properties of Laves phases, several basic aspects are still not or only poorly investigated e.g., the deformation mechanisms at room temperature, the exact nature of the dislocations (Burger`s vector, partial or perfect dislocation, etc.), statistics on the activation of different slip systems and their CRSS values or the effect of strain rate on dislocation motion.

3.3.1 ROOM TEMPERATURE DEFORMATION MECHANISMS IN LAVES PHASES

The mechanical properties of Laves phases at room temperature are still broadly unknown. It was suggested that a Peierls mechanism is active in Laves phases stating that the lattice resistance is the critical factor inhibiting dislocation motion [29-31]. As dislocation motion against this resistance is known to be thermally activated [32], it is strongly temperature dependent with much higher stresses required at low temperatures. As these stresses are higher than the fracture strength, samples fail by brittle failure rather than plastic deformation at low temperatures, inhibiting the investigation of deformation mechanism. Therefore, several authors investigated the deformation behaviour of macroscopic Laves

phase samples tested at high temperatures (HT) [29-31, 33-46] or deformed an alloy containing the Laves phase as small particles to introduce deformation into the Laves phase at room temperature (RT) [35, 47-52]. A third way, which this thesis follows as well, is the use of nanomechanical test methods using the size effect to deform Laves phases plastically at room temperature: Korte and Clegg [53] and Takata et al. [54, 55] used micro-compression experiments on Laves phases at room temperature and investigated critical stresses and slip systems. Still, little is known about the exact room temperature deformation mechanisms e.g., critical resolved shear stress (CRSS) of different slip systems or statistical information about the activation of different slip systems or dislocation structures and Burger`s vectors of Laves phases at room temperature.

An often-proposed mechanism of plastic deformation in complex structures (e.g. Laves phases) is the synchroshear mechanism. Originally proposed to take place in sapphire by Kronberg [56] it was then confirmed to take place in MnS [57] and proposed to occur in Laves phases as well [58]. Chisholm observed an atomic displacement resembling the synchroshear mechanism in an undeformed Laves phase [59] and several authors assumed synchroshear to operate in Laves phases [47, 48, 60], however first evidence for this hypothesis was just recently given by Schröders et al. [61]. The synchroshear mechanism describes the synchronized movement of two partial dislocations moving in parallel planes of the triple layer and diverging directions [59].

3.3.2 High temperature deformation mechanisms in Laves phases

Several authors, performing HT compression experiments on macroscopic Laves samples describe phase transformation between C36 and C15 as a main deformation mechanism: for transferring a C36 phase into a C15 phase, a Shockley partial is needed, resembling the synchroshear mechanism [46, 47, 49]. Regarding the dislocation structures, basal slip is stated to be the dominant deformation mechanism in the hexagonal Laves phases at high temperatures [36, 41, 44]. Nevertheless, other slip systems like prismatic or pyramidal slip are observed as well frequently, in some cases even as the dominant slip system [29, 30, 43, 45, 48, 50]. Krämer et al. performed a theoretical study on possible slip systems in the C14 and C15 structure based on geometrical aspects (i.e. out-of-plane movement, distance between two glide planes, number of next neighbours, etc.) [39]. She stated that next to the basal slip system, all other typical hexagonal slip systems, i.e. 1^{st} and 2^{nd} order prismatic as well as 1^{st} and 2^{nd} order pyramidal slip system, exhibit a theoretically possible (and energetically sensible) Burger`s vector. Liu et al. [48] then proposed that in the more complex C36 phase, a concept called “zonal glide” could take place, where perfect dislocations split into several partial dislocations, possibly gliding on slightly different

planes and directions, which then form a “netto” perfect dislocation, without giving experimental evidence thus far.

Paufler et al. conducted a series of macroscopic compression experiments at HT, mainly on C14 single crystals. Next to the already mentioned activation of different slip systems, they determined that the brittle-to-ductile temperature is 0.65 of the melting point [31, 38, 40]. They furthermore postulate that at high temperatures ($T > 0.8\ T_M$), dislocation climb could be active [41]. When testing samples with different chemical compositions (< 2 at. % deviation from the ideal AB_2 composition), they found a significant drop in dislocation velocity as well as a decrease in hardness with increasing off-stoichiometry. This is accompanied by an increasing homogeneity of the deformation process with increasing off-stoichiometry [29-31, 40, 42]. They conclude that dislocation starvation is an important feature for the deformation of Laves phases and that with increasing off-stoichiometry, dislocations are easily pinned by anti-site defects arising from the deviation from the stoichiometric composition. This is supported by the work by Takata et al., who showed that the critical stress needed to deform a micro pillar is significantly reduced by pre-deforming the pillar [54, 55].

The decrease in hardness with increasing off-stoichiometry (“defect softening”) found by these authors [30, 42, 62] was explained by the possibility to overcome the dislocation starvation. However, other studies report the exact opposite behaviour: Pike et al. [63-65] report an increase in hardness with increasing off-stoichiometry (“defect hardening”). They conclude that with increasing off-stoichiometry, anti-site defects are generated and that these – contradicting to Paufler et al. – display obstacles for dislocation motion instead of facilitating deformation by displaying potential dislocation sources. As both sides give reasonable explanations and present reliable data, it is difficult to judge about the accuracy of their work or where the discrepancy between these data comes from. Finally, Voss et al. [66] presents data, where the HT-compression strength of Laves phases did not exhibit the V-shape proposed by the previous experiments, but a linear trend from one side of the off-stoichiometry to the other side.

Regarding the C15 phase, several authors describe twinning on the $\{111\}$ plane being the dominant deformation mechanism [37, 51, 52, 67-69]. The $\{111\}$ plane was found to be the dominant slip system for dislocation slip as well, with $\{110\}$, $\{100\}$ and $\{112\}$ being possible as well [39].

3.4 OTHER MATERIALS

Next to the main material system of this study, Laves phases in the Mg-Al-Ca system, two other materials where investigated to extend the application of nanomechanical test methods to two limits: for high strain rate testing, several glass systems where used since these materials undergo a fundamental change in deformation mechanism with varying strain rates. To test the limits of high temperature nanoindentation, a super alloy was used since also here a fundamental change of deformation mechanism can be observed, this time over temperature.

The practical use of glasses is strongly linked to the resistance against crack initiation and more importantly crack growth, i.e. the toughness of a glass. These properties in turn are also determined by the dominant deformation mechanisms of flow. Depending on whether the glass deforms mainly by volume conservative shear or densification – compaction of the glass structure - it is referred to as normal or anomalous, respectively [70, 71]. Activation of either results in different cracking and deformation behavior [72]. The activation of either deformation mechanism depends not only on the structure and chemistry of the glass but also on the environmental and loading conditions, e.g. temperature, strain rate and stress state. The response of glasses to high strain rates is of special interest as a change in deformation characteristics has been seen with increasing strain rate for numerous glasses at high temperatures: at low strain rates, their viscosity is constant resulting in a linear increase of stress with increasing strain rate - Newtonian behavior. With increasing strain rate, deformation enters a non-Newtonian regime, where the viscosity decreases and thus the stress needed to introduce plastic deformation converges to a constant level and becomes independent of the strain rate [73] [74]. Whether this behavior extends to low temperatures was previously unknown.

In this study, different glass systems have been tested at room temperature over strain rates spanning seven orders of magnitude by using quasi-static nano-indentation and dynamic impact-nanoindentation. To cover a maximum diversity of glasses, the most anomalous glass, fused silica, and a glass presenting the normal, shear dominated extreme, a bulk metallic glass (BMG), were chosen. Additionally, a sodium-borosilicate glass (NBS) was subjected to two different thermal treatments resulting in an open structure (quenched) and a dense structure (annealed) and included into this study to change the extent of normal and anomalous behaviour within one glass composition [75, 76]. To vary the hydrostatic stress component and hence the relative fraction of densification during deformation [77], the NBS glasses

were additionally tested with two different tip geometries: a sharp cube corner and a comparatively flat Berkovich tip.

For the high temperature testing, a CMSX-4 superalloy and a 200 µm thick Amdry-386 bond coat was tested. In application, this bond coat provides environmental resistance and mediates thermal stresses between the superalloy and thermal barrier coating. The single crystalline CMSX-4 serves as a well-studied, but highly anisotropic reference material, while the polycrystalline bond coat is well suited to this and future studies by nanoindentation due to the more isotropic behaviour with small grain sizes, its intrinsically small size with regards to the thickness, and the interest in its high temperature properties for coating design.

3.5 NANOMECHANICAL TEST METHODS

Nanomechanical test methods offer the possibility to test samples site specifically and on a small scale so that even in samples with a very small grain size or where the material is only present as small particles, mechanical tests can be performed. The size effect offers the possibility to test materials which are brittle on a macroscopic scale [78-90].

In this study, two nanomechanical test methods are mainly used: nanoindentation and micropillar compression. While in nanoindentation a pyramidal or conical tip is used to indent a sample and measure depth and force to calculate a hardness by the Oliver and Pharr method [81, 82], micropillar compression [88-90] uses focused ion beam (FIB) milling to create cylindrical specimen, which are then compressed with a flat top indenter tip (flat punch).

Nanoindentation experiments offer the advantage of being able to quickly perform a large number of tests on selective positions. Due to the pyramidal shape of the tip, however, the stress field is inhomogeneous and it is thus difficult to make assumptions about the stress on a specific plane (critical resolved shear stress, CRSS). Micropillar compression experiments, on the other hand, offer the possibility to test a material in an approximately uniaxial stress field so that CRSS values can be determined. Milling samples with FIB is time consuming, leading to very little statistics, though.

In this work, both (in-situ) nanoindentation and micropillar compression experiments have been conducted in combination with atomic force microscopy (AFM) and scanning electron microscopy (SEM) as well as transmission electron microscopy (TEM) to investigate the deformation mechanisms of Laves phases between RT and 250 °C. Typical analysis steps are presented in Figure 4.

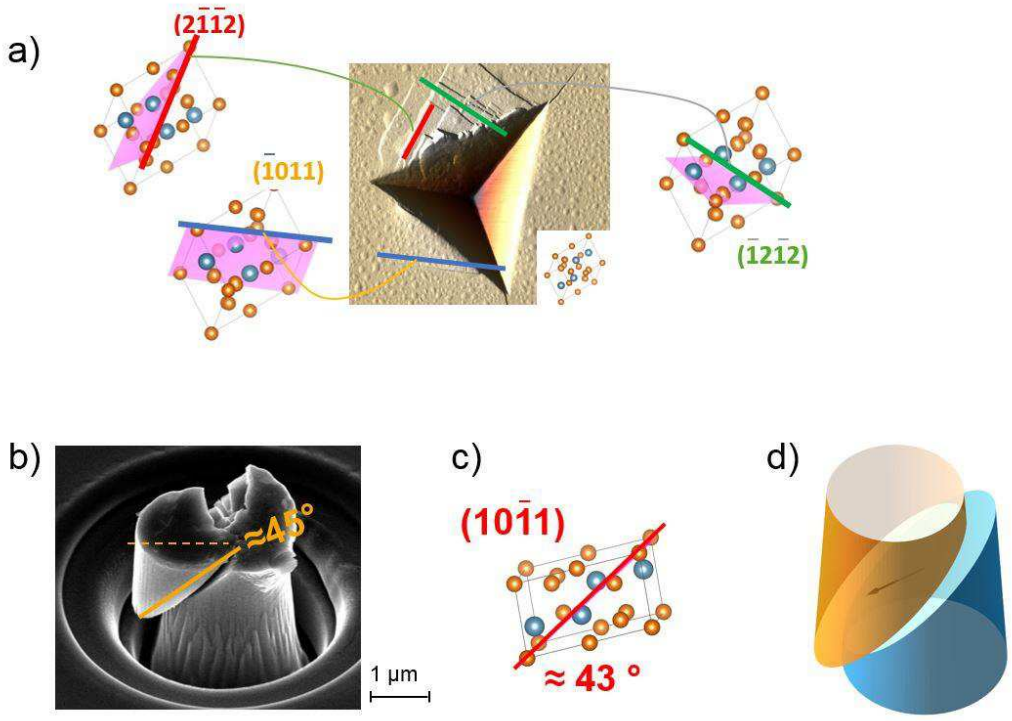

FIGURE 4: ANALYSIS OF NANOMECHANICAL TEST METHODS TO INVESTIGATE THE DISLOCATION STRUCTURE. A) DISPLAYS A RESIDUAL IMPRESSION FROM NANOINDENTATION WITH SLIP LINES AROUND THE INDENT AND HOW EBSD IS USED TO CORRELATE THESE LINES TO SLIP PLANES. MICROPILLAR COMPRESSION EXPERIMENTS IDEALLY SHOW ONE SLIP EVENT (B) WHICH CAN THEN BE CORRELATED TO A SLIP PLANE (C). D) DISPLAYS A SIMULATED MICROPILLAR TO CONFIRM THE SLIP DIRECTION.

3.5.1 THE OLIVER AND PHARR METHOD

Nanoindentation uses a sharp tip consisting of a hard material, e.g. diamond, sapphire or cubic BN, to penetrate into a material. By continuously measuring the load and the displacement, one can then calculate different parameters, e.g. the hardness or the elastic modulus. For this, the Oliver and Pharr method [81, 82] is used. Different shapes are used for the tip, conical, spherical and pyramidal ones [79]. Due to their self-symmetry, pyramidal tips are the most common ones. Depending on whether one wants to introduce a more hydrostatic stress field or a stress field with a higher portion of shear stresses, a flat or sharp tip geometry can be used, respectively [91]. The standard geometry used for most experiments is the Berkovich tip, a flat pyramidal tip.

Generally, the hardness H can be calculated using equation (1)

$$H = \frac{L}{A} \tag{1}$$

the load L is measured, and the area A can be estimated from the displacement signal:

$$A = 24.5\, h_c \tag{2}$$

with h_c being the depth signal. Equation (2) is only valid for an ideal Berkovich tip without any effect of wear. However, all tips deviate more or less strongly from this ideal shape, depending on how long they have been used. Therefore, a calibration measurement is conducted. Here, a known material (e.g. fused silica) is indented and the shape of the tip is determined from the load-displacement signal. The result, called diamond are function (DAF) is then used to analyse measurements of unknown materials to determine the hardness or other parameters of interest.

3.5.2 Slip line analysis

Figure 4 a) displays a residual impression from nanoindentation and how the slip lines around the indent are correlated to slip planes. From electron backscatter diffraction microscopy (EBSD) measurements, the orientation of the sample can be determined and the trace of different slip planes on the sample surface can be calculated. By comparing the angle between a fixed axis and the slip line on the one hand and the angle between the same fixed axis and different slip plane traces on the other hand, single slip lines can be attributed to different slip planes. In order to keep a balance between the accuracy of the method and a sufficient amount of indexable slip lines, a maximum deviation of 6° was taken between the angle of the slip line in the SE image and the angle of the slip plane trace in the EBSD image.

3.5.3 Strain rate jump tests and activation volume

Though the stress field is strongly inhomogeneous – making the determination of a singles strain value and correspondingly of a single strain rate difficult – a standard “indentation strain rate” has been established (equation (3)) [92].

$$\dot{\epsilon} = \frac{\dot{h}}{h} \tag{3}$$

Even though this strain rate is not directly comparable to strain rates determined in uniaxial testing (tensile test, compression test, etc.), it is a useful parameter to compare different indentation cycles. Using equation (3), it is possible to keep the strain rate constant during one experiment by increasing the displacement rate with increasing displacement. It is furthermore possible to jump between different

strain rates in one indentation cycle. This procedure is called strain rate jump (SRJ) tests and can be used to determine the strain rate sensitivity (SRS) following equation (4)

$$m = \frac{\delta \ln H}{\delta \ln \dot{\epsilon}} \tag{4}$$

The SRS can furthermore be used to determine an activation volume V

$$V = \frac{3 * \sqrt{3}\, k\, T}{m\, H} \tag{5}$$

For low temperatures, the activation volume can be calculated using the Peierls stress (equation (6)):

$$\tau\,(T, \dot{\gamma}) = \tau_p + \frac{kT}{V} \ln\left(\frac{\dot{\gamma}}{\rho b^2\, \nu}\right) \tag{6}$$

$$V = kT \frac{\Delta \ln \dot{\gamma}}{\Delta \tau} \tag{7}$$

with $\dot{\gamma}$ being the shear rate, b the Burgers vector and ρ the dislocation velocity. Using the van Mises criterium (equation (8)) enables calculation of the activation volume (equation (9))

$$\tau = \sqrt{3}\, \sigma \tag{8}$$

$$V = 3 * \sqrt{3}\, kT \frac{\Delta \ln \dot{\epsilon}}{\Delta H} \tag{9}$$

Due to a strong indentation size effect (ISE) observed in the material investigated in this study, the hardness was averaged for a depth of 10 nm before and after each strain rate jump and the mean value was used to determine an SRS.

3.5.4 Micropillar compression

Focused ion beam milling (FIB) was used to mill cylindrical specimen with a diameter of 2 µm into the material. A conical tip where the top has been cut off so that there is a flat surface with a 10 µm diameter (flat punch) is then installed in the nanoindenter and the pillar are compressed measuring the load and the displacement. From these data the stress-strain curve can be calculated. Micropillar

compression experiments ideally lead to a single slipping event of the pillar (Figure 4 b). The orientation of the grain is then used to determine the angle between the surface and possible slip planes and thus correlate the slip event to a single plane (Figure 4 c). By using the uniaxial stress and the Schmid factor of the determined slip system, a CRSS can be calculated.

3.5.5 High temperature testing

Tests were performed using a MicroMaterials NanoTest P-3 system modified by a custom-built vacuum chamber (~ 10^{-5} mbar). Indents were performed to a depth of 1 µm using a an independently-heated Berkovich sapphire tip at a constant load rate of 2 mN/s, followed by a 30 second dwell period and 5 mN/s unloading rate. At high temperatures (> 900 °C), only single indents could be performed since the tests at such high temperatures lead to a strong blunting due to mechanical loading as well as chemical reaction of the tip. To accommodate on this blunting, a DAF was performed before and after the test series as well as after the tests at 700 °C. Thermal drift was measured at 90 % of the load to correct the load-displacement curve. Next to the blunting of the tip and adjusting the temperatures to minimize the thermal drift, creep proved to be a difficulty by overlaying the thermal drift.

3.5.6 Nano-Impact testing

In normal (quasi-static) nanoindentation the accessible strain rates are quite limited, with most measurements falling in the range of 0.1 – 0.001 s-1 [93]. This does not reflect the loading conditions materials have to face in reality, with brittle materials often failing during loading at high strain rates, e.g. falling to the ground or being hit by small objects with high velocity. Standard high-velocity testing methods, e.g. Charpy-impact testing, use macroscopic sample dimensions [94], but for brittle materials like glasses, it is well known that failure is controlled by pre-existing defects, such as small cracks and notches, which commonly depend on the manufacturing process and reduce the critical load for failure to drastically below the intrinsic material strength [95]. The latter may then only be estimated where cracking is suppressed and plasticity activated instead, e.g. in nanoindentation.

In order to combine the advantages of a small-scale impact with a quantitative measurement, impact nanoindentation testing can be used. It significantly expands the range of accessible strain rates compared with quasi-static nanoindentation and retains the small scale and confining pressure that inhibit cracking and hence permit the characterisation of plastic deformation. There are several publications using a pendulum-based nanoindentation system (from MicroMaterials Ltd.) to perform impact nano-indentation experiments [96-109], as was also done in this work.

4 RESULTS

4.1 USING IMPACT NANOINDENTATION TO TEST MATERIALS OVER LARGE STRAIN RATE REGIMES

By stiffening the pendulum of the Micro Materials Ltd. Nanotest P3, ringing (i.e. vibration of the pendulum overlaying the actual movement of the pendulum due to the indentation) can be avoided and the displacement-time curves can be recorded with sufficient accuracy to use the signal to determine different characteristics (s. Figure 5).

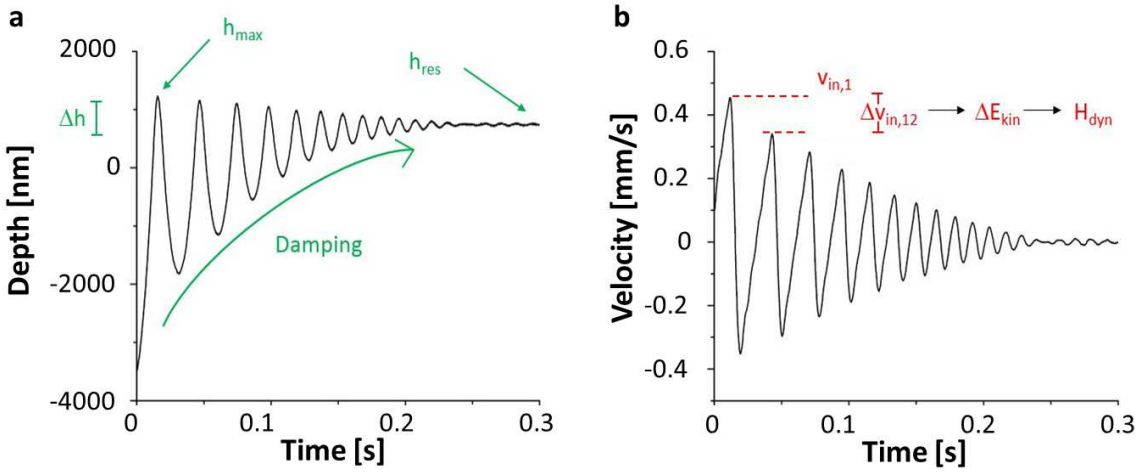

FIGURE 5: DEPTH-TIME CURVE (A) AND VELOCITY-TIME CURVE OBTRAINED FROM THE IMPACT NANOINDENTATION EXPERIMENTS USING A CUSTOM MADE STIFFENED PENDULUM.

From the originally obtained depth-time curve, a velocity-time curve can be determined and several characteristics can be derived from this curve:

Kinetic Energy, E_{kin}: In a pendulum-based system the effective mass of the pendulum may be determined using the ratio of the applied force and the resulting acceleration. The initial kinetic energy, $E_{kin,in}$, is subsequently derived with the effective mass of the system, m_{eff}, and the maximum velocity prior to first indentation, v_{in}, as:

$$E_{kin,in} = \frac{1}{2} m_{eff} v_{in}^2 \quad \textbf{(10)}$$

m_{eff} is determined in a free-swinging mode by measuring the acceleration due to a known load. As the velocity prior to impact varies with both the impulse height and load, $E_{kin,in}$ gives a unique value which can be used to compare different measurements. To analyse the amount of plastic deformation during the first impact, the energy difference between the first and the second impact, taken at the point of maximum velocity just before contact, can be derived:

$$\Delta E_{kin} = E_{kin,1} - E_{kin,2} \quad \textbf{(11)}$$

Relevant depths - h_{res}, h_{max}, Δh : To estimate the amount of plastic deformation, one can measure the residual indentation depth, h_{res}, at the end of the experiment. The difference, Δh, between the maximum depth measured over the whole experiment and the residual indentation depth, h_{max}, and h_{res}, may be used to estimate the proportion of the elastic response. Note that the maximum depth is commonly achieved during the first impact, while the residual depth is measured after several impacts at decreasing velocities. With the system used in this study, the prescribed impact load is still applied when the system comes to rest, therefore h_{res} still incorporates the elastic response of the material.

Damping coefficient, DC: This parameter enables investigation of the deformation mechanisms during the impact tests and determination of how the material absorbs energy into plastic and elastic deformation. While the overall deformation is given by h_{res}, the DC allows the response to be monitored semi-continuously during testing. This value therefore reflects whether the deformation mechanism changes during single indents, e.g. whether all the energy is already consumed in two or three indents, or whether there is a gradual decrease in energy over several indents. By fitting an exponential function to the maximum velocity (or depths) values of each impact, the damping coefficient can be defined as the best fit to the *n* distinguishable maximum velocities, $v_{in,n}$ at their respective time steps t_n:

$$DC = \frac{1}{t_n} \ln\left(\frac{v_{in,n}}{v_{in,1}}\right) \quad \textbf{(12)}$$

Dynamic Hardness: Measuring hardness in impact nanoindentation is not as straightforward as for quasi-static indentation. Although generally speaking, the dynamic hardness is defined as the loss in kinetic energy divided by the volume of the impression [104, 109], the specific values used for this are not as well-defined as for the load and area used in quasi-static indentation hardness. Two alternatives are available for dynamic hardness, essentially either considering the entire indentation, or merely the first impact.

Considering the entire indentation, hardness is calculated by Equation 4, taking the difference in kinetic energy before the first ($v_{in,1}$) and the second impact ($v_{in,2}$) and the volume of the indentation created at the final residual depth derived from the diamond area function (DAF) [109] using this final depth ($V_{DAF}(h_{res})$) [104, 109].

$$H_{dyn,res} = \frac{\frac{1}{2} m_{eff} \left(v_{in,1}^2 - v_{in,2}^2 \right)}{V_{DAF}(h_{res})} \quad \textbf{(13)}$$

4.2 ACTIVATION OF DIFFERENT SLIP SYSTEMS IN THE C14 AND C15 PHASES AT ROOM TEMPERATURE

For testing the activation of different slip systems in the C15 phase, three orientations were indented and analysed using EBSD and secondary electrons (SE). Figure 6 displays the activation of different slip systems in the C15 phase at room temperature.

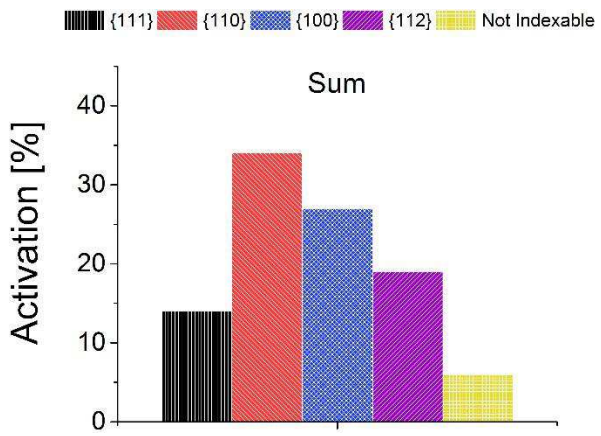

FIGURE 6: ACTIVATION OF DIFFERENT SLIP SYSTEMS IN THE C15 PHASE. THE DOMINANT SLIP SYSTEM IS {110}, FOLLOWED BY {100}, {112} AND {111}. 94 % OF ALL MEASURED SLIP LINES COULD BE CORRELATED TO ONE OF THESE SLIP PLANES.

The dominant slip system is $\{110\}$, followed by $\{100\}$, $\{112\}$ and $\{111\}$, which have all been observed experimentally [39]. All four slip systems together comprise 94 % of all measured slip lines. Three different orientations were tested and showed no significant deviation.

For the hexagonal C14 phase, $\{0001\}$ (basal), $\{10\bar{1}0\}$ (prismatic 1st order), $\{11\bar{2}0\}$ (prismatic 2nd order), $\{10\bar{1}1\}$ (pyramidal 1st order) and $\{11\bar{2}2\}$ (pyramidal 2nd order) were considered. Due to the anisotropy of the hexagonal cell, different orientations were tested. Figure 7 displays the activation of different slip systems for varying angles between the x-axis and the surface normal at room temperature. Additionally, Matlab was used to simulate 1,000,000 randomly oriented lines which were then correlated to the trace of the investigated slip systems for every orientation. The result gave a number of how the distribution would look like if only pure geometry is considered, i.e. if all systems would have the same CRSS value. By comparing the two values – the experimentally determined distribution of activation of different slip systems and the value gained by considering pure geometry – one can make assumptions about the magnitude of the CRSS value a slip system should exhibit. The more negative the deviation is, the more unfavourable this slip system should be and therefore the higher the CRSS should be (Table 10).

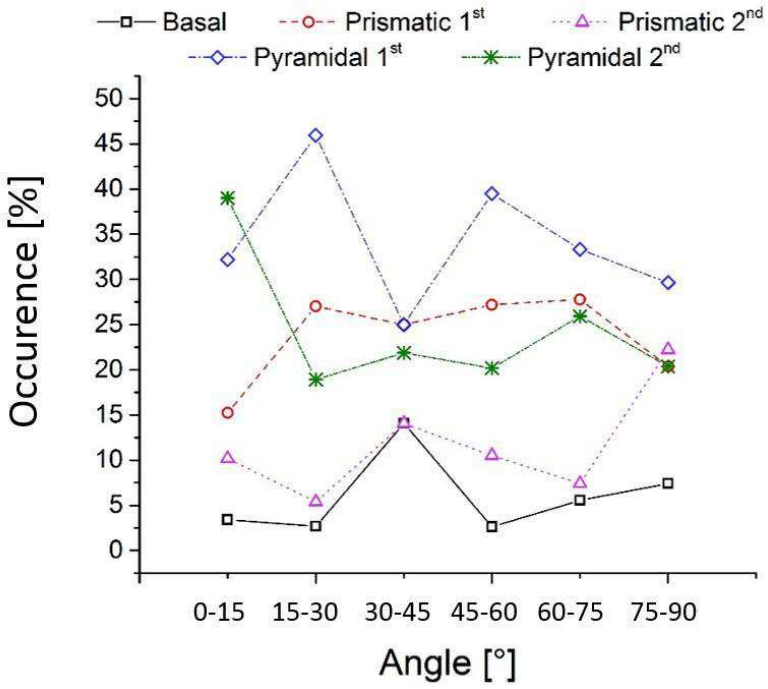

FIGURE 7: OCCURRENCE OF DIFFERENT SLIP SYSTEMS IN THE C14 PHASE AT ROOM TEMPERATURE FOR DIFFERENT ORIENTATIONS. THE ANGLE ON THE X-AXIS CORRESPONDS TO THE ANGLE BETWEEN THE C-AXIS AND THE SURFACE NORMAL.

Next to nanoindentation experiments, micropillar compression experiments have been conducted on the C14 phase at room temperature, allowing the determination of CRSS values. Table 10 lists the values determined by nanoindentation experiments and by geometrical analysis as well as the CRSS values determined by micropillar compression experiments.

TABLE 10: RESULTS OF THE GEOMETRICAL AND EXPERIMENTAL SLIP TRACE ANALYSIS WITH THE OCCURRENCE OF SLIP PLANES IN THE EXPERIMENT, Ω_{EXP} , THE GEOMETRICAL PREDICTION OF EACH PLANE'S OCCURRENCE, $\Omega_{THEO.}$, AND THE RESULTING DEVIATION, Δ, WITH THE MEASUREMENT OF CRITICAL RESOLVED SHEAR STRESSES (CRSS) BY MICROCOMPRESSION.

	Slip plane	Basal $\{0001\}$	1st order prismatic $\{10\bar{1}0\}$	2nd order prismatic $\{11\bar{2}0\}$	1st order pyramidal $\{10\bar{1}1\}$	2nd order pyramidal $\{11\bar{2}2\}$
Na	Number of traces	22	92	45	131	92

	Ω_{exp} [%]	6.0	23.8	11.6	34.3	24.4
	Ω_{theo} [%]	4.8	16.8	16.3	32.9	29.3
	$\Delta = \Omega_{exp} - \Omega_{theo}$ [%]	1.2	7.0	-4.7	1.4	-4.9
µ-compression	Number of pillars	6	2	0	4	12
	Slip direction	<a>	<a>	<a>	<a>	<c+a>
	CRSS [GPa]	0.52± 0.05	0.44 ± 0.01	-	0.53 ± 0.07	0.59 ± 0.07

TEM experiments were conducted to randomly confirm the results from the slip line analysis as well as to investigate the exact nature of Burgers vectors in the C14 phase.

4.3 DEVELOPMENT OF DEFORMATION MECHANISMS IN THE C14 PHASE WITH INCREASING TEMPERATURE

Similar procedure has been followed to investigate the HT deformation mechanisms of the C14 phase. As there are two variables – orientation and temperature – three orientations were chosen to be investigated in order to keep the size of the data set in a reasonable order. The orientations investigated were close to $0°(0001)$, $45°(0001)$ and $90°(0001)$ with the angle describing the angle between the surface and the (0001) direction. As the $90°(0001)$ orientation showed only a very small number of slip lines but uniform pile up already at 50 °C, no data about the activation of different slip systems in this orientation could be determined. The activation of different slip systems for the $0°(0001)$ and the $45°(0001)$ orientations as well as the CRSS values are displayed in Figure 8.

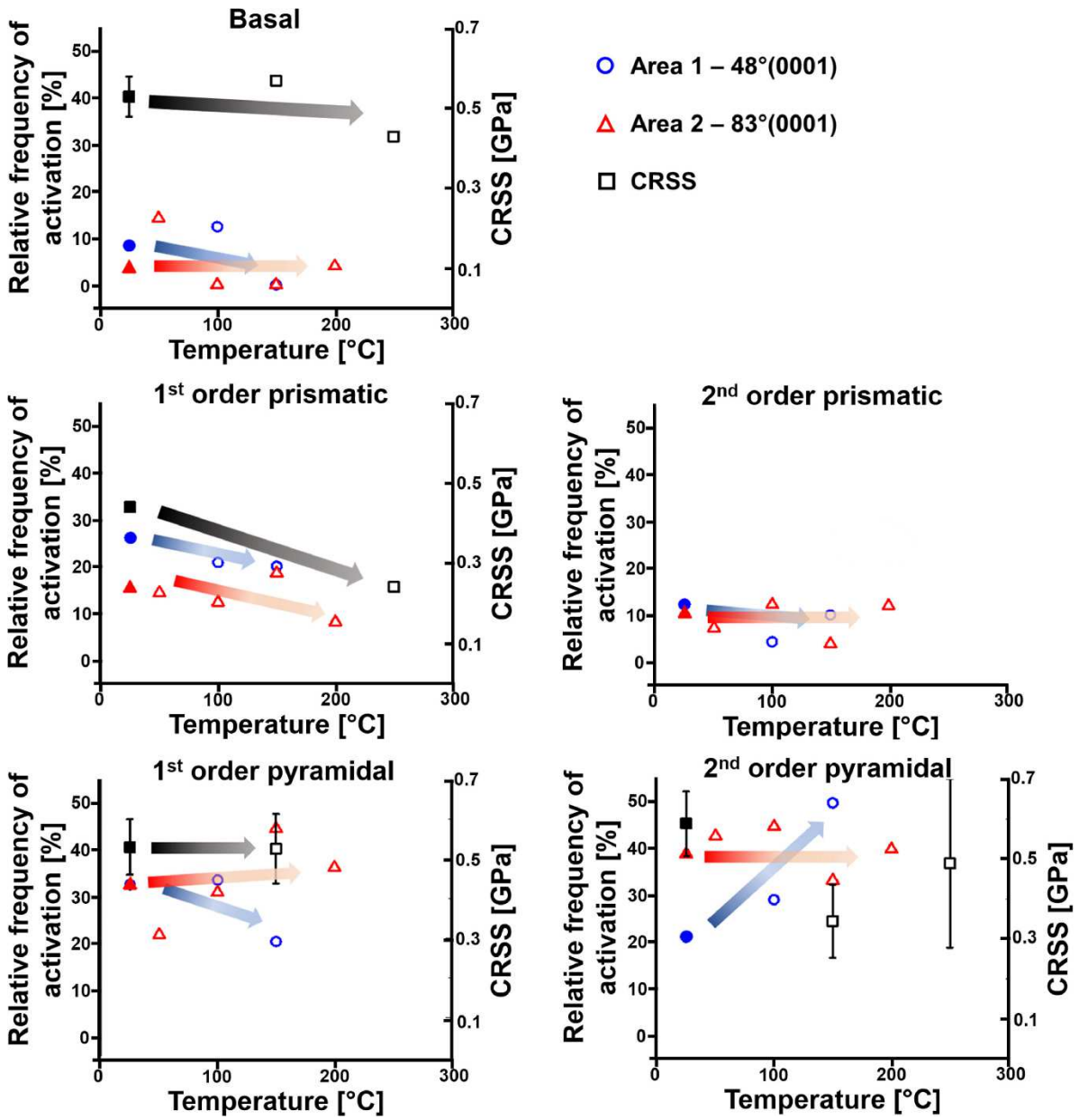

FIGURE 8: ACTIVATION OF DIFFERENT SLIP SYSTEMS FOR TEMPERATURES BETWEEN RT AND 250 °C. THE RED ARROWS DESCRIBE THE 7°(0001) ORIENTATION, THE BLUE ONES THE 44°(0001) ORIENTATION (LEFT AXIS). THE BLACK SYMBOLS STAND FOR CRSS VALUES DETERMINED IN MICROPILLAR COMPRESSION (RIGHT AXIS).

Next to the activation of slip systems and CRSS values, other parameters have been studied: the occurrence of plastic instabilities, the activation volume and the number of slip lines per indent. It was found that at ambient temperatures, the C14 phase exhibited plastic instabilities, also referred to as Portevin-le-Chatelier (PLC) effect (Figure 9). At low temperatures, a significant PLC effect can be

observed while the number of steps in the load-displacement curves decreases with increasing temperature.

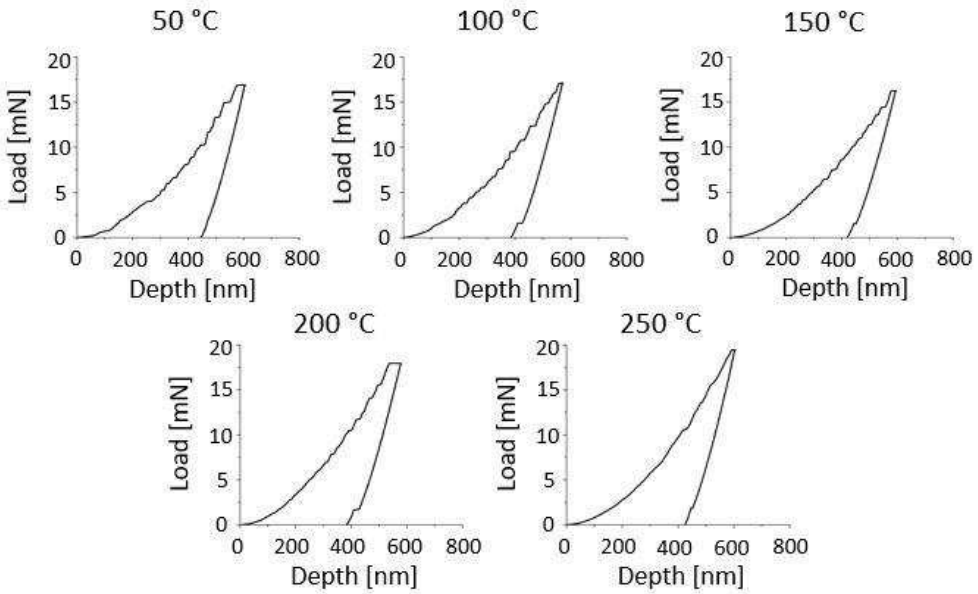

FIGURE 9: THE OCCURRENCE OF PLASTIC INSTABILITIES IN THE C14 PHASE AT DIFFERENT TEMPERATURES. WHILE THE EFFECT IS STRONG AT LOW TEMPERATURES, THE NUMBER AND SIZE OF STEPS DECREASES WITH INCREASING TEMPERATURE.

In addition to this, the number of slip lines around the indents decreased with increasing temperature (Figure 10). While clear, straight lines can be observed at low temperatures (red lines), these lines start to form bowed out shapes (white lines), following the stress field in very narrow steps, and finally disappear completely with increasing temperature.

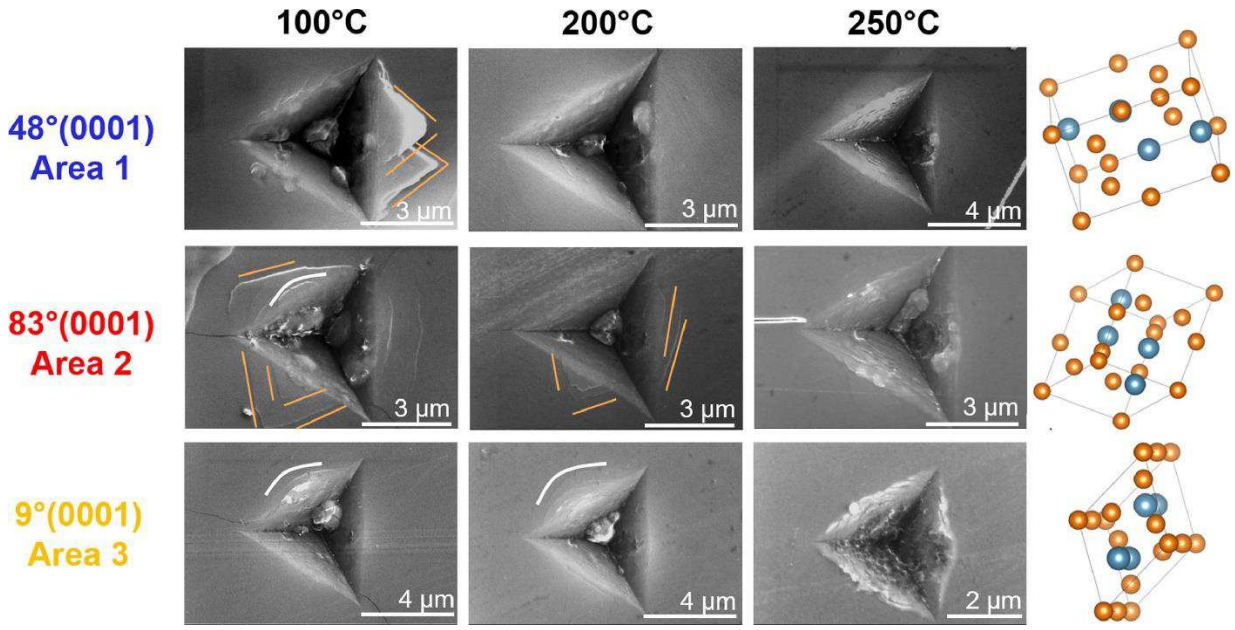

FIGURE 10: NUMBER OF SLIP LINES AROUND THE INDENT. WHILE AT LOW TEMPERATURES, CLEAR STRAIGHT LINES CAN BE OBSERVED AROUND THE INDENTS (RED), THESE LINES EITHER START TO FORM BOWED OUT SHAPES (WHITE) OR JUST VANISH (E.G. HOMOGENEOUS PILE UP).

Finally, the strain rate sensitivity (SRS) was determined from strain rate jump tests. While it was difficult to determine a single value, as a strong size effect and the occurrence of plastic instabilities hinder a clear determination of hardness values, the activation volume was found to be close to zero or even negative.

4.4 CHANGES IN DEFORMATION MODE IN THE C36 PHASE AT ROOM TEMPERATURE WITH VARYING COMPOSITION

A sample consisting of C36 phase was produced with the nominal compositions of $(Mg_{1.37}Al_{0.63})_2Ca$. The sample consisted of very small grains with varying composition and orientation. By means of FIB an array was milled into the sample so that areas with constant orientation and composition could be determined and tested. Three orientations were chosen, close to $0°(0001)$, $45°(0001)$ and $90°(0001)$. The composition varied between $(Mg_{10}Al_{90})_2Ca$ and $(Mg_{70}Al_{30})_2Ca$. Several changes in deformation behaviour could be observed.

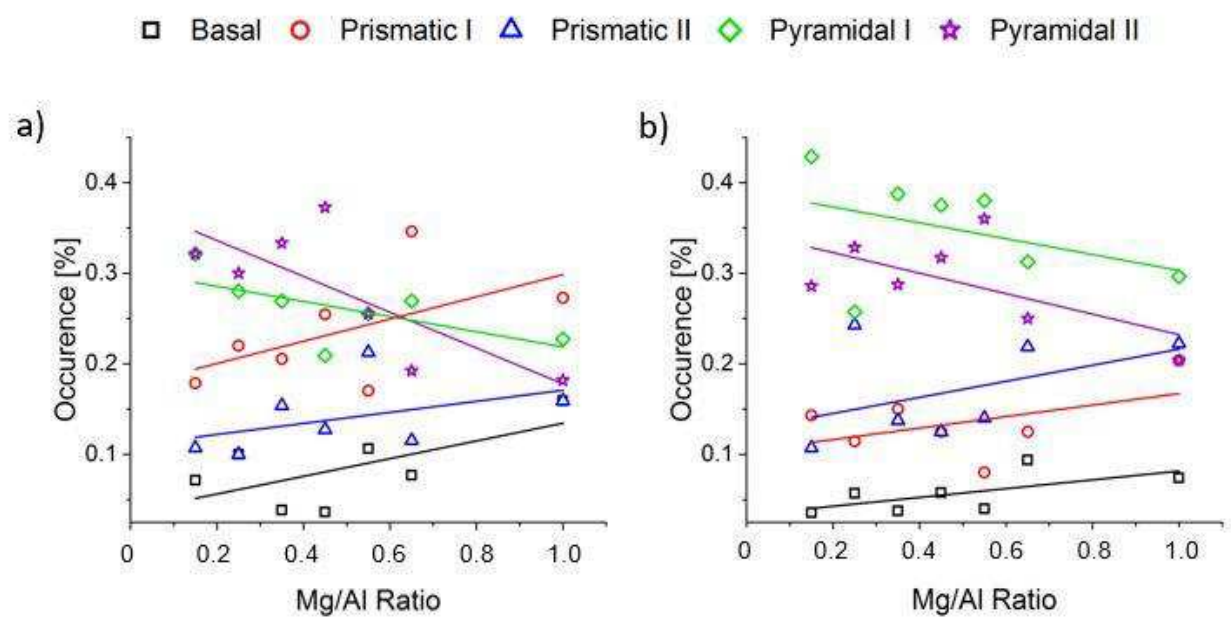

FIGURE 11: OCCURRENCE OF DIFFERENT SLIP PLANES FOR DIFFERENT MG/AL RATIOS AND THE 45°(0001) (A) AND 90°(0001) (B) ORIENTATION. FOR BOTH ORIENTATIONS, BASAL, PRISMATIC 1ST AND 2ND SLIP INCREASES AND PYRAMIDAL 1ST AND 2ND SLIP DECREASES IN NUMBER DENSITY OF SLIP LINES WITH INCREASING MG CONTENT.

At first, a change in the activation of different slip systems could be observed (Figure 11). Including the data points from the C14 phase, one can see that for both orientations, the $45°(0001)$ and $90°(0001)$ orientations both pyramidal slip planes show a decreasing activation with increasing Mg content, while basal and both prismatic slip systems increase in activation. The $0°(0001)$ orientation exhibited only very few slip lines per indent so that it was not possible to analyse the activation of slip systems in this orientation with sufficient reliability. Next to a change in activation of slip systems, the data showed an increasing amount of slip lines per indent and a decreasing amount of plastic instabilities with increasing Mg content for all three orientations (Figure 12).

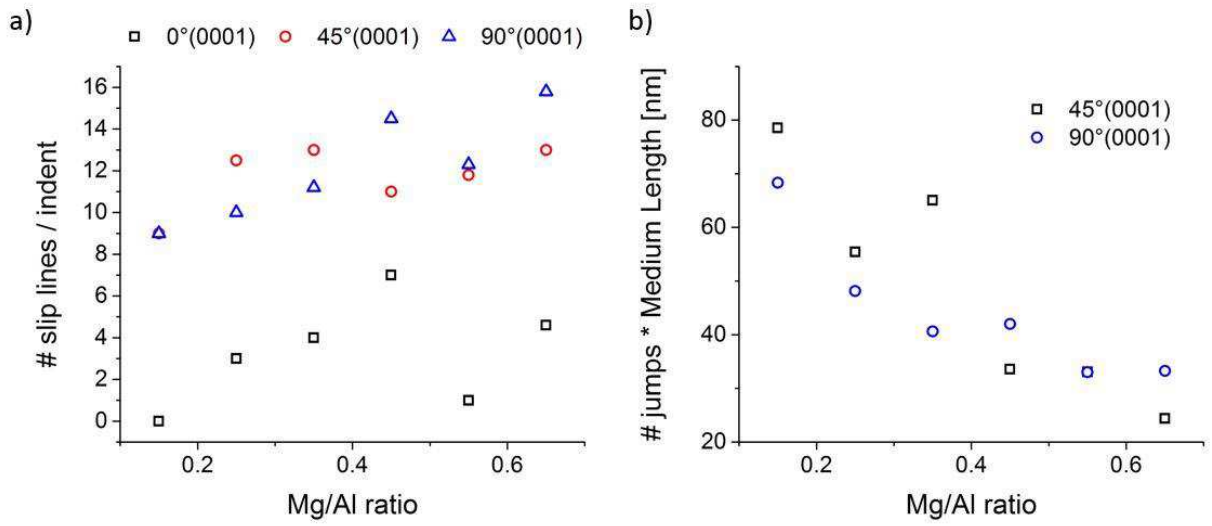

FIGURE 12: THE NUMBER OF SLIP LINES PER INDENT (A) AND THE AMOUNT OF PLASTIC INSTABILITIES (B) IN THE C36 PHASE. THE NUMBER OF SLIP LINES INCREASES WHILE THE AMOUNT OF PLASTIC INSTABILITIES DECREASES WITH INCREASING MG CONTENT FOR ALL TESTED ORIENTATIONS

4.5 EDX MEASUREMENTS OF THE C14, C15 AND C36 PHASE

EDX measurements were performed on the C14, C15 and C36 phase. Figure 13 displays the deviation from the exact stoichiometric composition of 66 at.-% B-atoms for all three phases and different Mg/Al ratios. It can be seen that the C15 phase crystallises close to the stoichiometric composition. The C14 phase forms with a significant deviation from the ideal composition. The C36 phase exhibits a linear trend from strongly off-stoichiometric (low Mg content) to close to the stoichiometric composition (high Mg content). Also the inaccuracies of EDX measurements are relatively high so that it is not possible to really determine the exact composition within a sufficiently low error bar to make a direct comparison to the mechanical properties, the method is accurate enough to show the general trends (e.g. close to the stoichiometric composition or off-stoichiometric).

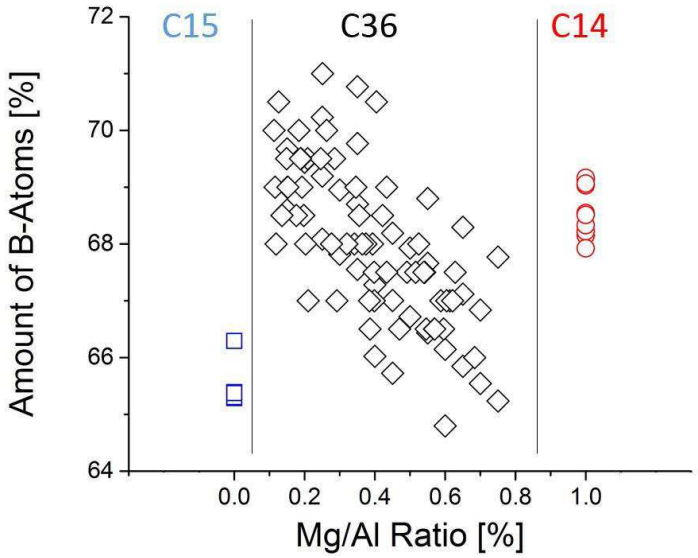

FIGURE 13: DEVIATION FROM THE STOICHIOMETRIC COMPOSITION WITH VARYING MG/AL RATIO FOR THE THREE DIFFERENT LAVES PHASES. WHILE THE C15 PHASE IS CLOSE THE STOICHIOMETRIC COMPOSITION, THE C14 PHASE DEVIATES SIGNIFICANTLY. THE C36 PHASE SHOWS A LINEAR TREND FROM OFF-STOICHIOMETRY (LOW MG CONTENT) TO STOICHIOMETRY (HIGH MG CONTENT)

5 DISCUSSION

5.1 NON-NEWTONIAN BEHAVIOR OF DIFFERENT GLASS MATERIALS AT HIGH STRAIN RATES

In this study, several different glass materials, ranging from the most anomalous glass (fused silica) to a glass representing the normal side (shear deformation) of deformation behaviour in glasses (a bulk metallic glass, BMG) was chosen. Additionally, a Sodium-Borosilicate glass was tested in a quenched and a annealed state, leading to a more open (quenched) or close packed (annealed) structure which are more prone to densification or shear, respectively. Finally, the stress state was varied by using a sharp cube corner (introducing more shear deformation) and a blunter Berkovich (introducing more densification) indenter geometry. By using impact nanoindentation, the deformation behaviour could be analysed over several orders of magnitude.

In glasses, the viscosity plays an important role. Typically, the stress needed to deform glasses at room temperature is proportional to the strain rate. This proportional factor is the viscosity η:

$$\sigma = \eta * \dot{\epsilon} \quad \textbf{(14)}$$

At low strain rates, most fluids show a linear viscosity and therefore a linear increase of stress with strain rate. At higher strain rates, some fluids show a decreasing (or increasing) strain rate and therefore, the stress levels off to a constant value instead of increasing with increasing strain rate. This behaviour is called non-Newtonian behaviour.

Target of this study was to evaluate if (and in which extend) Non-Newtonian behaviour can be observed in glasses at room temperature and if this can be correlated to a change in the deformation mechanisms of glass.

To answer the first question, if non-Newtonian behaviour can be observed in glasses at room temperature, the dynamic hardness was measured over several orders of magnitude for all described glass systems and plotted over the strain rate:

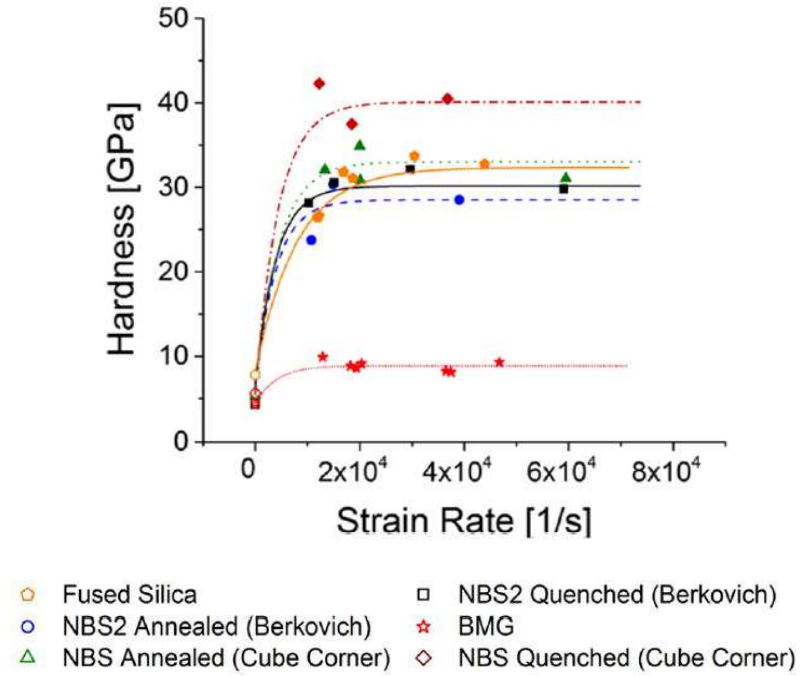

FIGURE 14: DEVELOPMENT OF DYNAMIC HARDNESS WITH STRAIN RATE FOR DIFFERENT GLASS SYSTEMS. WITH INCREASING STRAIN RATE, THE HARDNESS LEVELS OFF TO A CONSTANT VALUE, SHOWING NON-NEWTONIAN BEHAVIOR OF DIFFERENT GLASSES AT ROOM TEMPERATURE.

It could also be shown that by dividing the measured constant hardness at high strain rates by the theoretical hardness of the investigated glass system, all glasses converge towards a common value of ~ 70 % of their theoretical hardness:

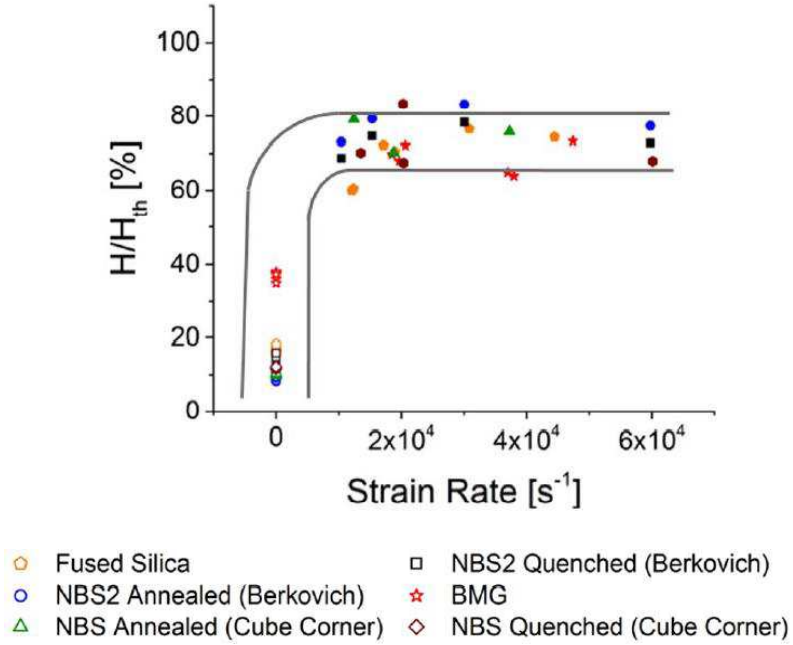

FIGURE 15: BY DIVIDING THE MEASURED CONSTANT HARDNESS AT HIGH STRAIN RATES BY THE THEORETICAL HARDNESS OF THE INDIVIDUAL GLASS SYSTEM, IT CAN BE SHOWN THAT ALL GLASS SYSTEMS CONVERGE TOWARDS A COMMON VALUE OF ~ 70 % OF THEIR THEORETICAL HARDNESS.

In a second step, the amount of plastic and elastic deformation introduced into the different glass systems were measured for different strain rates. From the Impact nanoindentation experiments, the energy loss ratio with the first impact was analysed. Since densification is a reversible process, this mechanism is expected to show a higher elastic portion, while non-reversible shear deformation should show a higher amount of plastic deformation. A second set of experiments measured the amount of recovered (reversible) volume after annealing treatment using AFM (Figure 16).

Both sets of experiments show the expected trend for the different glass materials. From the most open structure (fused silica), over annealed and then quenched NBS glass tested with a flat Berkovich tip, annealed and then quenched NBS glass tested with a sharp Cube Corner tip up to the most compact structure (BMG), one can see an increase of shear deformation.

Next to the structure, it is remarkable, that also a shift from densification to shear deformation can be seen for all materials in a similar way with increasing strain rate, connecting the occurrence of non-Newtonian behaviour to the deformation mechanism of the investigated glasses, independent of their differences in structure.

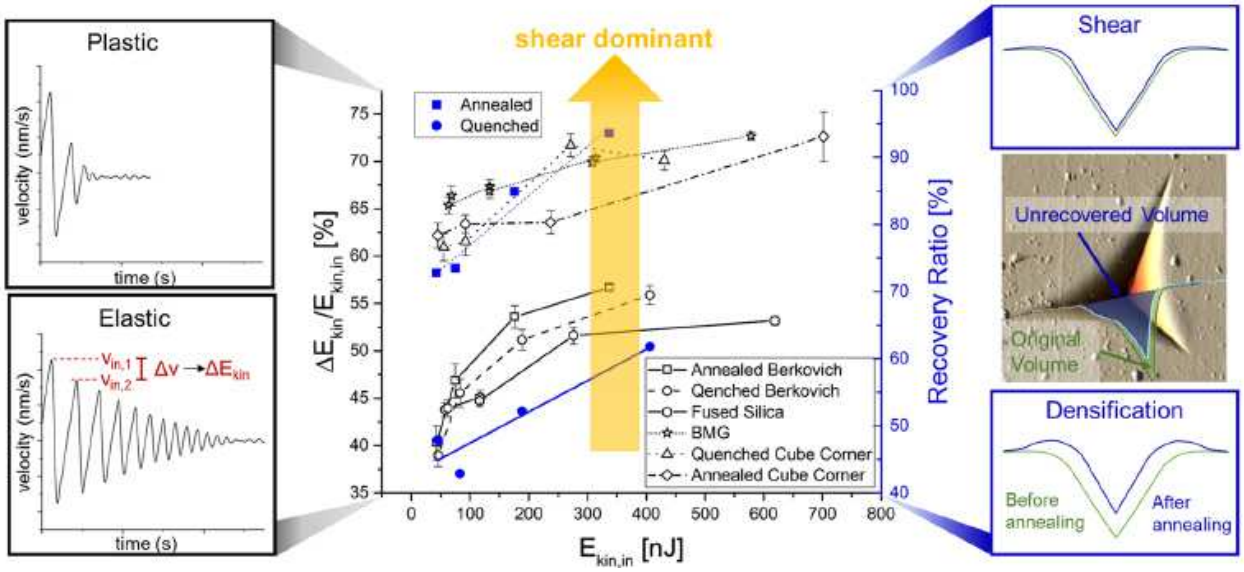

FIGURE 16: INFLUENCE OF STRAIN RATE ON THE DEFORMATION BEHAVIOUR OF DIFFERENT GLASS STRUCTURES. ON THE LEEFT AXIS, THE ENERGY LOSS WITH THE FIRST IMPACT, REPRESENTING THE AMOUNT OF PLASTIC VS. ELASTIC DEFORMATION IS OUTLINED. ON THE RIGHT AXIS, RESULTS FROM ANNEALING EXPERIMENTS ARE SHOWN WHICH DISPLAY THE AMOUNT OF RECOVERED VOLUME AFTER ANNEALING TREATMENT ARE DISPLAYED.

5.2 APPLICATION OF NANOINDENTATION EXPERIMENTS AT HIGH TEMPERATURES

For the first time, it was possible to perform nanoindentation experiments at 1000 °C. The problems of conducting these sort of experiments are mainly the challenge to ensure a thermally stable system during repeatedly bringing the tip and the sample in and out of contact as well as to inhibit chemical interaction between the tip and the sample, leading to drastic changes in the tip geometry at high temperatures, even after only a few indentation cycles. The tip material is therefore the limiting factor inhibiting an expansion of the application temperature of nanoindentation experiments to temperatures above 1000 °C.

5.3 INFLUENCE OF TEMPERATURE ON THE ACTIVATION OF SLIP SYSTEMS IN THE C14 PHASE

The deformation behaviour of the C14 Mg2Ca Laves phase was investigated. For room temperature, the CRSS values determined in micropillar compression experiments fit very well to the activation of different slip systems determined in nanoindentation experiments. A negative deviation of the activation measured experimentally from the theoretical value determined by the geometrical analysis (i.e. that this slip system was less often activated than proposed by pure geometry) should correspond to a hard slip system and therefore to a high CRSS and vice versa. This behaviour can indeed be observed (Table 10): basal and pyramidal 2nd order slip, which have been activated approximately with the same frequency as predicted by the geometrical analysis exhibit a similar CRSS. Prismatic 1st order slip was activated with a higher frequency and correspondingly exhibits a lower CRSS. Pyramidal 2nd order slip on the other hand was less often activated than predicted by pure geometry and shows the expected high CRSS. Unfortunately, it was not possible to activate prismatic 2nd order slip during micropillar compression despite micropillar being oriented for a high Schmid factor on this slip system. This speaks for a high CRSS value and fits the negative deviation from the geometrical analysis.

To investigate the reason for the similar CRSS values, the basal and the 1st order pyramidal plane have been compared and it was found that an atomic arrangement similar to the one responsible for the synchroshear mechanism in the basal plane is as well present in the pyramidal 1st order plane. It is furthermore missing in the other slip planes. This would give an explanation why the CRSS values of the basal and the pyramidal 1st order plane are so similar.

At high temperatures, the correlation between the micropillar compression and the nanoindentation experiments stays valid for most temperatures and slip systems. The only deviation is pyramidal 1st order slip, where the CRSS stays constant between RT and 150 °C but the activation increases $(7°(0001))$ or decreases $(44°(0001))$. A possible reason for this deviation was found to be the specific arrangements of the pyramidal slip planes for these orientations.

Next to a change in activation of slip systems, the experiments revealed a PLC effect at low temperatures which decreased in magnitude with increasing temperature. In addition, the number of slip lines decreased with increasing temperature. Finally, the SRS was found to be close to zero and arguably negative for some temperatures. Three different options could be the possible reason for these findings.

The first one is that with increasing temperature, cross-slip or dislocation glide become active. This is furthermore supported by a decreasing CRSS value for pyramidal slip, where cross-slip can occur in Mg. However, no change in SRS, no significant hardening effect in micropillar compression experiments as well as TEM images from HT-samples contradict this argumentation.

The second theory is that with increasing temperature, oxidation takes place which makes it simply more difficult to detect the slip lines on the surface. Since the experiments have been performed under high vacuum ($< 10^{-5}$ Pa) and very fine structures e.g. inside the indents can still be seen, this is not considered as a reliable explanation. Furthermore, oxidation would not explain the reduction of serrated yielding.

The next idea is that all these findings are connected to the PLC effect. Though the concept of the PLC effect is relatively old, the exact mechanism behind it are still under debate [110]. Usually, a PLC effect or serrated yielding is correlated to the interaction of dislocations and solute atoms, called dynamic strain ageing (DSA) [110-116]. This mechanism describes the alternating processes of solute atoms diffusing to a dislocation and pinning it and the dislocation ripping free from the attached solute atoms and moving to the next obstacle [110, 112-114]. The process depends on several parameters, e.g. the diffusibility and concentration of solute atoms or the number of obstacles for dislocation motion. As it also depends on the ability of dislocations to move freely and to overcome obstacles, it also depends on extrinsic parameters, especially the strain rate and the temperature [110]. While it is generally accepted that an increase in temperature leads to a decrease in the amount of DSA, the effect of strain rate is less clear. However, it is as well accepted that DSA leads to a decrease in SRS and possibly even to a nSRS [110, 112-115]. Both conditions are met in this study: the magnitude of the PLC effect decreases with increasing temperature and a surprisingly low SRS, debatably even negative at some temperatures can be observed. Furthermore, the C14 phase showed a deviation from the stoichiometric composition (e.g. the presence of solute atoms) in EDX measurements. C15 phase did not show a PLC effect and showed a composition close to the stoichiometric composition in EDX measurements. Finally, it is reported that, if all three Laves phases are present in one system (as it is the case in the Mg-Al-Ca system), the C15 phase usually precipitates with the stoichiometric composition while the C14 and the C36 phase crystallise with off-stoichiometry [28].

The PLC effect would also help explaining the reducing number of slip lines with increasing temperature: compression tests at high temperatures revealed that compositions that even slightly deviate from the ideal AB_2 composition (<2 % deviation) already lead to a significantly increased amount of active

dislocation sources. A strong deviation from the stoichiometric composition would therefore lead to a high number of active dislocation source and thus to homogeneous deformation and a low number of slip lines. However, it was proposed by Klose et al.[117] that in systems where DSA takes place, several fresh (i.e. unpinned) dislocations can pile up behind a pinned dislocation. When the leading dislocation breaks free, a large amount of dislocations simultaneously starts to move, resulting in a strain burst [118, 119]. This would mean that in the low temperature regime, where the PLC effect is pronounced, dislocation movement would still be restricted to single glide planes due to a coordinated dislocation motion from DSA, even though a large amount of dislocation sources could be active because of the anti-site defects. When temperatures increase (and the PLC effect decreases), dislocation motion becomes less localised and therefore the high amount of dislocation sources can be active, resulting in a more homogeneous deformation. This mechanism would explain the loss of slip lines with increasing temperature.

Extensive studies are needed to fully answer which or how many of these assumptions are valid, including high resolution TEM (HR-TEM), neutron scattering as well as DFT to simulate stacking fault energies (SFE). As this is the first systematic study to investigate a statistical data set about the deformation mechanisms of the C14 Laves phase at temperatures far below the brittle-to-ductile transition temperature, the hypotheses given in this study nevertheless give a good starting point for further studies.

5.4 INFLUENCE OF COMPOSITION ON THE ACTIVATION OF SLIP SYSTEMS IN THE C36 PHASE

In the cubic C15 phase, the $\{111\}$ plane was the least often activated slip plane. This result is surprising, as most studies performed at HT state that this should be the dominant slip system. On the other hand, basal slip is as well the dominant slip system in the C14 and C36 phase at HT while this study revealed that at room temperature, it is the least often activated slip system. Remarkable is that by including the four slip systems known to occur in the C15 phase – $\{111\}$, $\{110\}$, $\{001\}$ and $\{112\}$ – 94 % of all slip lines can be assigned to one of these slip systems stating that indeed these are sufficient to describe dislocation activation in the C15 phase.

In the C36 phase, a high number of slip lines belonged to non-basal planes. Unlike in the C14 phase [39], there is no theoretical consideration of possible Burgers vectors for the C36 phase. Due to the complexity and the large unit cell it is implausible, though, to expect perfect $< c + a >$ or $< c >$

dislocations. Instead, partial dislocations are more probable, e.g. as discussed in the idea of "zonal glide" [48]. In this study, a first attempt was undertaken to construct possible Burgers vectors in the pyramidal 1st and 2nd order as well as the prismatic 2nd order slip plane.

One main focus when investigating the deformation mechanism of the C36 phase is the chemical composition. The C36 phase can vary the chemical composition quite extensively without changing the crystal structure, different to the C14 and the C15 phase. The Mg-Al ratio can thereby vary between $(Mg_{10}Al_{90})_2Ca$ and $(Mg_{70}Al_{30})_2Ca$. Amerioun et al. [120] determined which positions are most likely to be occupied by Mg or Al atoms. Combining this information with the position of the partial dislocations determined in this study reveals that 1st and 2nd order pyramidal planes both pass mostly through atoms that are the first ones to be occupied by Al atoms. Basal and prismatic slip planes on the other hand mostly contain positions where Mg atoms are energetically favourable to be placed. Arguing that – due to its bigger diameter – a single Mg atom in an Al-rich slip plane has a detrimental effect on the activation of this slip system, while the effect of a single Al atom in an Mg-rich slip plane should not be as grave as the first case, one would expect to see the activation of basal and prismatic slip to increase with increasing Mg content and the activation of pyramidal slip to increase with increasing Al content. Both assumptions are met as is shown in Figure 11.

The C36 phase showed plastic instabilities and a diverging number of slip lines around the indents – similar to the C14 phase. However, in this case these characteristics did not change with temperature but with varying Mg-Al ratio: for high Mg contents, the number of slip lines increased while the amount of plastic instabilities decreased. Two possible explanations for this behaviour are presented and discussed. The first thesis is that the PLC effect is connected to pyramidal slip, as not only the number of slip lines but also the activation of pyramidal slip showed an increasing trend with increasing Mg-Al-ratio. However, in the HT experiments on the C14 phase, this behaviour could not be observed but rather the opposite trend. One could argue that the effect of a change in pyramidal slip is superimposed with the effect of a change in temperature. This remains to be investigated.

The second assumption is that these findings are connected to the occurrence of DSA. It was found that even small deviations from the exact stoichiometric composition (< 2 %) already change the deformation mode significantly, e.g. by introducing anti-site defects that can pin dislocations (and therefore lead to plastic instabilities). Next to plastic instabilities (due to dislocation-solute interaction, e.g. pinning) one should see an increase in hardness. Both conditions are met in this study. Finally, anti-site defect display

possible dislocation sources in Laves phases, i.e. with increasing off-stoichiometry the number of anti-site defects should increase which would in turn result in more dislocation and therefore to a more homogeneous deformation and less slip lines per indent. This can as well be observed in our data.

Again, this is supported by the EDX measurements and the fact that the C15 phase usually can be found near the stoichiometric composition while C14 and C36 are usually off-stoichiometric (if all three phases appear in one system at the same temperature) [28]. The C15 phase does not show serrated yielding.

In section 5.1, the C14 phase showed a decreasing amount of slip lines with increasing temperature and this was correlated to the decreasing occurrence of DSA. In the C36 phase, however, these two characteristics show diverging trends. The reason for this is found in the extent of the PLC effect. In the C36 phase, the maximum value for the product between the number and the mean distance of displacement jumps (as a measurement of the extent of the PLC effect) reaches 78 nm (at a high Al content). The C14 phase exhibits a similar value at 200 °C. At room temperature, the product reaches values of 370 nm, which is 4.5 times higher than the maximum value in the C36 phase. Therefore, the effect of DSA on the homogeneity of slip is not as pronounced in the C36 phase as in the C14 phase and the effect of off-stoichiometry (with the increasing amount of active dislocation sources) is much more dominant in the C36 phase. The effect of these two mechanism is displayed in Figure 17.

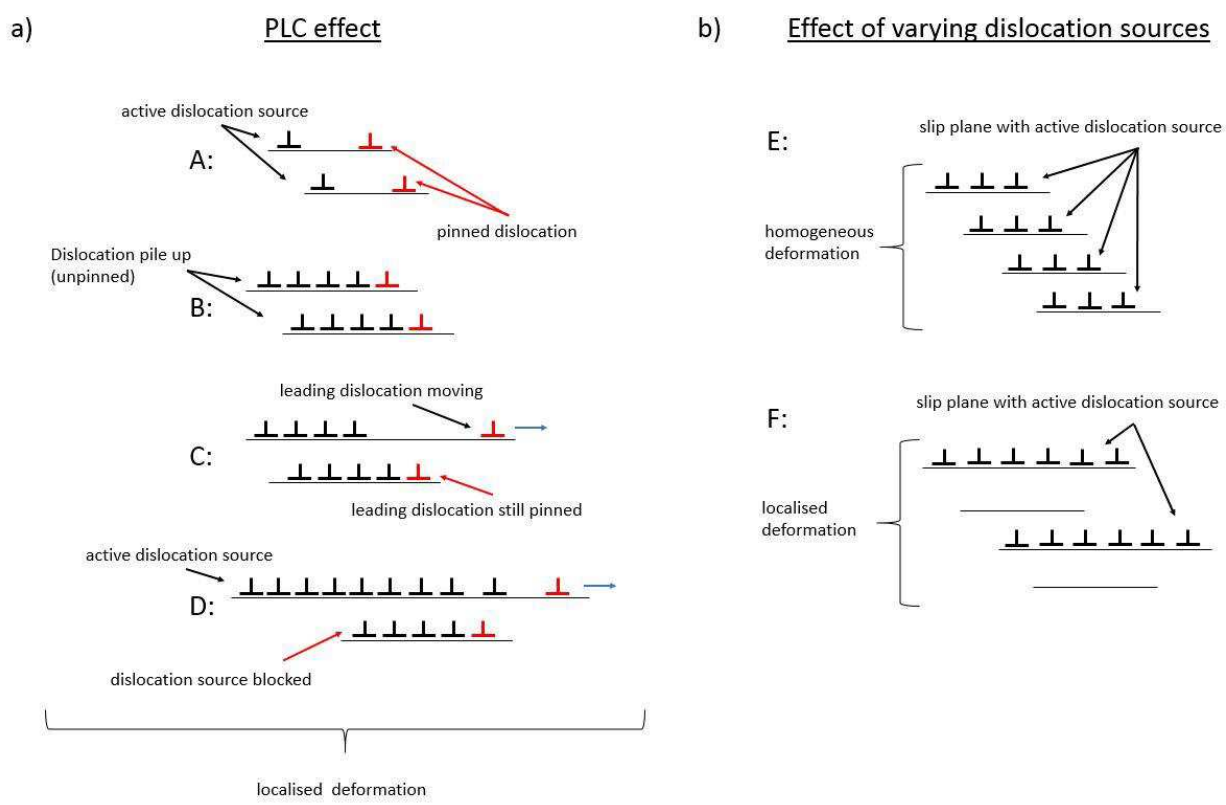

FIGURE 17:SCHEME FOR DESCRIBING THE INFLUENCE OF THE PLC EFFECT (A) AND OF VARYING DISLOCATION SOURCES (B) ON THE HOMOGENEITY OF SLIP.

Similar to the findings in the C14 phase, one would need further, high resolving techniques to identify how many and which of the discussed theses are active in this material.

6 CONCLUSION

A combination of micromechanical testing (nanoindentation and micropillar compression) and electron microscopy (SE, EBSD, TEM) was used to investigate the deformation behaviour of the three Laves phases in the Mg-Al-Ca system at temperatures between RT and 250 °C. The analysis comprised the determination of CRSS values and comparing these to statistical information about the activation of different slip systems. SRS and the amount of plastic instabilities were measured and discussed against the background of the crystal structure and dislocation structures, supported by TEM. The main findings are:

- Statistical analysis of slip steps formed around nanoindentations in the C14 phase at room temperature suggested a scaling of the critical resolved shear stresses as follows: 1st order prismatic < basal ≈ 1st order pyramidal < 2nd order pyramidal slip ≤ 2nd order prismatic. The CRSS values followed this order: $\tau_{Pris\ 1^{st}} = 0.44\ GPa < \tau_{basal} = 0.52\ GPa \approx \tau_{pyr1^{st}} = 0.53\ GPa < \tau_{pyr2^{nd}} = 0.59\ GPa$
- For low temperatures, a PLC effect was determine in the C14 phase, decreasing with increasing temperature. This is accompanied by a low, possibly negative SRS, speaking for the occurrence of DSA and therefore for the presence of solute atoms
- With increasing testing temperature, the amount of slip lines decreased as well in the C14 phase. Three possibilities are presented, namely dislocation climb, cross-slip and the effect of off-stoichiometry. As several findings contradict climb and cross-slip, the reason for this behaviour was found to be an increasing number of dislocation sources with increasing off-stoichiometry, as determined in macroscopic tests
- The C15 phase showed four different slip systems being activated. The most often activated one is $\{110\}$ with 34 % of all slip lines accounted to this slip plane. The others are $\{100\}$ with 27 %, $\{112\}$ with 19 % and $\{111\}$ with 14 %.
- The C36 phase showed several trends when shifting the Mg-Al-ratio towards higher Mg contents: pyramidal slip increased, basal and prismatic slip decreased in extend, the number of slip lines increased and the magnitude of plastic instabilities decreased with increasing Mg content. Additionally, the hardness decreased with increasing Mg content.
- While it is not assumed that the change in slip lines and plastic instabilities is connected to a change in activation of slip systems, these findings are correlated to the effect of off-stoichiometry. It is argued that the incorporation of bigger Mg atoms into Al-preferred positions leads to slight off-stoichiometry. This in turn leads to the plastic instabilities as well as the change in hardness.

7 REFERENCES

[1] D. Amberger, "Einfluss der eutektischen Phase auf die Kriechfestigkeit kalziumhaltiger Magnesiumlegierungen," PhD, Technische Fakultät der Universität Erlangen-Nürnberg, Universität Erlangen-Nürnberg, Erlangen, 2011.

[2] D. Amberger, P. Eisenlohr, and M. Göken, "Microstructural evolution during creep of Ca-containing AZ91," *Materials Science and Engineering: A,* vol. 510–511, no. 0, pp. 398-402, 6/15/ 2009, doi: http://dx.doi.org/10.1016/j.msea.2008.04.115.

[3] D. Amberger, P. Eisenlohr, and M. Göken, "On the importance of a connected hard-phase skeleton for the creep resistance of Mg alloys," *Acta Materialia,* vol. 60, no. 5, pp. 2277-2289, 3// 2012, doi: http://dx.doi.org/10.1016/j.actamat.2012.01.017.

[4] B. Backes, K. Durst, D. Amberger, and M. Göken, "Particle Hardening in Creep-Resistant Mg-Alloy MRI 230D Probed by Nanoindenting Atomic Force Microscopy," (in English), *Metall and Mat Trans A,* vol. 40, no. 2, pp. 257-261, 2009/02/01 2009, doi: 10.1007/s11661-008-9720-1.

[5] H. Eibisch, A. Lohmüller, N. Kömpel, and R. F. Singer, "Effect of solidification microstructure and Ca additions on creep strength of magnesium alloy AZ91 processed by Thixomolding," *International Journal of Materials Research,* vol. 99, no. 1, pp. 56-66, 2008/01/01 2008, doi: 10.3139/146.101604.

[6] L. Han, D. O. Northwood, X. Nie, and H. Hu, "The effect of cooling rates on the refinement of microstructure and the nanoscale indentation creep behavior of Mg–Al–Ca alloy," *Materials Science and Engineering: A,* vol. 512, no. 1–2, pp. 58-66, 6/25/ 2009, doi: http://dx.doi.org/10.1016/j.msea.2009.01.068.

[7] M. P. Liu, Q. D. Wang, X. Q. Zeng, G. Y. Yuan, Y. P. Zhu, and W. J. Ding, "Mechanical Properties and Creep Behavior of Mg–Al–Ca Alloys," *Materials Science Forum,* vol. 488, pp. 763-766 2005.

[8] A. Luo, B. R. Powell, and M. Balogh, "Creep and microstructure of magnesium-aluminum-calcium based alloys," (in English), *Metall and Mat Trans A,* vol. 33, no. 3, pp. 567-574, 2002/03/01 2002, doi: 10.1007/s11661-002-0118-1.

[9] K. Maruyama, M. Suzuki, and H. Sato, "Creep strength of magnesium-based alloys," (in English), *Metall and Mat Trans A,* vol. 33, no. 3, pp. 875-882, 2002/03/01 2002, doi: 10.1007/s11661-002-0157-7.

[10] Y. Mori, Y. Terada, and T. Sato, "Microstructure Stability and Creep Strength in a Die-Cast AX52 Magnesium Alloy," *MATERIALS TRANSACTIONS,* vol. 46, no. 8, pp. 1749-1752, 2005, doi: 10.2320/matertrans.46.1749.

[11] N. D. Saddock, A. Suzuki, J. W. Jones, and T. M. Pollock, "Grain-scale creep processes in Mg–Al–Ca base alloys: Implications for alloy design," *Scripta Materialia,* vol. 63, no. 7, pp. 692-697, 10// 2010, doi: http://dx.doi.org/10.1016/j.scriptamat.2010.03.055.

[12] T. Sato and M. V. Kral, "Microstructural evolution of Mg–Al–Ca–Sr alloy during creep," *Materials Science and Engineering: A,* vol. 498, no. 1–2, pp. 369-376, 12/20/ 2008, doi: http://dx.doi.org/10.1016/j.msea.2008.08.006.

[13] J. Su, S. Kaboli, A. S. Kabir, I.-H. Jung, and S. Yue, "Effect of dynamic precipitation and twinning on dynamic recrystallization of micro-alloyed Mg–Al–Ca alloys," *Materials Science and Engineering: A,* vol. 587, no. 0, pp. 27-35, 12/10/ 2013, doi: http://dx.doi.org/10.1016/j.msea.2013.08.019.

[14] M. Suzuki, A. Shibata, and K. Maruyama, "Creep behavior and Microstructures in Grain Boundary Strengthened Mg-Al-Ca Thixomolded® Alloys," *Materials Science Forum,* vol. 706-709, pp. 1249-1254, 2012.

[15] Y. Terada, D. Itoh, and T. Sato, "Dislocation analysis of die-cast Mg–Al–Ca alloy after creep deformation," *Materials Science and Engineering: A,* vol. 523, no. 1–2, pp. 214-219, 10/15/ 2009, doi: http://dx.doi.org/10.1016/j.msea.2009.07.001.

[16] Y. Terada, R. Sota, N. Ishimatsu, T. Sato, and K. Ohori, "A thousandfold creep strengthening by Ca addition in die-cast AM50 magnesium alloy," (in English), *Metall and Mat Trans A,* vol. 35, no. 9, pp. 3029-3032, 2004/09/01 2004, doi: 10.1007/s11661-004-0046-3.

[17] J. R. TerBush, A. Suzuki, N. D. Saddock, J. W. Jones, and T. M. Pollock, "Dislocation substructures of three die-cast Mg–Al–Ca-based alloys," *Scripta Materialia,* vol. 58, no. 10, pp. 914-917, 5// 2008, doi: http://dx.doi.org/10.1016/j.scriptamat.2008.01.015.

[18] M. Vogel, O. Kraft, and E. Arzt, "Creep behavior of magnesium die-cast alloy ZA85," *Scripta Materialia,* vol. 48, no. 8, pp. 985-990, 4/14/ 2003, doi: http://dx.doi.org/10.1016/S1359-6462(02)00588-2.

[19] S. Amerioun, S. I. Simak, and U. Häussermann, "Laves-Phase Structural Changes in the System CaAl2-xMgx," *Inorganic Chemistry,* vol. 42, no. 5, pp. 1467-1474, 2003/03/01 2003, doi: 10.1021/ic020596m.

[20] H. Cao *et al.*, "Experiments coupled with modeling to establish the Mg-rich phase equilibria of Mg–Al–Ca," *Acta Materialia,* vol. 56, no. 18, pp. 5245-5254, 10// 2008, doi: http://dx.doi.org/10.1016/j.actamat.2008.07.003.

[21] J. Gröbner, D. Kevorkov, I. Chumak, and R. Schmid-Fetzer, "Experimental investigation and thermodynamic calculation of ternary Al–Ca–Mg phase equilibria," *Z. Metallkd.,* vol. 94, no. 9, pp. 976-982, 2003.

[22] F. Islam and M. Medraj, "Thermodynamic Modelling of the Mg-Al-Ca-System," *Canadian Metallurgical Quarterly,* vol. 44, no. 3, pp. 1 - 14, 2005.

[23] D. Kevorkov, M. Medraj, J. Li, E. Essadiqi, and P. Chartrand, "The 400°C isothermal section of the Mg–Al–Ca system," *Intermetallics,* vol. 18, no. 8, pp. 1498-1506, 8// 2010, doi: http://dx.doi.org/10.1016/j.intermet.2010.03.038.

[24] K. Ozturk, Y. Zhong, Z.-K. Liu, and A. Luo, "Creep resistant Mg-Al-Ca alloys: Computational thermodynamics and experimental investigation," (in English), *JOM,* vol. 55, no. 11, pp. 40-44, 2003/11/01 2003, doi: 10.1007/s11837-003-0208-6.

[25] A. Suzuki, N. D. Saddock, J. W. Jones, and T. M. Pollock, "Structure and transition of eutectic (Mg,Al)2Ca Laves phase in a die-cast Mg–Al–Ca base alloy," *Scripta Materialia,* vol. 51, no. 10, pp. 1005-1010, 11// 2004, doi: http://dx.doi.org/10.1016/j.scriptamat.2004.07.011.

[26] H. N. Mathur, V. Maier-Kiener, and S. Korte-Kerzel, "Deformation in the γ-Mg17Al12 phase at 25–278 °C," *Acta Materialia,* vol. 113, pp. 221-229, 7// 2016, doi: http://dx.doi.org/10.1016/j.actamat.2016.05.001.

[27] F. Stein, M. Palm, and G. Sauthoff, "Structure and stability of Laves phases. Part I. Critical assessment of factors controlling Laves phase stability," *Intermetallics,* vol. 12, no. 7–9, pp. 713-720, 7// 2004, doi: http://dx.doi.org/10.1016/j.intermet.2004.02.010.

[28] F. Stein, M. Palm, and G. Sauthoff, "Structure and stability of Laves phases part II—structure type variations in binary and ternary systems," *Intermetallics,* vol. 13, no. 10, pp. 1056-1074, // 2005, doi: http://dx.doi.org/10.1016/j.intermet.2004.11.001.

[29] H. Kubsch, P. Paufler, and G. E. R. Schulze, "The mobility of grown-in dislocations in the intermetallic compound MgZn2 during prismatic slip," *physica status solidi (a),* vol. 25, no. 1, pp. 269-275, 1974, doi: 10.1002/pssa.2210250125.

[30] H. Kubsch, P. Paufler, and G. E. R. Schulze, "The Mobility of Grown-in Dislocations in the Intermetallic Compound MgZn2. III. Dependence of Basal Slip on Chemical Composition within the Homogeneity Range and on Temperature," *physica status solidi (b),* vol. 56, no. 1, pp. 231-234, 1973, doi: 10.1002/pssb.2220560121.

[31] T. H. Mueller and P. Paufler, "Yield strength of the monocrystalline intermetallic compound MgZn2," *physica status solidi (a),* vol. 40, no. 2, pp. 471-477, 1977, doi: 10.1002/pssa.2210400213.

[32] "Chapter 4 - Frictional Forces in Metals," in *Pergamon Materials Series*, vol. 8, D. Caillard and J. L. Martin Eds.: Pergamon, 2003, pp. 85-123.

[33] A. V. Kazantzis, M. Aindow, G. K. Triantafyllidis, and J. T. M. De Hosson, "On the self-pinning character of synchro-Shockley dislocations in a Laves phase during strain rate cyclical compressions," *Scripta Materialia,* vol. 59, no. 7, pp. 788-791, 2008/10/01/ 2008, doi: https://doi.org/10.1016/j.scriptamat.2008.06.024.

[34] T. Rzychoń, "Characterization of Mg-rich clusters in the C36 phase of the Mg–5Al–3Ca–0.7Sr–0.2Mn alloy," *Journal of Alloys and Compounds,* vol. 598, no. 0, pp. 95-105, 6/15/ 2014, doi: http://dx.doi.org/10.1016/j.jallcom.2014.02.029.

[35] S. Scudino, P. Donnadieu, K. B. Surreddi, K. Nikolowski, M. Stoica, and J. Eckert, "Microstructure and mechanical properties of Laves phase-reinforced Fe–Zr–Cr alloys," *Intermetallics,* vol. 17, no. 7, pp. 532-539, 7// 2009, doi: http://dx.doi.org/10.1016/j.intermet.2009.01.007.

[36] N. Takata, H. Ghassemi-Armaki, M. Takeyama, and S. Kumar, "Nanoindentation study on solid solution softening of Fe-rich Fe2Nb Laves phase by Ni in Fe–Nb–Ni ternary alloys," *Intermetallics,* vol. 70, pp. 7-16, 2016/03/01/ 2016, doi: https://doi.org/10.1016/j.intermet.2015.11.003.

[37] T. Takasugi, S. Hanada, and M. Yoshida, "High temperature mechanical properties of C15 Laves phase Cr2Nb intermetallics," *Materials Science and Engineering: A,* vol. 192-193, pp. 805-810, 1995/02/28/ 1995, doi: https://doi.org/10.1016/0921-5093(94)03319-6.

[38] D. Hinz, P. Paufler, and G. E. R. Schulze, "Temperature Change Experiments during Secondary Creep of the Intermetallic Compound MgZn2," *physica status solidi (b),* vol. 36, no. 2, pp. 609-615, 2006, doi: 10.1002/pssb.19690360224.

[39] U. Krämer and G. E. R. Schulze, "Gittergeometrische Betrachtung der plastischen Verformung von Lavesphasen," *Kristall und Technik,* vol. 3, no. 3, pp. 417-430, 1968, doi: 10.1002/crat.19680030308.

[40] T. Müller, H. Krahl, P. Paufler, A. Lamsa, and G. E. R. Schulze, "Gleitbanduntersuchungen während und nach Verformung der intermetallischen Verbindung MgZn2," *Kristall und Technik,* vol. 7, no. 11, pp. 1249-1264, 2006, doi: 10.1002/crat.19720071109.

[41] P. Paufler, "Deformation-mechanism maps of the intermetallic compound MgZn2," *Kristall und Technik,* vol. 13, no. 5, pp. 587-590, 1978, doi: 10.1002/crat.19780130522.

[42] P. Paufler, "Early work on Laves phases in East Germany," *Intermetallics,* vol. 19, no. 4, pp. 599-612, 2011/04/01/ 2011, doi: http://dx.doi.org/10.1016/j.intermet.2010.11.032.

[43] P. Paufler, J. Marschner, and G. E. R. Schulze, "The Mobility of Grown-in Dislocations in the Intermetallic Compound MgZn2 I. Stress Dependence for Edge Dislocations in Prism Slip at 390 °C," *physica status solidi (b),* vol. 40, no. 2, pp. 573-579, 1970, doi: 10.1002/pssb.19700400216.

[44] P. Paufler, J. Marschner, and G. E. R. Schulze, "The Mobility of Grown-in Dislocations in the Intermetallic Compound MgZn2 II. Stress Dependence of Basal Slip at 390 °C," *physica status solidi (b),* vol. 43, no. 1, pp. 279-282, 1971, doi: 10.1002/pssb.2220430128.

[45] P. Paufler and G. E. R. Schulze, "Gleitsysteme innermetallischer Verbindungen," *Kristall und Technik,* vol. 2, no. 4, pp. K11-K14, 1967, doi: 10.1002/crat.19670020421.

[46] P. Paufler and G. E. R. Schulze, "Plastic Deformation of the Intermetallic Compound MgZn2," *physica status solidi (b),* vol. 24, no. 1, pp. 77-87, 1967, doi: 10.1002/pssb.19670240107.

[47] Y. Liu, S. M. Allen, and J. D. Livingston, "Deformation Mechanisms in a Laves Phase," *MRS Proceedings,* vol. 288, 1992, Art no. 203, doi: 10.1557/PROC-288-203.

[48] Y. Liu, S. M. Allen, and J. D. Livingston, "Deformation of two C36 laves phases by microhardness indentation at room temperature," (in English), *Metall and Mat Trans A,* vol. 26, no. 5, pp. 1107-1112, 1995/05/01 1995, doi: 10.1007/BF02670607.

[49] Y. Liu, J. D. Livingston, and S. M. Allen, "Room-temperature deformation and stress-induced phase transformation of laves phases in Fe-10 At. Pct Zr alloy," (in English), *MTA,* vol. 23, no. 12, pp. 3303-3308, 1992/12/01 1992, doi: 10.1007/BF02663439.

[50] Y. Liu, J. D. Livingston, and S. M. Allen, "Defect structures and nonbasal slip of C36 laves phase MgNi2 in a two-phase alloy," *Metall and Mat Trans A,* vol. 26, no. 6, pp. 1441-1447, 1995/06/01 1995, doi: 10.1007/BF02647594.

[51] A. V. Kazantzis, M. Aindow, and I. P. Jones, "Deformation behaviour of the C15 Laves phase Cr2Nb," *Materials Science and Engineering: A,* vol. 233, no. 1, pp. 44-49, 1997/08/15/ 1997, doi: https://doi.org/10.1016/S0921-5093(97)00047-6.

[52] W.-Y. Kim, D. E. Luzzi, and D. P. Pope, "Room temperature deformation behavior of the Hf–V–Ta C15 Laves phase," *Intermetallics,* vol. 11, no. 3, pp. 257-267, 2003/03/01/ 2003, doi: https://doi.org/10.1016/S0966-9795(02)00246-7.

[53] S. Korte and W. J. Clegg, "Studying Plasticity in Hard and Soft Nb–Co Intermetallics," *Advanced Engineering Materials,* vol. 14, no. 11, pp. 991-997, 2012, doi: 10.1002/adem.201200175.

[54] N. Takata, H. Ghassemi Armaki, Y. Terada, M. Takeyama, and K. S. Kumar, "Plastic deformation of the C14 Laves phase (Fe,Ni)2Nb," *Scripta Materialia,* vol. 68, no. 8, pp. 615-618, 4// 2013, doi: http://dx.doi.org/10.1016/j.scriptamat.2012.12.019.

[55] N. Takata, H. Ghassemi-Armaki, Y. Terada, M. Takeyama, and S. Kumar, "Effect of Dislocation Sources on Slip in Fe2Nb Laves Phase with Ni in Solution," *MRS Proceedings,* vol. 1516, pp. 269-274, 2012, doi: 10.1557/opl.2012.1566.

[56] M. L. Kronberg, "Plastic deformation of single crystals of sapphire: Basal slip and twinning," *Acta Metallurgica,* vol. 5, no. 9, pp. 507-524, 1957/09/01/ 1957, doi: https://doi.org/10.1016/0001-6160(57)90090-1.

[57] Y. T. Zhou, Y. B. Xue, D. Chen, Y. J. Wang, B. Zhang, and X. L. Ma, "Atomic-scale configurations of synchroshear-induced deformation twins in the ionic MnS crystal," *Scientific Reports,* Article vol. 4, p. 5118, 05/30/online 2014, doi: 10.1038/srep05118.

[58] P. M. Hazzledine and P. Pirouz, "Synchroshear transformations in Laves phases," *Scripta Metallurgica et Materialia,* vol. 28, no. 10, pp. 1277-1282, 1993/05/15/ 1993, doi: https://doi.org/10.1016/0956-716X(93)90468-8.

[59] M. F. Chisholm, S. Kumar, and P. Hazzledine, "Dislocations in Complex Materials," *Science,* vol. 307, no. 5710, pp. 701-703, February 4, 2005 2005, doi: 10.1126/science.1105962.

[60] K. S. Kumar and P. M. Hazzledine, "Polytypic transformations in Laves phases," *Intermetallics,* vol. 12, no. 7, pp. 763-770, 2004/07/01/ 2004, doi: https://doi.org/10.1016/j.intermet.2004.02.017.

[61] S. Schröders, S. Sandlöbes, B. Berkels, and S. Korte-Kerzel, "On the structure of defects in the Fe7Mo6 μ-Phase," *Acta Materialia,* vol. 167, pp. 257-266, 2019/04/01/ 2019, doi: https://doi.org/10.1016/j.actamat.2019.01.045.

[62] K. Eichler, H. Kubsch, T. Müller, and P. Paufler, "Änderung von Verformungseigenschaften der intermetallischen Verbindung MgZn2 im Homogenitätsbereich," *Kristall und Technik,* vol. 11, no. 11, pp. 1185-1188, 1976/01/01 1976, doi: 10.1002/crat.19760111110.

[63] L. M. Pike, I. M. Anderson, C. T. Liu, and Y. A. Chang, "Site occupancies, point defect concentrations, and solid solution hardening in B2 (Ni,Fe)Al," *Acta Materialia,* vol. 50, no. 15, pp. 3859-3879, 2002/09/03/ 2002, doi: https://doi.org/10.1016/S1359-6454(02)00192-1.

[64] P. K. Liaw, C. T. Liu, L. M. Pike, and J. H. Zhu, "Point Defects in Binary Laves-Phase Alloys,"; Oak Ridge National Laboratory; Oak Ridge, TN, ORNL/Sub/93-SP173/03; Other: ON: DE00002723 United States 10.2172/2723 Other: ON: DE00002723 ORNL English, 1999. [Online]. Available: http://www.osti.gov/scitech/servlets/purl/2723

[65] L. M. Pike, Y. A. Chang, and C. T. Liu, "On the Correlation of the Hardness of B2 Compounds with Point Defect Concentrations," *MRS Proceedings,* vol. 364, p. 65, 2011, Art no. 65, doi: 10.1557/PROC-364-65.

[66] S. Voß, M. Palm, F. Stein, and D. Raabe, "Compositional Dependence of the Compressive Yield Strength of Fe-Nb(-Al) and Co-Nb Laves Phases," *MRS Proceedings,* vol. 1295, pp. mrsf10-1295-n06-02, 2011, Art no. mrsf10-1295-n06-02, doi: 10.1557/opl.2011.459.

[67] F. Chu and D. P. Pope, "Deformation of a HF-V-NB C15 Laves Phase," *MRS Proceedings,* vol. 288, p. 561, 1992, Art no. 561, doi: 10.1557/PROC-288-561.

[68] L. Liu, P. Shen, X. Wu, R. Wang, W. Li, and Q. Liu, "First-principles calculations on the stacking fault energy, surface energy and dislocation properties of NbCr2 and HfCr2," *Computational Materials Science,* vol. 140, pp. 334-343, 2017/12/01/ 2017, doi: https://doi.org/10.1016/j.commatsci.2017.08.030.

[69] L. Ma *et al.*, "Ab initio study of stacking faults and deformation mechanism in C15 Laves phases Cr2X (X = Nb, Zr, Hf)," *Materials Chemistry and Physics,* vol. 143, no. 2, pp. 702-706, 2014/01/15/ 2014, doi: https://doi.org/10.1016/j.matchemphys.2013.09.056.

[70] A. Arora, D. B. Marshall, B. R. Lawn, and M. V. Swain, "Indentation deformation/fracture of normal and anomalous glasses," *Journal of Non-Crystalline Solids,* vol. 31, no. 3, pp. 415-428, 1979/04/01 1979, doi: http://dx.doi.org/10.1016/0022-3093(79)90154-6.

[71] K. W. Peter, "Densification and flow phenomena of glass in indentation experiments," *Journal of Non-Crystalline Solids,* vol. 5, no. 2, pp. 103-115, 1970/11/01 1970, doi: http://dx.doi.org/10.1016/0022-3093(70)90188-2.

[72] R. F. Cook and G. M. Pharr, "Direct Observation and Analysis of Indentation Cracking in Glasses and Ceramics," *Journal of the American Ceramic Society,* vol. 73, no. 4, pp. 787-817, 1990, doi: 10.1111/j.1151-2916.1990.tb05119.x.

[73] Y. Yue and R. Brückner, "A new description and interpretation of the flow behaviour of glass forming melts," *Journal of Non-Crystalline Solids,* vol. 180, no. 1, pp. 66-79, 1994/12/01 1994, doi: http://dx.doi.org/10.1016/0022-3093(94)90398-0.

[74] J. H. Simmons, R. K. Mohr, and C. J. Montrose, "Non-Newtonian viscous flow in glass," *Journal of Applied Physics,* vol. 53, no. 6, pp. 4075-4080, 1982, doi: doi:http://dx.doi.org/10.1063/1.331272.

[75] C. Zehnder, S. Bruns, J.-N. Peltzer, K. Durst, S. Korte-Kerzel, and D. Möncke, "Influence of Cooling Rate on Cracking and Plastic Deformation during Impact and Indentation of Borosilicate Glasses," (in English), *Frontiers in Materials,* Original Research vol. 4, no. 5, 2017-March-07 2017, doi: 10.3389/fmats.2017.00005.

[76] P. Malchow, K. E. Johanns, D. Möncke, S. Korte-Kerzel, L. Wondraczek, and K. Durst, "Composition and cooling-rate dependence of plastic deformation, densification, and cracking in sodium borosilicate glasses during pyramidal indentation," *Journal of Non-Crystalline Solids,* vol. 419, pp. 97-109, 7/1/ 2015, doi: http://dx.doi.org/10.1016/j.jnoncrysol.2015.03.020.

[77] S. Yoshida, J.-C. Sanglebœuf, and T. Rouxel, "Quantitative evaluation of indentation-induced densification in glass," *Journal of Materials Research,* vol. 20, no. 12, pp. 3404-3412, 2005/12/001 2005, doi: 10.1557/jmr.2005.0418.

[78] S. Korte, R. J. Stearn, J. M. Wheeler, and W. J. Clegg, "High temperature microcompression and nanoindentation in vacuum," *Journal of Materials Research,* vol. 27, no. 1, pp. 167-176, 2012/001/14 2012, doi: 10.1557/jmr.2011.268.

[79] W. D. Nix, "Mechanical properties of thin films," *MTA,* vol. 20, no. 11, p. 2217, 1989/11/01 1989, doi: 10.1007/BF02666659.

[80] W. D. Nix and H. Gao, "Indentation size effects in crystalline materials: A law for strain gradient plasticity," *Journal of the Mechanics and Physics of Solids,* vol. 46, no. 3, pp. 411-425, 1998/03/01/ 1998, doi: https://doi.org/10.1016/S0022-5096(97)00086-0.

[81] W. C. Oliver and G. M. Pharr, "An improved technique for determining hardness and elastic modulus using load and displacement sensing indentation experiments," *Journal of Materials Research,* vol. 7, no. 06, pp. 1564-1583, 1992, doi: doi:10.1557/JMR.1992.1564.

[82] W. C. Oliver and G. M. Pharr, "Measurement of hardness and elastic modulus by instrumented indentation: Advances in understanding and refinements to methodology," *Journal of Materials Research,* vol. 19, no. 01, pp. 3-20, 2004, doi: doi:10.1557/jmr.2004.19.1.3.

[83] D. Tabor, "The hardness of solids," *Review of Physics in Technology,* vol. 1, no. 3, p. 145, 1970. [Online]. Available: http://stacks.iop.org/0034-6683/1/i=3/a=I01.

[84] J. S. K. L. Gibson, S. G. Roberts, and D. E. J. Armstrong, "High temperature indentation of helium-implanted tungsten," *Materials Science and Engineering: A,* vol. 625, pp. 380-384, 2/11/ 2015, doi: http://dx.doi.org/10.1016/j.msea.2014.12.034.

[85] C. M. Byer, B. Li, B. Cao, and K. T. Ramesh, "Microcompression of single-crystal magnesium," *Scripta Materialia,* vol. 62, no. 8, pp. 536-539, 2010/04/01/ 2010, doi: https://doi.org/10.1016/j.scriptamat.2009.12.017.

[86] S. Korte, J. S. Barnard, R. J. Stearn, and W. J. Clegg, "Deformation of silicon – Insights from microcompression testing at 25–500 °C," *International Journal of Plasticity,* vol. 27, no. 11, pp. 1853-1866, 11// 2011, doi: http://dx.doi.org/10.1016/j.ijplas.2011.05.009.

[87] P. R. Howie, S. Korte, and W. J. Clegg, "Fracture modes in micropillar compression of brittle crystals," *Journal of Materials Research,* vol. 27, no. 1, pp. 141-151, 2012/001/14 2012, doi: 10.1557/jmr.2011.256.

[88] M. D. Uchic and D. M. Dimiduk, "A methodology to investigate size scale effects in crystalline plasticity using uniaxial compression testing," *Materials Science and Engineering: A,* vol. 400–401, no. 0, pp. 268-278, 7/25/ 2005, doi: http://dx.doi.org/10.1016/j.msea.2005.03.082.

[89] M. D. Uchic, D. M. Dimiduk, J. N. Florando, and W. D. Nix, "Sample Dimensions Influence Strength and Crystal Plasticity," *Science,* vol. 305, no. 5686, pp. 986-989, August 13, 2004 2004, doi: 10.1126/science.1098993.

[90] M. D. Uchic, P. A. Shade, and D. M. Dimiduk, "Plasticity of Micrometer-Scale Single Crystals in Compression," *Annual Review of Materials Research,* vol. 39, no. 1, pp. 361-386, 2009, doi: doi:10.1146/annurev-matsci-082908-145422.

[91] A. C. Fischer-Cripps, *Introduction to Contact Mechanics*, Second ed. New York: Springer Science, 2007.

[92] V. Maier, K. Durst, J. Mueller, B. Backes, H. W. Höppel, and M. Göken, "Nanoindentation strain-rate jump tests for determining the local strain-rate sensitivity in nanocrystalline Ni and ultrafine-grained Al," *Journal of Materials Research,* vol. 26, no. 11, pp. 1421-1430, 2011, doi: 10.1557/jmr.2011.156.

[93] K. Durst and V. Maier, "Dynamic nanoindentation testing for studying thermally activated processes from single to nanocrystalline metals," *Current Opinion in Solid State and Materials Science,* vol. 19, no. 6, pp. 340-353, 12// 2015, doi: http://dx.doi.org/10.1016/j.cossms.2015.02.001.

[94] H. H. Czichos, M., *Hütte - Das Ingenieurwissen*, 34 ed. Berlin: Springer-Verlag, 2012.

[95] A. A. Griffith, "The Phenomena of Rupture and Flow in Solids," *Philosophical Transactions of the Royal Society of London. Series A, Containing Papers of a Mathematical or Physical Character,* vol. 221, no. 582-593, pp. 163-198, 1921, doi: 10.1098/rsta.1921.0006.

[96] B. D. Beake, "Evaluation of the fracture resistance of DLC coatings on tool steel under dynamic loading," *Surface and Coatings Technology,* vol. 198, no. 1–3, pp. 90-93, 8/1/ 2005, doi: http://dx.doi.org/10.1016/j.surfcoat.2004.10.048.

[97] B. D. Beake, G. S. Fox-Rabinovich, S. C. Veldhuis, and S. R. Goodes, "Coating optimisation for high speed machining with advanced nanomechanical test methods," *Surface and Coatings Technology,* vol. 203, no. 13, pp. 1919-1925, 3/25/ 2009, doi: http://dx.doi.org/10.1016/j.surfcoat.2009.01.025.

[98] B. D. Beake, S. R. Goodes, and J. F. Smith, "Micro-Impact Testing: A New Technique for Investigating Thin Film Toughness, Adhesion, Erosive Wear Resistance, and Dynamic Hardness," *Surface Engineering,* vol. 17, no. 3, pp. 187-192, 2001/06/01 2001, doi: 10.1179/026708401101517755.

[99] B. D. Beake, S. R. Goodes, J. F. Smith, and F. Gao, "Nanoscale repetitive impact testing of polymer films," *Journal of Materials Research,* vol. 19, no. 1, pp. 237-247, 2004/001/001 2004, doi: 10.1557/jmr.2004.19.1.237.

[100] B. D. Beake *et al.*, "Investigating the fracture resistance and adhesion of DLC films with micro-impact testing," *Diamond and Related Materials,* vol. 11, no. 8, pp. 1606-1609, 8// 2002, doi: http://dx.doi.org/10.1016/S0925-9635(02)00107-3.

[101] B. D. Beake, S. P. Lau, and J. F. Smith, "Evaluating the fracture properties and fatigue wear of tetrahedral amorphous carbon films on silicon by nano-impact testing," *Surface and Coatings Technology,* vol. 177–178, pp. 611-615, 1/30/ 2004, doi: http://dx.doi.org/10.1016/S0257-8972(03)00934-4.

[102] B. D. Beake and N. Ranganathan, "An investigation of the nanoindentation and nano/micro-tribological behaviour of monolayer, bilayer and trilayer coatings on cemented carbide," *Materials Science and Engineering: A,* vol. 423, no. 1–2, pp. 46-51, 5/15/ 2006, doi: http://dx.doi.org/10.1016/j.msea.2005.11.066.

[103] B. D. Beake and J. F. Smith, "Nano-impact testing—an effective tool for assessing the resistance of advanced wear-resistant coatings to fatigue failure and delamination," *Surface and Coatings Technology,* vol. 188–189, pp. 594-598, 11// 2004, doi: http://dx.doi.org/10.1016/j.surfcoat.2004.07.016.

[104] M. Jennett and J. Nunn, "High resolution measurement of dynamic (nano) indentation impact energy: a step towards the determination of indentation fracture resistance," *Philosophical Magazine,* vol. 91, no. 7-9, pp. 1200-1220, 2011/03/01 2010, doi: 10.1080/14786435.2010.485585.

[105] J. R. T. C. A. Schuh, "The Hall–Petch breakdown at high strain rates: Optimizing nanocrystalline grain size for impact applications," *Applied Physics Letters,* vol. 93, no. 17, p. 171916, 2008/10/27 2008, doi: 10.1063/1.3000655.

[106] G. Skordaris *et al.*, "Brittleness and fatigue effect of mono- and multi-layer PVD films on the cutting performance of coated cemented carbide inserts," *CIRP Annals - Manufacturing Technology,* vol. 63, no. 1, pp. 93-96, // 2014, doi: http://dx.doi.org/10.1016/j.cirp.2014.03.081.

[107] H. Somekawa and C. A. Schuh, "High-strain-rate nanoindentation behavior of fine-grained magnesium alloys," *Journal of Materials Research,* vol. 27, no. 9, pp. 1295-1302, 2012/005/14 2012, doi: 10.1557/jmr.2012.52.

[108] J. M. Wheeler, C. A. Collier, J. M. Paillard, and J. A. Curran, "Evaluation of micromechanical behaviour of plasma electrolytic oxidation (PEO) coatings on Ti–6Al–4V," *Surface and Coatings Technology,* vol. 204, no. 21–22, pp. 3399-3409, 8/15/ 2010, doi: http://dx.doi.org/10.1016/j.surfcoat.2010.04.006.

[109] J. M. Wheeler and A. G. Gunner, "Analysis of failure modes under nano-impact fatigue of coatings via high-speed sampling," *Surface and Coatings Technology,* vol. 232, no. 0, pp. 264-268, 10/15/ 2013, doi: http://dx.doi.org/10.1016/j.surfcoat.2013.05.028.

[110] A. Yilmaz, "The Portevin–Le Chatelier effect: a review of experimental findings," *Science and Technology of Advanced Materials,* vol. 12, no. 6, p. 063001, 2011, doi: 10.1088/1468-6996/12/6/063001.

[111] H. Ovri and E. T. Lilleodden, "Temperature dependence of plastic instability in Al alloys: A nanoindentation study," *Materials & Design,* vol. 125, pp. 69-75, 2017/07/05/ 2017, doi: https://doi.org/10.1016/j.matdes.2017.03.071.

[112] D. L. Olmsted, L. G. Hector, and W. A. Curtin, "Molecular dynamics study of solute strengthening in Al/Mg alloys," *Journal of the Mechanics and Physics of Solids,* vol. 54, no. 8, pp. 1763-1788, 2006/08/01/ 2006, doi: https://doi.org/10.1016/j.jmps.2005.12.008.

[113] P. Hähner, "On the physics of the Portevin-Le Châtelier effect part 1: The statistics of dynamic strain ageing," *Materials Science and Engineering: A,* vol. 207, no. 2, pp. 208-215, 1996/03/30/ 1996, doi: https://doi.org/10.1016/0921-5093(95)10033-4.

[114] P. Hähner, "On the physics of the Portevin-Le Châtelier effect part 2: from microscopic to macroscopic behaviour," *Materials Science and Engineering: A,* vol. 207, no. 2, pp. 216-223, 1996/03/30/ 1996, doi: https://doi.org/10.1016/0921-5093(95)10032-6.

[115] W. A. Curtin, D. L. Olmsted, and L. G. Hector Jr, "A predictive mechanism for dynamic strain ageing in aluminium–magnesium alloys," *Nature Materials,* Article vol. 5, p. 875, 10/22/online 2006, doi: 10.1038/nmat1765.

[116] H. Aboulfadl, J. Deges, P. Choi, and D. Raabe, "Dynamic strain aging studied at the atomic scale," *Acta Materialia,* vol. 86, pp. 34-42, 2015/03/01/ 2015, doi: https://doi.org/10.1016/j.actamat.2014.12.028.

[117] F. B. Klose, J. Weidenmüller, A. Ziegenbein, P. Hähner, and H. Neuhäuser §, "Plastic instabilities with propagating deformation bands in Cu–Al alloys," *Philosophical Magazine,* vol. 84, no. 3-5, pp. 467-480, 2004/01/21 2004, doi: 10.1080/14786430310001610320.

[118] H. Neuhäuser, "Collective micro shear processes and plastic instabilities in crystalline and amorphous structures," *International Journal of Plasticity,* vol. 9, no. 4, pp. 421-435, 1993/01/01/ 1993, doi: https://doi.org/10.1016/0749-6419(93)90046-S.

[119] F. B. Klose *et al.*, "Analysis of Portevin-Le Chatelier serrations of type Bin Al–Mg," *Materials Science and Engineering: A,* vol. 369, no. 1, pp. 76-81, 2004/03/25/ 2004, doi: https://doi.org/10.1016/j.msea.2003.10.292.

[120] S. Amerioun, T. Yokosawa, S. Lidin, and U. Häussermann, "Phase Stability in the Systems AeAl2-xMgx (Ae = Ca, Sr, Ba): Electron Concentration and Size Controlled Variations on the Laves Phase Structural Theme," *Inorganic Chemistry,* vol. 43, no. 15, pp. 4751-4760, 2004/07/01 2004, doi: 10.1021/ic0400235.

Plastic deformation of single crystalline C14 Mg_2Ca Laves phase at room temperature

Christoffer Zehnder, Konrad Czerwinski, Konstantin D. Molodov, Stefanie Sandlöbes-Haut, James S.K-L. Gibson, Sandra Korte-Kerzel
Materials Science and Engineering: A, Volume 759 (2019) Pages 754-761
https://doi.org/10.1016/j.msea.2019.05.092.

Short Summary

Intermetallic phases, such as Mg2Ca, have been shown to significantly improve the creep strength of magnesium alloys. However, the relevant deformation mechanisms of the intermetallics for further alloy development are largely unknown as the application temperature of the intermetallic-metallic composites lies in their brittle low temperature regime. In this study, we investigated the deformation mechanisms of the hexagonal Mg2Ca Laves phase at the same size scale (µm) as in intermetallic-metallic alloys and at room temperature using nanomechanical test methods. We identified active slip planes by a statistical evaluation of slip traces formed around nanoindentations and measured the corresponding critical resolved shear stresses for each slip system by compression of single crystalline micropillars in selected orientations. Deformation occurs on basal, 1st and 2nd order pyramidal as well as 1st and 2nd order prismatic planes and the critical stresses are of the order of 0.44 GPa–0.59 GPa with the lowest value obtained on the 1st order prismatic planes. Finally, we discuss the possible slip systems on a theoretical basis in terms of their local atomic structure.

The authors contribution to this paper comprised conceptualization, methodology of the experimental work, investigating and analyzing the experimental data as well as writing the paper.

Materials Science & Engineering A 759 (2019) 754–761

Contents lists available at ScienceDirect

Materials Science & Engineering A

journal homepage: www.elsevier.com/locate/msea

Plastic deformation of single crystalline C14 Mg_2Ca Laves phase at room temperature

Christoffer Zehnder, Konrad Czerwinski, Konstantin D. Molodov, Stefanie Sandlöbes-Haut, James S.K-L. Gibson, Sandra Korte-Kerzel*

Institut für Metallkunde und Materialphysik, RWTH Aachen University, Aachen, Germany

ARTICLE INFO

Keywords:
Dislocation
Crystal plasticity
Mechanical testing
Ductility
Intermetallics

ABSTRACT

Intermetallic phases, such as Mg_2Ca, have been shown to significantly improve the creep strength of magnesium alloys. However, the relevant deformation mechanisms of the intermetallics for further alloy development are largely unknown as the application temperature of the intermetallic-metallic composites lies in their brittle low temperature regime. In this study, we investigated the deformation mechanisms of the hexagonal Mg_2Ca Laves phase at the same size scale (μm) as in intermetallic-metallic alloys and at room temperature using nano-mechanical test methods. We identified active slip planes by a statistical evaluation of slip traces formed around nanoindentations and measured the corresponding critical resolved shear stresses for each slip system by compression of single crystalline micropillars in selected orientations. Deformation occurs on basal, 1^{st} and 2^{nd} order pyramidal as well as 1^{st} and 2^{nd} order prismatic planes and the critical stresses are of the order of 0.44 GPa–0.59 GPa with the lowest value obtained on the 1^{st} order prismatic planes. Finally, we discuss the possible slip systems on a theoretical basis in terms of their local atomic structure.

1. Introduction

1.1. Laves phases in the Mg–Al–Ca system

Although Laves phases are brittle and thus offer limited use as structural materials on their own, they can be used to stabilise weaker metallic matrices [1]. For example, if Al and Ca are added to Mg-alloys, the creep resistance increases by up to three orders of magnitude [2–11]. This improved creep resistance is attributed to the precipitation of intermetallic phases inside the grains and at the grain boundaries. Amberger et al. [12,13] have shown that an interconnected intermetallic skeleton significantly hinders grain boundary sliding and reduces the stress in the matrix.

Depending on chemical composition and heat treatment, the intermetallic skeleton consists of a mixture of different intermetallic phases: the $Mg_{17}Al_{12}$ phase with the A12 structure and several Laves phases: the hexagonal C14 Mg_2Ca and C36 $(Mg,Al)_2Ca$ as well as the cubic C15 Al_2Ca structure [3,14–16]. Investigations on the $Mg_{17}Al_{12}$ phase [17,18] have revealed a pronounced drop in hardness at temperatures exceeding 150 °C. As the application temperature of cast magnesium alloys can exceed 150 °C, replacing $Mg_{17}Al_{12}$ with Laves phases - if they are stable and retain strength up to higher temperatures - would further increase the application temperature. The mechanical behaviour of Laves phases at temperatures significantly above 150 °C, i.e. above the macroscopically observed brittle-to-ductile transition temperature has already been investigated [19,20]. However, in order to guide a knowledge-based alloy design, understanding of low temperature properties and in particular whether and how these intermetallics may also exhibit low temperature plastic deformation at the micrometre scale encountered in reinforced alloys is also required. Unfortunately, so far, there is very little known about the room temperature deformation behaviour of Laves phases [21] but deformation experiments at the nano- and microscale have revealed significant plasticity at small scales in similar phases [22–24] due to a size effect on fracture favouring plasticity in small volumes [25].

1.2. The deformation mechanisms of Laves phases

Without extensive literature available on low temperature deformation of Laves phases, their comprehensively investigated high temperature, bulk deformation mechanisms are a natural starting point also for work at room temperature: Paufler et al. have investigated the mechanical properties of single-crystalline Laves phases at homologous temperatures (i.e. the absolute temperature divided by the melting

* Corresponding author.
E-mail address: korte-kerzel@imm.rwth-aachen.de (S. Korte-Kerzel).

https://doi.org/10.1016/j.msea.2019.05.092
Received 22 January 2019; Received in revised form 22 May 2019; Accepted 23 May 2019
Available online 24 May 2019
0921-5093/

point) of greater than 0.6 [19,20,26–31], the high temperature range in which Laves phases typically exceed their brittle-to-ductile-transition temperature [32]. The theoretical investigation on possible slip systems in the hexagonal C14 phase by Krämer et al. has revealed slip systems typically observed in hexagonal metals, i.e. basal, prismatic, and 1st and 2nd order pyramidal [33]. Their further experimental work on the hexagonal Mg_2Zn Laves phase confirmed these results and led to the conclusion that deformation at high temperatures is controlled by the Peierls barrier, i.e. the intrinsic resistance of the lattice to dislocation motion [26–28]. As dislocation motion against this resistance is known to be strongly thermally activated [34], the resulting critical resolved shear stresses may be much higher at low temperatures. Macroscopic samples therefore show no significant plastic regime at room temperature but fail by rapid brittle fracture [21,35], making it impossible to investigate the mechanisms of plastic deformation at these temperatures by conventional macroscopic mechanical testing.

One way to overcome this brittle behaviour is to test samples in compression at much smaller scales, such that the existence of critical pre-existing cracks becomes unlikely and their nucleation and growth is impeded by the small elastically strained volume and, where possible, also the choice of slip geometry. In the latter case, the choice of single slip conditions prevents slip band intersections leading to crack nucleation. Nevertheless, there is only limited literature data concerning deformation of Laves phases by nanomechanical testing techniques at low homologous temperatures. Takata et al. have used micropillar compression to deform C14 Fe_2Nb samples at room temperature and found the basal and 2nd order pyramidal planes being activated [22,36]. Korte et al. have investigated the cubic C15 Laves phase Nb_2Co showing dislocation slip on the {111} planes [24].

A different approach is to deform alloys where Laves phases precipitate in large areas and thus participate in the deformation. In this way, Liu et al. have shown the occurrence of non-basal slip on the $\{10\bar{1}0\}$, $\{10\bar{1}1\}$ and $\{10\bar{1}2\}$ planes in the C36 phases Ni_2Mg and Fe_2Cr after macroscopic compression experiments on Ni15%-Mg and Fe10%-Zr alloys at room temperature [37,38].

1.3. Theoretical evaluation of different slip systems in Laves phases

Previous studies, especially the ones conducted at high temperature, mainly investigated the occurrence of basal slip, where synchroshear can take place to allow dislocation motion in the densely-packed triple layer. Kronenberg first proposed this coupled movement of partial dislocations on different crystallographic planes as a plastic deformation mechanism in sapphire [39]. As the mechanism describes the synchronised movement of partial dislocations, it was named synchroshear. Hazzledine et al. [40] suggested that it might also operate in the basal plane of Laves phases and an atomic arrangement consistent with synchroshear was observed in a Laves phase imaged by Chisholm et al. by high resolution scanning transmission electron microscopy [41]. Beyond this, it should be noted that the operation of synchroshear as a mechanism of plastic deformation in Laves phases has mainly been assumed so far rather than directly confirmed by high resolution analysis of mobile defects [21,42–44].

Beyond the triple layer of the basal plane in hexagonal or {111} planes in cubic Laves phases, it has been shown [22,37,38,43] that other slip systems can be activated in addition, even at room temperature. Krämer and Schulz have conducted an extensive theoretical study to investigate how favourable the activation of different slip systems is [33]. For this purpose, they have defined different parameters that may influence the stress required for dislocation motion on a given plane, such as out-of-plane displacement of the moving atoms, coordination number and atomic smoothness of the glide plane [33]. They [33] concluded that the slip systems given in Table 1 (translated from the original paper) would be energetically possible from a theoretical point of view. Although Burgers vectors have not been analysed in this work, slip is assumed to take place in the directions given in Table 1.

Table 1
Possible slip systems in the hexagonal C14 Laves phase from a theoretical point of view, from Ref. [33].

Slip System	Plane	Burgers vector	Type of dislocation
Basal	{0001}	$\frac{1}{3}<11\bar{2}0>$	Perfect
Basal (Synchroshear)	{0001}	$\frac{1}{3}<10\bar{1}0>$	Partial
1st order Prismatic	$\{10\bar{1}0\}$	$\frac{1}{3}<\bar{1}2\bar{1}0>$	Perfect
		<0001>	Perfect
		$\frac{1}{2}<0001>$	Partial
2nd order Prismatic	$\{11\bar{2}0\}$	$<1\bar{1}00>$	Perfect
1st order Pyramidal	$\{\bar{1}101\}$	$\frac{1}{3}<1\bar{1}00>$	Partial
		$\frac{1}{3}<\bar{1}2\bar{1}0>$	Perfect
		$\frac{1}{3}<\bar{2}113>$	Perfect
2nd order Pyramidal	$\{11\bar{2}2\}$	$\frac{1}{3}<\bar{1}\bar{1}23>$	Perfect

Here, we investigated in detail the activation of different slip systems of the C14 Mg_2Ca Laves phase at room temperature. To this end, we used nanoindentation into individual grains in correlation with crystal orientations from electron backscatter diffraction (EBSD) to obtain statistically-meaningful information on the frequency of slip plane activation. These results were confirmed and explored in more detail by means of transmission electron microscopy. Finally, the identified slip planes were studied quantitatively in terms of their specific critical resolved shear stresses by compression of single crystalline micropillars [24,45,46].

2. Experimental

2.1. Sample preparation

Samples of C14 $Mg_{70}Ca_{30}$ Laves phase were polished with diamond paste to 0.25 µm, followed by a final polishing step with 0.05 µm aluminium oxide polishing solution (OPA). The grain size varied between 20 µm and 100 µm. The composition was confirmed by energy-dispersive X-ray spectroscopy (EDAX (NJ, USA)/FEI Helios Nanolab 600i).

2.2. Nanoindentation experiments and slip line analysis

Nanoindentation experiments within single grains were conducted with a diamond Berkovich tip to 100 mN under a constant loading rate of 2 mN/s, with each grain containing between five and seven indents. The data was analysed using the method described by Oliver and Pharr and a Young's modulus of 1141 GPa and a Poisson ratio of 0.07 for diamond [47] as well as a Poisson ratio of 0.24 for Mg_2Ca using here an intermediate value of those between 0.20 and 0.27 given in Refs. [48–50]. The distance between two indents and between an indent and a grain boundary was controlled to be larger than 10 µm. After indentation, small slip lines were measured around the indent by scanning electron microscopy (SEM) (FEI Helios Nanolab 600i) and atomic force microscopy (AFM) (Park Systems, XE-70, analysis with WSxM-5 [51]) (Fig. 1). These lines correspond to the intersections between the operating slip plane and the surface of the sample. Subsequently, EBSD maps around the indents were recorded (Hicari, EDAX (NJ, USA)). The angles of the slip traces were measured in the secondary electron (SE) images and compared with the geometrical values calculated from EBSD data for each slip plane given in Table 1. In this way, surface slip lines were correlated to slip planes (Fig. 1). This analysis is necessarily statistical in nature, as it is possible that several slip planes may intersect the surface at the same angle and the solution is therefore not always unambiguous. In total, 345 slip traces have been analysed around 33 indents with 15% of these resulting in two possible solutions

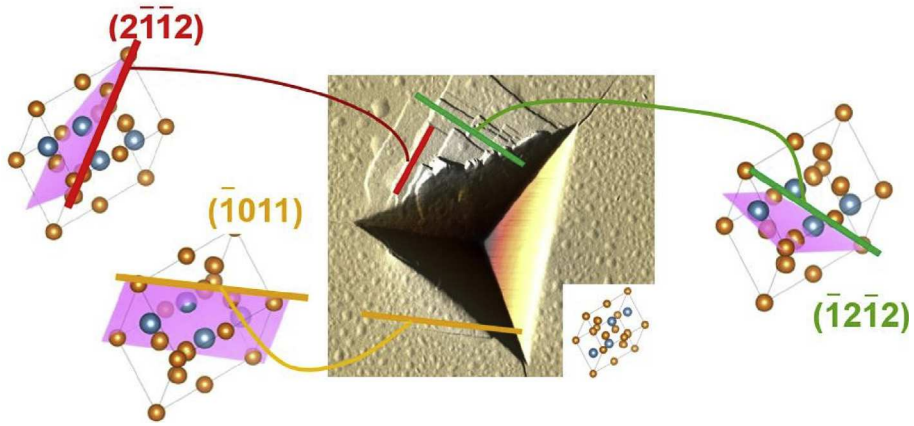

Fig. 1. AFM image of a nanoindent with slip traces surrounding the indent. The angles of the slip traces were measured and compared to the traces of different slip planes using the crystal orientation obtained from EBSD.

and another 15% that could not be correlated within a maximum deviation of 6° from the available theoretical solutions. The value of 6° was chosen to balance the occurrence of ambiguous and zero solutions in the analysis as proposed in a similar analysis by Schröders et al. [52].

2.3. Micropillar compression experiments

25 micropillars were milled in individual grains with orientations of the grains chosen such that most c-axis orientations between 0° and 90° were covered. Pillars were milled with a height of 6 µm and a diameter of 2 µm using a focused ion beam (FIB) (FEI Helios Nanolab 600i). The pillars were cut with concentric circles with decreasing currents from 21 nA to 80 pA at 30 kV to minimise beam damage and obtain a small taper angle of the pillars. Cylindrical pillars were chosen to reduce the influence of FIB damage [53] as well as to prevent potential incompatibilities formed by deforming a hexagonal crystal in a square pillar [54]. The pillars were then compressed using a 10 µm diamond flat punch with a loading rate of 0.2 mN/s using a NanoTest Platform III (Micro Materials Limited, Wrexham, UK). The displacement data were corrected using a correction for elastic sink-in Ref. [55] with a Young's modulus of 1141 GPa and 53 GPa and a Poisson ratio of 0.07 and 0.24 for diamond and for Mg_2Ca, respectively [47–50]. Both the slip direction and the angle(s) of the activated slip plane(s) on the surface of deformed micropillars were measured and correlated to possible slip planes within the hexagonal crystal structure (Fig. 2). The maximum allowed deviation between the angle measured in the SE image and the possible angle of the slip planes from EBSD was taken as 6°. The upper diameter of the pillar was used for the calculation of critical resolved shear stresses (CRSS) needed to activate a slip system as slip appeared to nucleate predominantly near the top.

2.4. TEM

TEM lamellae were prepared as cross-sections from indents and compressed micropillars using FIB milling (FEI Helios Nanolab 600i) to validate the glide planes determined in micropillar compression and indentation. A final thinning current of 80 pA at 30 kV accelerating voltage was applied during preparation. The samples were analysed by conventional transmission electron microscopy (TEM) (Philips CM20) operated at an accelerating voltage of 200 kV.

3. Results

3.1. Nanoindentation and micropillar compression experiments

The average hardness at 500 nm indentation depth and modulus for all grains tested was determined to be 3.42 ± 0.22 GPa and 55.1 ± 3.0 GPa, respectively. The Young's modulus is in good agreement with first-principle investigations giving values between 45.98 GPa and 55.74 GPa [56].

In order to test individual crystallographic orientations by single-grain indents, the angle between the c-axis and the surface normal was divided into 15° steps, and for each between five and seven indents were analysed in terms of the active slip planes. For every division, the number of slip traces corresponding to each slip system was determined. Their absolute numbers and fractions by slip plane over all orientations is summarised in Table 2. Basal and 1st order pyramidal slip are the least and most frequently activated slip planes at 6.0% and 34.3%, respectively.

This approach intrinsically assumes dislocation activity is equally divided across the activated slip planes, i.e. it does not account for differences in slip step height. Additionally, as sub-surface dislocation motion cannot be accounted for in this method, it necessarily assumes that all slip systems are equal with respect to their ability to produce a slip step and that differences for a given indent in a specific crystal orientation are therefore only caused by the unit cell symmetry and the crystal orientation with respect to the induced stress field and surface. However, as only slip resulting in appreciable surface topology becomes sufficiently visible in the experiments, the pool of theoretically possible slip planes that would provide a match for a given slip trace was reduced to those enclosing at least a 10° angle with the surface. This excludes very shallow planes that would require a large number of dislocations to travel a long way from the highly stressed zone to produce a slip step of appreciable height.

With respect to the measurements of the slip step height, these could in theory be correlated to a number of dislocations on a slip system to increase the accuracy of this approach. However, these measurements - if made by AFM - would be extremely time consuming. This therefore contradicts the intention of these measurements: to rapidly and straightforwardly obtain statistically-meaningful information on the activation of different slip planes. In addition, AFM measurements would need to be conducted before the EBSD maps can be collected due to typical contamination of the sample with carbon during electron imaging. This further increases experimental time as many more indents are required to ensure sufficient data are present over the distribution of orientations. Whether other high-resolution measurements, such as laser beam interferometry, would enable the necessary rapid, high resolution (and ideally automated) analysis remains to be seen. In spite of these limitations of surface observation by electron microscopy, the approach is exceedingly useful in guiding the subsequent uniaxial experiments in terms of the crystal orientations that are most interesting to investigate in more detail.

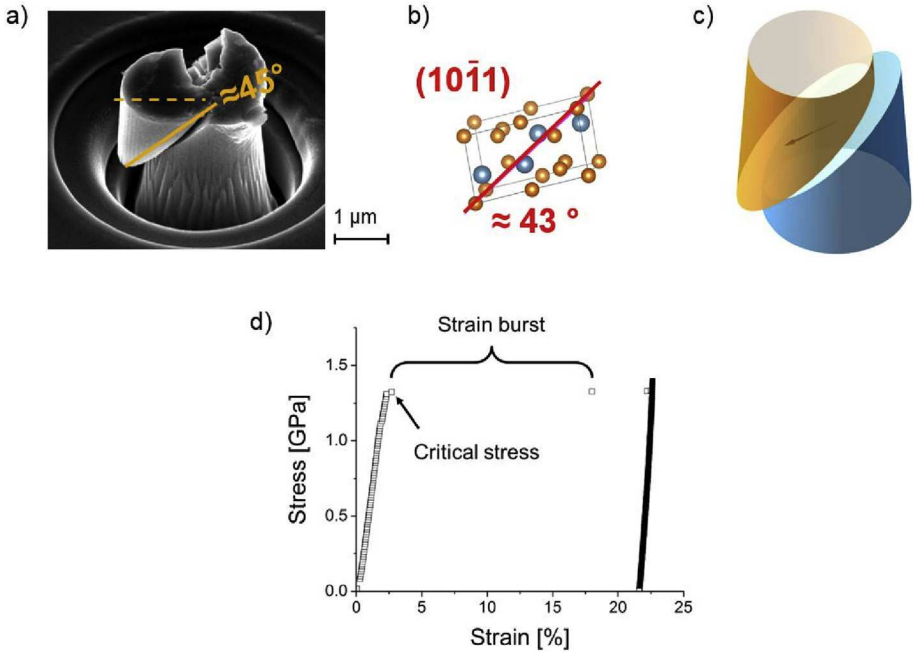

Fig. 2. (a) A compressed micropillar with one dominant slip event and (b) the corresponding crystal orientation derived from EBSD with the identified slip plane shown schematically. Using the geometrically-possible slip direction with the highest Schmid factor, the expected slip geometry of a micropillar with the same orientation is illustrated in (c), viewed in the same direction as the SE image of the real micropillar in (a). A typical stress-strain curve from a compression test (d) exhibits no work hardening but a clear transition from ideally-elastic to plastic deformation. The stress at which the strain burst appears was taken to determine the CRSS.

Micropillar compression revealed 1st order pyramidal and 2nd order pyramidal slip in 4 and 12 pillars, respectively, out of 25 micropillars in total spanning the complete range of angles α between the c-axis and the compression direction. Prismatic slip was mainly observed at intermediate and high angles in the regime α = 30°–90°, where α is the angle between the c-axis and the surface normal, i.e. the indentation or compression direction. Basal slip was only found at an angle of α = 44°. 2nd order prismatic slip was not observed at all.

Table 2 lists the measured CRSS for slip on basal, prismatic and both pyramidal slip planes. For calculating the CRSS values, the slip plane was determined from the angle of the observed slip trace on the micropillar. In this slip plane, the slip direction exhibiting the maximum Schmid factor was selected and verified for consistency with the slip direction observed in the SEM, as was shown in Fig. 2. For basal, prismatic and 1st order pyramidal slip, < a > dislocations were considered, whereas < c+a > type dislocations were considered for 2nd order pyramidal slip. For all pillars which were indexed as slipped on a 1st order pyramidal plane in this study, always an < a > Burgers vector exhibited a high Schmid factor, so that we assume here this shorter Burgers vector to operate in all pillars found to slip on this plane. In terms of the derived CRSS values, 1st order prismatic slip shows the lowest CRSS with 0.44 GPa, followed by 1st order pyramidal and basal slip with 0.53 GPa and 0.52 GPa, respectively. 2nd order pyramidal slip shows the highest values of 0.59 GPa.

3.2. TEM investigations

TEM was conducted to validate the glide planes determined from surface trace analysis of deformed micropillars and around indents. Fig. 3a shows an indent exhibiting slip lines which correlate to all three prismatic slip planes. A TEM lamella was cut from this indent in the direction indicated by the black rectangle. Fig. 3 b shows a TEM micrograph and corresponding selected area electron diffraction (SAED) pattern of this lamella, confirming the presence of all three prismatic slip planes. The same confirmation of the SEM slip trace analysis was found in micropillars.

The dislocation density within the indent and micropillars was, however, too high to conduct a Burgers vector analysis. Therefore, smaller indents were made with a maximum depth of only 500 nm and in two crystal orientations, to identify which dislocations are present as a result of low-temperature deformation in Laves phases. Indents are useful in this regard, as many more slip planes are activated simultaneously. From these, TEM lamellae were cut to study the presence of the two possible types of dislocations on the 1st order pyramidal planes, namely < a > or < c+a > dislocations. Even though the indentation depth was reduced, the dislocation density in the glide bands was still relatively high, preventing identification of individual dislocations for Burgers vector analysis using the $\vec{g}\cdot\vec{b}$ ($\vec{g}$: diffraction vector; $\vec{b}$: Burgers vector) invisibility analysis.

For an indent in Fig. 4, an estimate of possible Burgers vectors due to different numbers of (in)visible dislocations in different two-beam conditions was possible. The lamella contained visible dislocations

Table 2
Results of the geometrical and experimental slip trace analysis with the occurrence of slip planes in the experiment, Ω_{exp}, the geometrical prediction of each plane's occurrence, Ω_{theo}., and the resulting deviation, Δ, with the measurement of critical resolved shear stresses (CRSS) by microcompression.

	Slip plane	Basal {0001}	1st order prismatic {10$\bar{1}$0}	2nd order prismatic {11$\bar{2}$0}	1st order pyramidal {11$\bar{1}$1}	2nd order pyramidal {11$\bar{2}$2}
Nanoindentation	Number of traces	22	92	45	131	92
	Ω_{exp} [%]	6.0	23.8	11.6	34.3	24.4
	Ω_{theo} [%]	4.8	16.8	16.3	32.9	29.3
	$\Delta = \Omega_{exp} - \Omega_{theo}$ [%]	1.2	7.0	−4.7	1.4	−4.9
µ-compression	Number of pillars	6	2	0	4	12
	Slip direction	< a >	< a >	< a >	< a >	< c+a >
	CRSS [GPa]	0.52 ± 0.05	0.44 ± 0.01	–	0.53 ± 0.07	0.59 ± 0.07

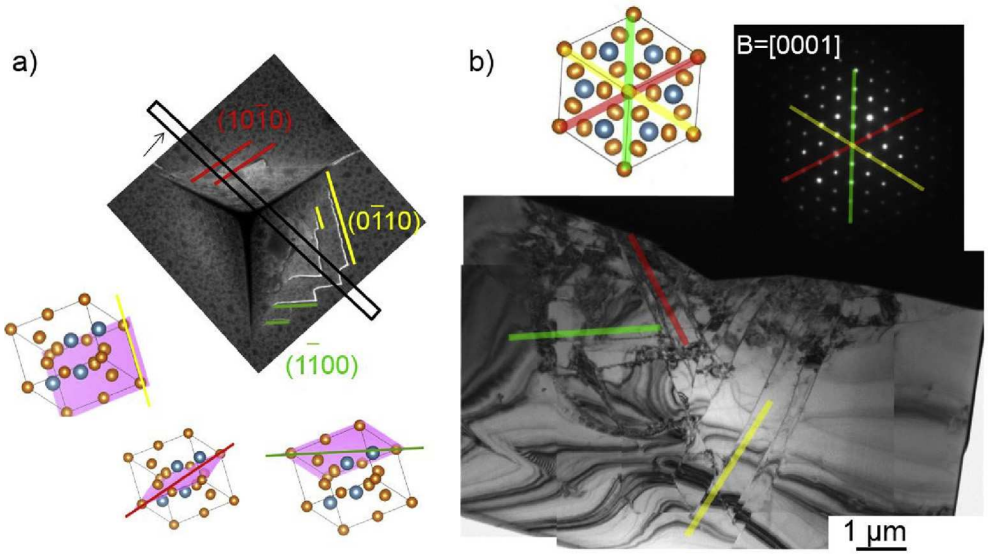

Fig. 3. Verification of slip plane identification obtained from surface slip traces, (a) indent with slip trace analysis suggesting prismatic slip. The surface normal is (4$\bar{1}$56). (b) TEM bright field (BF) image and selected area electron diffraction (SAED) pattern of a lamella prepared from the indent shown in (a) as indicated by the black rectangle.

using the diffraction vectors (0$\bar{1}$11), (10$\bar{1}$0), ($\bar{2}$110) and ($\bar{2}$112). For $\vec{g}$ = (0002), the dislocations are not visible. This combination can only be fulfilled by the < a > partial dislocations $\frac{1}{3}$ [10$\bar{1}$0] and $\frac{1}{3}$ [01$\bar{1}$0].

For the indent shown in Fig. 5, it was not possible to unambiguously determine the visibility of dislocations for all diffraction vectors. However, visibility under the diffraction vector $\vec{g}$ = (0002) reveals the presence of (partial) dislocations with a < c > component, presumably of < c + a > type.

4. Discussion

4.1. Relation of slip trace frequency, crystal structure and CRSS

Previous fundamental studies of Laves phases have shown that basal, 1st and 2nd order pyramidal as well as 1st order prismatic slip can be activated in Laves phases at room temperature [21,37,38,41,43]. However, the relative frequency of basal vs. non-basal slip, and the corresponding specific CRSS values have not been investigated, mainly due to the lack of single crystal experiments at room temperature. Only the micro-mechanical investigations of C14 Fe_2Nb by Takata [22,36] showed basal and 2nd order pyramidal slip in single crystal compression experiments, which were also confirmed in this study. The higher CRSS values for these slip systems determined by Takata are attributed to the stronger bonding in an Fe–Ni–Nb system with a theoretical shear modulus from density functional theory nearly five times that of Mg_2Ca [48,57] and an experimental nanoindentation hardness approximately four times higher than measured here [58]. Nevertheless, it can be seen that similar slip systems are active in these structurally similar materials.

In the present study, the relative frequency of basal and non-basal slip planes was determined and the corresponding CRSS values on the operating slip systems were measured. In this data, a discrepancy is suspected at first glance: 2nd order pyramidal and 1st order prismatic slip both show an activation frequency of 24% in nanoindentation but

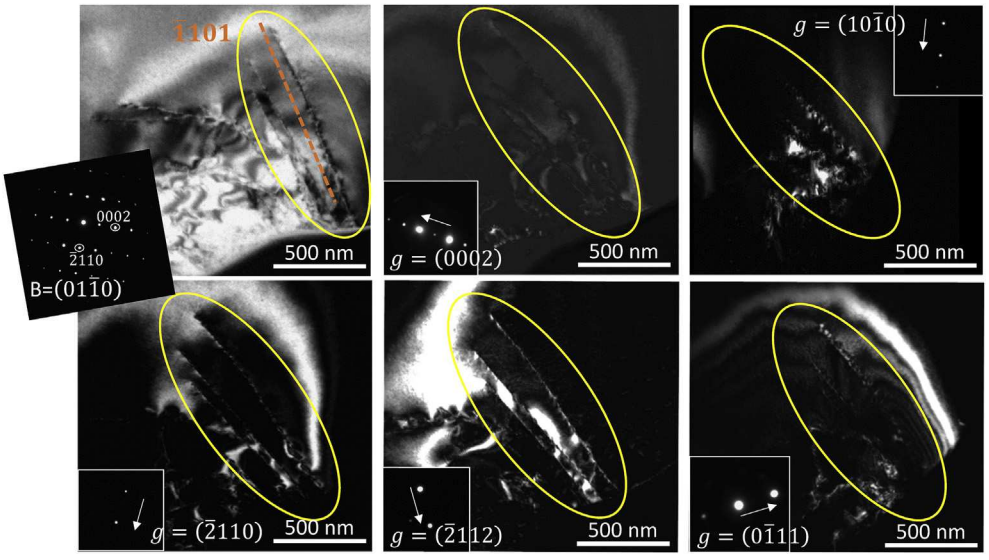

Fig. 4. Indent revealing the presence of $\frac{1}{3}$ [10$\bar{1}$0] and/or $\frac{1}{3}$ [01$\bar{1}$0] < a > -type partial dislocations. The yellow circle marks the region where the dislocations are (in) visible under different diffraction vectors (g). Indexing of slip planes was done using the ($B = 1\bar{2}1\bar{3}$) zone axis. (For interpretation of the references to colour in this figure legend, the reader is referred to the Web version of this article.)

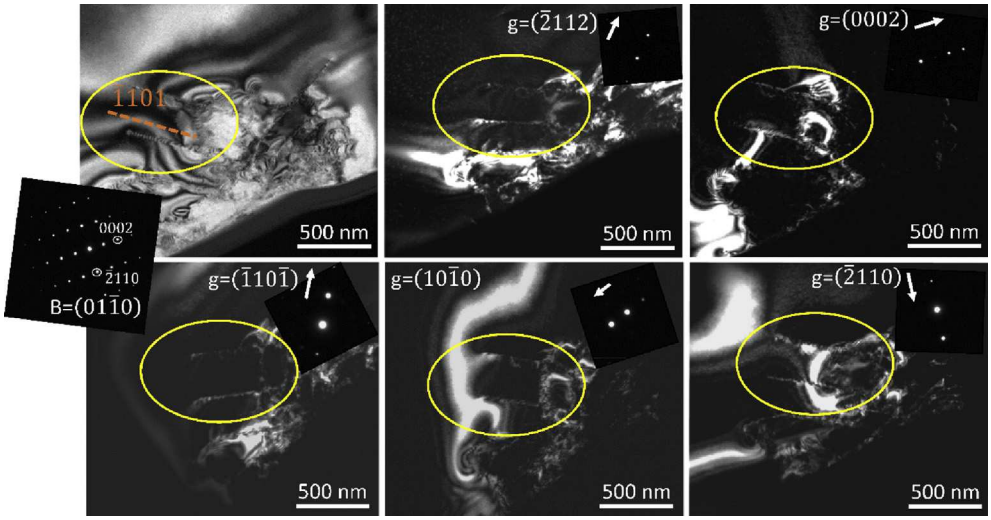

Fig. 5. Indent with a high dislocation density including those with a < c > component. The yellow circle marks the region where the dislocations are (in)visible under different diffraction vectors (g). Indexing of slip planes was done using the $B = (1\bar{2}1\bar{3})$ zone axis. (For interpretation of the references to colour in this figure legend, the reader is referred to the Web version of this article.)

exhibit completely different CRSS values: 0.59 GPa and 0.44 GPa, respectively. On the other hand, basal and 1st order pyramidal slip exhibit both a CRSS value of ~0.52 GPa but a very different activation frequency of 6% and 34%, respectively.

This apparent discrepancy is removed by considering the anisotropy of the hexagonal crystal structure. As different slip systems exhibit different numbers of equivalent slip planes in a hexagonal crystal, the number of intersections of the equivalent planes of one system with the sample surface is also different. For example, hexagonal crystals have three crystallographically equivalent prismatic slip planes at different angles in the unit cell, but only one basal plane. The frequency at which any given plane is activated is therefore a function of the crystal symmetry but also the texture of the sample and the probability of a given slip plane to cause a surface trace depending on its angle of intersection with the surface. To quantify the theoretical number of plane-surface intersections for the specific grains investigated here by nanoindentation slip trace analysis, Matlab was used to simulate 1,000,000 randomly chosen lines on the surface of a material with identical texture as the experimentally indented material [52]. These randomly distributed lines were assigned to crystallographic planes in the same way as described above for the experimentally measured surface steps. Equivalent to the experimental analysis, all cases where the angle between the slip plane and the surface was shallow (smaller than 10°) were excluded from this analysis. The results from this analysis then revealed the expected relative occurrence of different slip planes Ω_{theo} [%] considering crystal symmetry and texture under the assumption that all slip systems on the considered slip planes exhibit exactly the same CRSS value. The difference between the expected frequency of activation of each set of planes and the experimentally measured results, Δ, correspond to their differences in CRSS.

Comparison of the experimental data obtained from the analysis of surface steps formed during nanoindentation with this geometrical analysis is in very good agreement with the CRSS values determined in micropillar compression (Table 2): Basal and 1st order pyramidal slip show almost the same relative activation as predicted by the geometrical analysis and indeed exhibit a similar CRSS. 1st order prismatic slip shows a higher frequency relative to the expected value and, correspondingly, a lower CRSS. On the other hand, 2nd order pyramidal slip was observed less often than predicted and shows a higher CRSS than basal and 1st order pyramidal slip. As the Schmid factors for 2nd order prismatic slip in the compressed micropillars covered the range from 0.40 to 0.49, but it was not found to operate in any of the pillars tested, it is assumed that 2nd order prismatic slip also has a high CRSS and is difficult to activate in the C14 Laves phase, consistent with the scarcity of 2nd order prismatic slip traces during the nanoindentation experiments.

The CRSS values for basal and 1st order pyramidal slip determined using micropillar compression are very similar. A possible reason for this is given in Fig. 6: the 1st order pyramidal plane (b) contains a triple layer similar, but not identical to, that in the basal plane (a) where the synchroshear mechanism is thought to operate. The black lines in Fig. 6 highlight the atoms that are involved in the synchroshear mechanism on the basal plane and exhibit a similar configuration on the 1st order pyramidal plane. Therefore, a mechanism similar to the synchroshear mechanism in the basal plane could operate in the 1st order pyramidal plane, although this will need to be confirmed given the opposing stacking elements within the triple layer and the reduced planarity of the pyramidal plane.

Micro-mechanical data is typically difficult to extend to macroscopic scales due to size effects on the measured stresses [59,60]. These

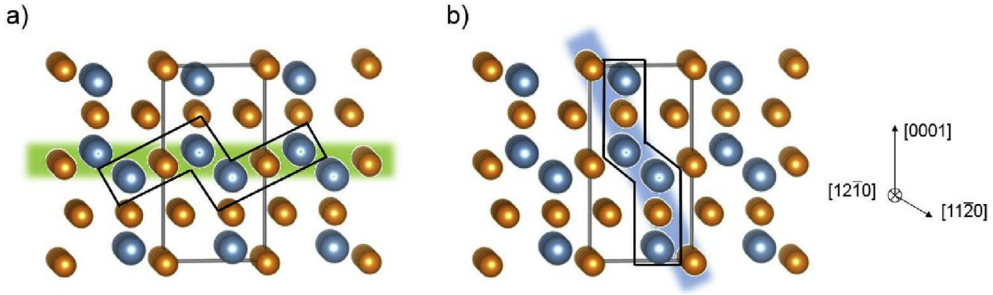

Fig. 6. Basal (a) and 1st order pyramidal (b) slip plane. The triple layer is marked in green and blue, respectively, and the black lines mark the atoms that are involved in the synchroshear mechanism on the basal plane (a) and may be involved in a similar non-planar mechanism on the pyramidal plane (b). (For interpretation of the references to colour in this figure legend, the reader is referred to the Web version of this article.)

are known to be much less severe in relative magnitude where the basic strength of the material is high and source-controlled mechanisms affected strongly by sample size are not very dominant [23,61]. However, in the case of the Laves phases studied here a translation into macroscopic properties is neither necessary nor intended as their application lies in reinforcement by means of a fully-connected intermetallic skeleton with strut sizes of the same order of a micrometre as used in the samples tested in this study. The determined values of hardness and CRSS are therefore directly relevant without any extrapolation towards the (currently unknown) bulk behaviour. These CRSS values are therefore suitable for any future crystal plasticity modelling of both the C14 Mg_2Ca phase as well as the overall behaviour of the creep-resistant intermetallic-metallic composite Mg alloy, even if hardening behaviour or rate/temperature dependence remain to be explored.

5. Conclusions

We investigated the plastic deformation behaviour of the hexagonal C14 Mg_2Ca Laves phase at room temperature. The combination of nanoindentation slip trace analysis and microcompression in conjunction with EBSD, AFM and TEM proved efficient and successful in determining the active slip systems and the respective critical resolved shear stress of this brittle and anisotropic phase.

- Statistical analysis of 345 surface slip traces formed around nanoindentations suggested a scaling of the critical resolved shear stresses as follows: 1^{st} order prismatic < basal ≈ 1^{st} order pyramidal < 2^{nd} order pyramidal slip ≤ 2^{nd} order prismatic.
- Micropillar compression experiments confirmed and quantified these results as $\tau_{1^{st}prismatic} = 0.44\ \text{Gpa} < \tau_{\text{basal}} = 0.52\ \text{GPa} \approx \tau_{1^{st}\text{pyramidal}} = 0.53\ \text{Gpa} < \tau_{2^{nd}\text{pyramidal}} = 0.59\ \text{GPa} \leq \tau_{2^{nd}\text{prismatic}}$
- TEM analysis of dislocations on 1^{st} order pyramidal planes revealed the presence of both < a > and < c + a > type (partial) dislocations.

Funding

This research did not receive any specific grant from funding agencies in the public, commercial, or not-for-profit sector but benefitted directly from work performed in project KO4603/2-1 funded by the German Research Foundation (DFG).

Data availability statement

The raw/processed data required to reproduce these findings cannot be shared at this time as the data also forms part of an ongoing study.

Acknowledgements

The authors would like to thank M. Loeck (IMM, RWTH Aachen) for help with Matlab.

References

[1] G. Sauthoff, Laves Phases, Intermetallics, Wiley-VCH Verlag GmbH, 1995, pp. 100–106.
[2] Y. Terada, R. Sota, N. Ishimatsu, T. Sato, K. Ohori, A thousandfold creep strengthening by Ca addition in die-cast AM50 magnesium alloy, Metall. Mater. Trans. A 35 (9) (2004) 3029–3032.
[3] T. Rzychoń, Characterization of Mg-rich clusters in the C36 phase of the Mg–5Al–3Ca–0.7Sr–0.2Mn alloy, J. Alloy. Comp. 598 (0) (2014) 95–105.
[4] W. Qudong, C. Wenzhou, Z. Xiaoqin, L. Yizhen, D. Wenjiang, Z. Yanping, X. Xiaoping, M. Mabuchi, Effects of Ca addition on the microstructure and mechanical properties of AZ91magnesium alloy, J. Mater. Sci. 36 (12) (2001) 3035–3040.
[5] A. Luo, B.R. Powell, M. Balogh, Creep and microstructure of magnesium-aluminum-calcium based alloys, Metall. Mater. Trans. A 33 (3) (2002) 567–574.
[6] A. Luo, Recent magnesium alloy development for automotive powertrain applications, Mater. Sci. Forum 419–422 (2003) 57–66.
[7] H. Cao, C. Zhang, J. Zhu, G. Cao, S. Kou, R. Schmid-Fetzer, Y.A. Chang, Experiments coupled with modeling to establish the Mg-rich phase equilibria of Mg–Al–Ca, Acta Mater. 56 (18) (2008) 5245–5254.
[8] T. Sato, M.V. Kral, Microstructural evolution of Mg–Al–Ca–Sr alloy during creep, Mater. Sci. Eng., A 498 (1–2) (2008) 369–376.
[9] M. Vogel, O. Kraft, E. Arzt, Creep behavior of magnesium die-cast alloy ZA85, Scripta Mater. 48 (8) (2003) 985–990.
[10] B. Backes, K. Durst, D. Amberger, M. Göken, Particle hardening in creep-resistant Mg-alloy MRI 230D probed by nanoindenting atomic force microscopy, Metall. Mater. Trans. A 40 (2) (2009) 257–261.
[11] N.D. Saddock, A. Suzuki, J.W. Jones, T.M. Pollock, Grain-scale creep processes in Mg–Al–Ca base alloys: implications for alloy design, Scripta Mater. 63 (7) (2010) 692–697.
[12] D. Amberger, P. Eisenlohr, M. Göken, Microstructural evolution during creep of Ca-containing AZ91, Mater. Sci. Eng.: A 510–511 (0) (2009) 398–402.
[13] D. Amberger, P. Eisenlohr, M. Göken, On the importance of a connected hard-phase skeleton for the creep resistance of Mg alloys, Acta Mater. 60 (5) (2012) 2277–2289.
[14] H. Zhang, S.-L. Shang, Y. Wang, L.-Q. Chen, Z.-K. Liu, Thermodynamic properties of Laves phases in the Mg–Al–Ca system at finite temperature from first-principles, Intermetallics 22 (0) (2012) 17–23.
[15] M.P. Liu, Q.D. Wang, X.Q. Zeng, G.Y. Yuan, Y.P. Zhu, W.J. Ding, Mechanical properties and creep behavior of Mg–Al–Ca alloys, Mater. Sci. Forum 488 (2005) 763–766.
[16] R. Ninomiya, T. Ojiro, K. Kubota, Improved heat resistance of Mg-Al alloys by the Ca addition, Acta Metall. Mater. 43 (2) (1995) 669–674.
[17] H.N. Mathur, V. Maier-Kiener, S. Korte-Kerzel, Deformation in the γ-$Mg_{17}Al_{12}$ phase at 25–278 °C, Acta Mater. 113 (2016) 221–229.
[18] M.O. Pekguleryuz, E. Baril, Creep resistant magnesium diecasting alloys based on alkaline earth elements, Mater. Trans. 42 (7) (2001) 1258–1267.
[19] P. Paufler, J. Marschner, G.E.R. Schulze, The mobility of grown-in dislocations in the intermetallic compound MgZn2 II. Stress dependence of basal slip at 390 °C, Phys. Status Solidi 43 (1) (1971) 279–282.
[20] P. Paufler, Deformation-mechanism maps of the intermetallic compound $MgZn_2$, Krist. Tech. 13 (5) (1978) 587–590.
[21] K.S. Kumar, Laves phase-based materials: microstructure, deformation modes and properties, MRS Proceedings 460 (2011).
[22] N. Takata, H. Ghassemi Armaki, Y. Terada, M. Takeyama, K.S. Kumar, Plastic deformation of the C14 Laves phase $(Fe,Ni)_2Nb$, Scripta Mater. 68 (8) (2013) 615–618.
[23] S. Korte-Kerzel, Microcompression of brittle and anisotropic crystals: recent advances and current challenges in studying plasticity in hard materials, MRS Communications 7 (2) (2017) 109–120.
[24] S. Korte, W.J. Clegg, Studying plasticity in hard and soft Nb–Co intermetallics, Adv. Eng. Mater. 14 (11) (2012) 991–997.
[25] F. Östlund, P.R. Howie, R. Ghisleni, S. Korte, K. Leifer, W.J. Clegg, J. Michler, Ductile–brittle transition in micropillar compression of GaAs at room temperature, Phil. Mag. 91 (7–9) (2011) 1190–1199.
[26] H. Kubsch, P. Paufler, G.E.R. Schulze, The mobility of grown-in dislocations in the intermetallic compound $MgZn_2$. III. Dependence of basal slip on chemical composition within the homogeneity range and on temperature, Phys. Status Solidi 56 (1) (1973) 231–234.
[27] H. Kubsch, P. Paufler, G.E.R. Schulze, The mobility of grown-in dislocations in the intermetallic compound $MgZn_2$ during prismatic slip, Phys. Status Solidi 25 (1) (1974) 269–275.
[28] T.H. Mueller, P. Paufler, Yield strength of the monocrystalline intermetallic compound $MgZn_2$, Phys. Status Solidi 40 (2) (1977) 471–477.
[29] P. Paufler, J. Marschner, G.E.R. Schulze, The mobility of grown-in dislocations in the intermetallic compound $MgZn_2$ I. Stress dependence for edge dislocations in prism slip at 390 °C, Phys. Status Solidi 40 (2) (1970) 573–579.
[30] P. Paufler, G.E.R. Schulze, Gleitsysteme innermetallischer verbindungen, Krist. Tech. 2 (4) (1967) K11–K14.
[31] P. Paufler, G.E.R. Schulze, Plastic deformation of the intermetallic compound $MgZn_2$, Phys. Status Solidi 24 (1) (1967) 77–87.
[32] P. Paufler, Early work on Laves phases in east Germany, Intermetallics 19 (4) (2011) 599–612.
[33] U. Krämer, G.E.R. Schulze, Gittergeometrische Betrachtung der plastischen Verformung von Lavesphasen, Krist. Tech. 3 (3) (1968) 417–430.
[34] D. Caillard, J.L. Martin (Eds.), Chapter 4 - Frictional Forces in Metals, Pergamon Materials Series, Pergamon, 2003, pp. 85–123.
[35] J.D. Livingston, Laves-phase superalloys? Phys. Status Solidi 131 (2) (1992) 415–423.
[36] N. Takata, H. Ghassemi-Armaki, Y. Terada, M. Takeyama, S. Kumar, Effect of dislocation sources on slip in Fe_2Nb laves phase with Ni in solution, MRS Proceedings 1516 (2012) 269–274.
[37] Y. Liu, J.D. Livingston, S.M. Allen, Defect structures and nonbasal slip of C36 laves phase $MgNi_2$ in a two-phase alloy, Metall. Mater. Trans. A 26 (6) (1995) 1441–1447.
[38] Y. Liu, S.M. Allen, J.D. Livingston, Deformation mechanisms in a laves phase, MRS Proceedings 288 (1992).
[39] M.L. Kronberg, Plastic deformation of single crystals of sapphire: basal slip and twinning, Acta Metall. 5 (9) (1957) 507–524.
[40] P.M. Hazzledine, P. Pirouz, Synchroshear transformations in Laves phases, Scripta Metall. Mater. 28 (10) (1993) 1277–1282.
[41] M.F. Chisholm, S. Kumar, P. Hazzledine, Dislocations in complex materials, Science 307 (5710) (2005) 701–703.

[42] K.S. Kumar, P.M. Hazzledine, Polytypic transformations in Laves phases, Intermetallics 12 (7) (2004) 763–770.
[43] Y. Liu, S.M. Allen, J.D. Livingston, Deformation of two C36 Laves phases by microhardness indentation at room temperature, Metall. Mater. Trans. A 26 (5) (1995) 1107–1112.
[44] A.V. Kazantzis, M. Aindow, G.K. Triantafyllidis, J.T.M. De Hosson, On the self-pinning character of synchro-Shockley dislocations in a Laves phase during strain rate cyclical compressions, Scripta Mater. 59 (7) (2008) 788–791.
[45] S. Korte, J.S. Barnard, R.J. Stearn, W.J. Clegg, Deformation of silicon – insights from microcompression testing at 25–500 °C, Int. J. Plast. 27 (11) (2011) 1853–1866.
[46] S. Korte, R.J. Stearn, J.M. Wheeler, W.J. Clegg, High temperature microcompression and nanoindentation in vacuum, J. Mater. Res. 27 (1) (2012) 167–176.
[47] W.C. Oliver, G.M. Pharr, An improved technique for determining hardness and elastic modulus using load and displacement sensing indentation experiments, J. Mater. Res. 7 (6) (1992) 1564–1583.
[48] Y. Liu, W.-C. Hu, D.-J. Li, K. Li, H.-L. Jin, Y.-X. Xu, C.-S. Xu, X.-Q. Zeng, Mechanical, electronic and thermodynamic properties of C14-type AMg_2 (A = Ca, Sr and Ba) compounds from first principles calculations, Comput. Mater. Sci. 97 (0) (2015) 75–85.
[49] Y. Liu, H. Ren, W.-C. Hu, D.-J. Li, X.-Q. Zeng, K.-G. Wang, J. Lu, First-principles calculations of strengthening compounds in magnesium alloy: a general review, J. Mater. Sci. Technol. 32 (12) (2016) 1222–1231.
[50] P. Mao, B. Yu, Z. Liu, F. Wang, Y. Ju, Mechanical, electronic and thermodynamic properties of Mg_2Ca Laves phase under high pressure: a first-principles calculation, Comput. Mater. Sci. 88 (2014) 61–70.
[51] I. Horcas, R. Fernández, J.M. Gómez-Rodríguez, J. Colchero, J. Gómez-Herrero, A.M. Baro, WSXM: a software for scanning probe microscopy and a tool for nanotechnology, Rev. Sci. Instrum. 78 (1) (2007) 013705.
[52] S. Schröders, S. Sandlöbes, C. Birke, M. Loeck, L. Peters, C. Tromas, S. Korte-Kerzel, Room temperature deformation in the Fe_7Mo_6 μ-Phase, Int. J. Plast. 108 (2018) 125–143.
[53] J. Hütsch, E.T. Lilleodden, The influence of focused-ion beam preparation technique on microcompression investigations: lathe vs. annular milling, Scripta Mater. 77 (2014) 49–51.
[54] Q. Yu, Z.-W. Shan, J. Li, X. Huang, L. Xiao, J. Sun, E. Ma, Strong crystal size effect on deformation twinning, Nature 463 (2010) 335.
[55] C.P. Frick, B.G. Clark, S. Orso, A.S. Schneider, E. Arzt, Size effect on strength and strain hardening of small-scale [111] nickel compression pillars, Mater. Sci. Eng., A 489 (1) (2008) 319–329.
[56] W.-Y. Yu, N. Wang, X.-B. Xiao, B.-Y. Tang, L.-M. Peng, W.-J. Ding, First-principles investigation of the binary AB_2 type Laves phase in Mg–Al–Ca alloy: electronic structure and elastic properties, Solid State Sci. 11 (8) (2009) 1400–1407.
[57] J.J. Qi, Y. Zhou, W. Wang, L.H. Qian, Z.Q. Lv, W.T. Fu, Electronic, magnetic and mechanical properties of $(Fe,Ni)_2Nb$ from density functional theory, J. Magn. Magn. Mater. 452 (2018) 219–229.
[58] N. Takata, H. Ghassemi-Armaki, M. Takeyama, S. Kumar, Nanoindentation study on solid solution softening of Fe-rich Fe_2Nb Laves phase by Ni in Fe–Nb–Ni ternary alloys, Intermetallics 70 (2016) 7–16.
[59] M.D. Uchic, P.A. Shade, D.M. Dimiduk, Plasticity of micrometer-scale single crystals in compression, Annu. Rev. Mater. Res. 39 (2009) 361–386.
[60] O. Kraft, P.A. Gruber, R. Mönig, D. Weygand, Plasticity in confined dimensions, Annu. Rev. Mater. Res. 40 (2010) 293–317.
[61] S. Korte, W. Clegg, Discussion of the dependence of the effect of size on the yield stress in hard materials studied by microcompression of MgO, Phil. Mag. 91 (7–9) (2011) 1150–1162.

Non-Newtonian Flow to the Theoretical Strength of Glasses via Impact Nanoindentation at Room Temperature

Christoffer Zehnder, Jan-Niklas Peltzer, James S. K.-L. Gibson, Doris Möncke,
Sandra Korte-Kerzel
Sci Rep 7, 17618 (2017).
https://doi.org/10.1038/s41598-017-17871-4

Short Summary

In many daily applications glasses are indispensable and novel applications demanding improved strength and crack resistance are appearing continuously. Up to now, the fundamental mechanical processes in glasses subjected to high strain rates at room temperature are largely unknown and thus guidelines for one of the major failure conditions of glass components are non-existent. Here, we elucidate this important regime for the first time using glasses ranging from a dense metallic glass to open fused silica by impact as well as quasi-static nanoindentation. We show that towards high strain rates, shear deformation becomes the dominant mechanism in all glasses accompanied by Non-Newtonian behaviour evident in a drop of viscosity with increasing rate covering eight orders of magnitude. All glasses converge to the same limit stress determined by the theoretical hardness, thus giving the first experimental and quantitative evidence that Non-Newtonian shear flow occurs at the theoretical strength at room temperature.

The authors contribution to this paper comprised conceptualization, methodology of the experimental work, investigating and analyzing the experimental data as well as writing the paper.

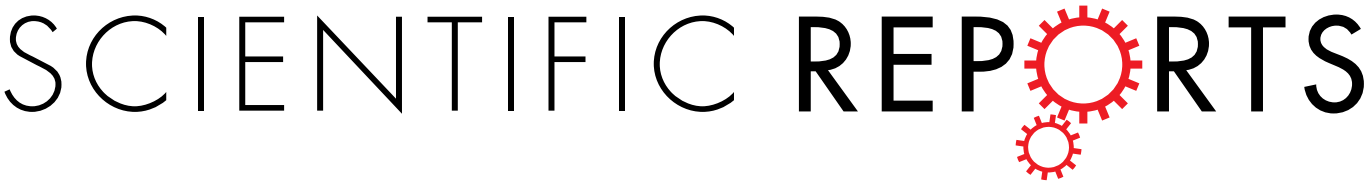

OPEN

Non-Newtonian Flow to the Theoretical Strength of Glasses via Impact Nanoindentation at Room Temperature

Received: 10 July 2017
Accepted: 1 December 2017
Published online: 15 December 2017

Christoffer Zehnder[1], Jan-Niklas Peltzer[1], James S. K.-L. Gibson[1], Doris Möncke[2,3] & Sandra Korte-Kerzel[1]

In many daily applications glasses are indispensable and novel applications demanding improved strength and crack resistance are appearing continuously. Up to now, the fundamental mechanical processes in glasses subjected to high strain rates at room temperature are largely unknown and thus guidelines for one of the major failure conditions of glass components are non-existent. Here, we elucidate this important regime for the first time using glasses ranging from a dense metallic glass to open fused silica by impact as well as quasi-static nanoindentation. We show that towards high strain rates, shear deformation becomes the dominant mechanism in all glasses accompanied by Non-Newtonian behaviour evident in a drop of viscosity with increasing rate covering eight orders of magnitude. All glasses converge to the same limit stress determined by the theoretical hardness, thus giving the first experimental and quantitative evidence that Non-Newtonian shear flow occurs at the theoretical strength at room temperature.

Glass shapes our way of life; from the basic needs of shelter and light to the modern ever-presence of the global networks on mobile devices. Yet deformation of glasses in exactly these applications, from static windows to flexibly loaded and frequently damaged displays, is in many aspects only poorly understood. Our current understanding is focused on the catastrophic fracture events in glasses, not their plastic deformation. In metals, it is the physical understanding of how deformation takes place down to the atomic level which has enabled scientists to improve technical alloys from steels to superalloys at staggering rates over the last decades. Unlike metals, glasses exhibit a short range order (SRO) represented by a few atoms building recurring structural units, but these do not stack periodically in three dimensions to give long range order (LRO). The underlying mechanisms in glasses must be inherently different compared to metals, due to the lack of crystalline order. Nevertheless, it is plastic deformation, either by densification of the glass network or shear flow, which accommodates scratches on transparent devices and, more importantly, competes with or pre-mediates fracture. To investigate and understand these mechanisms is crucial where new technologies, with their rapidly growing demands on strength and toughness of the materials and composites made from them, are to be implemented efficiently.

Until now, a vast yet most relevant regime has been missing from our ability to quantitatively measure and thus understand deformation in glasses: the low temperature and high strain rate regime, i.e. deformation conditions which correspond to the drop of a mobile device or the exposure of windows to sand-rich winds. Here, we demonstrate for the first time how these conditions may be studied quantitatively and systematically and that four distinctly different glasses show the same behaviour towards the extreme conditions at high rates and low temperatures far below the glass transition temperature. The presented insights enable an easy comparison between different materials and a preselection without having to conduct extensive experiments with different materials, simplifying the design process considerably.

The practical use of glasses is strongly linked to the resistance against crack initiation and more importantly crack growth, i.e. the toughness of a glass. These properties in turn are also determined by the dominant

[1]Institute of Physical Metallurgy and Metal Physics, RWTH Aachen University, Aachen, Germany. [2]Department of Built Environment and Energy Technology, Linnaeus University, Växjö, Sweden. [3]Theoretical and Physical Chemistry Institute, National Hellenic Research Foundation, Athens, Greece. Correspondence and requests for materials should be addressed to S.K.-K. (email: korte-kerzel@imm.rwth-aachen.de)

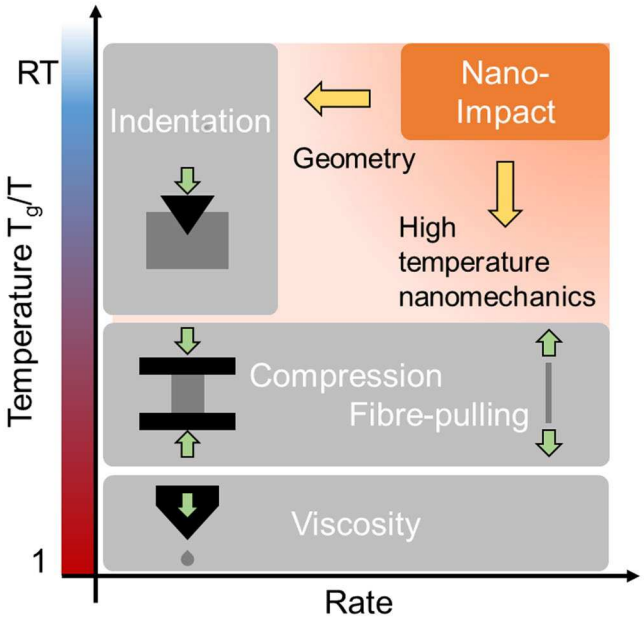

Figure 1. Previously inaccessible low temperature and high rate deformation regime now covered by impact nanoindentation testing. The experimental method in combination with in-depth analysis is envisioned to bridge the present characterisation gap between already available high temperature and indentation methods. Development of the required equipment has already been achieved in the context of other nano-mechanical test methods[11–13].

deformation mechanisms of flow. Depending on whether the glass deforms mainly by volume conservative shear or densification – compaction of the glass structure - it is referred to as normal or anomalous, respectively[1,2]. Activation of either results in different cracking behaviour[3] and depends not only on the structure and chemistry of the glass but also on the environmental and loading conditions, e.g. temperature and strain rate. The response of glasses to high strain rates is of special interest as a change in deformation characteristics has been seen with increasing strain rate for numerous glasses at high temperatures: at low strain rates, their viscosity is constant resulting in a linear increase of stress with increasing strain rate - Newtonian behaviour[4]. With increasing strain rate, deformation enters a non-Newtonian regime, where the viscosity decreases and the rate at which the stress increases with strain rate therefore decreases and finally converges to a constant level, becoming independent of the strain rate[4,5]. Whether this behaviour extends to low temperatures in glasses was previously unknown.

Up to now, it has simply not been possible to obtain detailed information from deformation experiments conducted both at room temperature and at high strain rates and allowing a quantitative analysis of deformation modes, e.g. activation of shear, densification and critical stress levels. (Nano)indentation, micropillar compression and diamond anvil cell experiments can be used to introduce plastic deformation at temperatures far below the glass transition temperature T_g, however, these are all normally limited to low strain rates[6,7]. At high temperature, fibre pulling and conventional macroscopic compression experiments[8] can be used to apply high strain rates, but these methods cannot be used at low temperatures as they result in premature fracture from pre-existing flaws[9]. Impact testing allows studies at high rates and variable temperature. However, classical methods, even in combination with high speed imaging, are still limited in terms of their quantitative interpretation and, due to the projectile size, the typical sample volumes within bulk samples are large enough to also contain statistically distributed intrinsic flaws governing deformation[10].

In contrast, nano-impact testing, i.e. instrumented (nano) indentation in a ballistic, high rate operation, offers the possibility to deform glasses plastically to high rates at room temperature. This is achieved by employing the same geometry as in quasi-static indentation and therefore inducing a confining pressure that suppresses fracture and enables plastic deformation in indentation of brittle materials in general. Until now, this approach only has found limited use in the characterisation of fused silica[11], sol-gel coatings[12] and magnesium alloys[13]. Its application is often limited by the oscillations that develop in an un-stiffened pendulum. Using the stiffening modifications shown to be effective by Jennet *et al.*[11], impact nanoindentation is now utilised here and applied to very high strain rates beyond the scope of conventional hardness measurements. The latter is realized by accelerating the tip into the sample by releasing a controlled elastic deformation introduced into the tip mount, and collecting the position-time-signal at a high acquisition rate during impact and several subsequent rebounds. By using different tip geometries and a high temperature setup, such experiments could span a wide range of strain rates (10^{-4}–$10^{5}\,s^{-1}$) and temperatures (≈150–1200 K)[14,15] entering regimes which have not been accessible so far by conventional methods (Fig. 1).

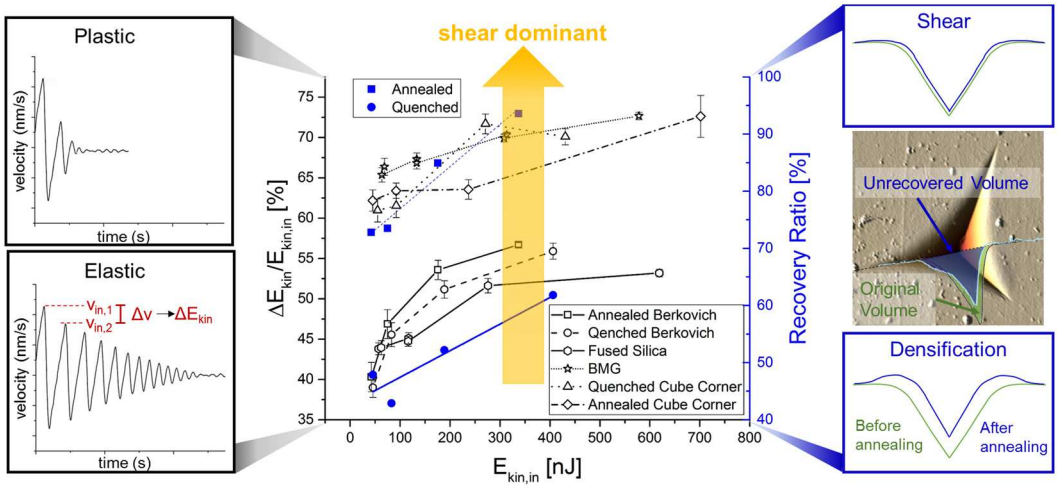

Figure 2. Influence of strain rate (determined by the plotted kinetic impact energy) on the ratio of shear and densification as well as plastic and elastic deformation. The energy loss ratio from the velocity-time data of impact-nanoindentation for different glasses yields consistent behaviour with the recovery ratio for the indented volume derived from annealing experiments and subsequent AFM analysis. An increasing amount of shear deformation is correlated with an increase in energy loss, or plastic deformation, during the first indent and found, consistent with glass structure and stress state, towards the densest glass networks and smaller hydrostatic stress component.

Results and Discussion

In this study, different glass systems have been tested at room temperature over strain rates spanning seven orders of magnitude by using quasi-static nano-indentation and dynamic impact-nanoindentation. To cover a maximum diversity of glasses, the most anomalous glass, fused silica, and a glass presenting the normal, shear dominated extreme, a bulk metallic glass (BMG), were chosen. Additionally, a sodium-borosilicate glass (NBS) was subjected to two different thermal treatments resulting in an open structure (quenched) and a dense structure (annealed) and included into this study to change the extent of normal and anomalous behaviour within one glass composition[16,17]. To vary the hydrostatic stress component and hence the relative fraction of densification during deformation[18], the NBS glasses were additionally tested with two different tip geometries: a sharp cube corner and a comparatively flat Berkovich tip.

While it is well known how these glasses behave at low strain rates and room temperature[6,19–21], there is no information how shear and densification, stress and viscosity develop towards high rates at room temperature. To obtain this crucial information, a new methodology is presented here analysing different parameters of the position-time-data recorded in each experiment during impact nanoindentation. Two of these are of special interest: the energy loss ratio and the dynamic hardness. The energy loss ratio represents the energy dissipated during impact and thus the ratio of plastic and elastic deformation; an increasing energy loss ratio corresponds to a shift from elastic to plastic deformation. The dynamic hardness gives a measure of the resistance to impact deformation by taking the dissipated energy over the volume plastically displaced by the tip during the very first impact.

In terms of the energy loss ratio, all samples show the same trend (Fig. 2): an increase of energy loss ratio and thus plastic deformation with increasing strain rate (determined by the impact energy). AFM measurements show that the samples tested with the Berkovich tip do not form cracks so that the complete energy loss is due to plastic deformation and not influenced by cracking. To investigate the amount of densification and shear contributing to the plastic deformation at increasing rates, annealing treatments were conducted on the two NBS glasses after impact indentation. It was found that both samples reveal a shift from densification to shear deformation with increasing strain rate, so that the increase in plastic deformation - indicated by the increase in energy loss ratio - appears to be accommodated to a greater extend by shear flow as the strain rate increases. Interestingly, the related changes in energy loss ratio are consistent with this transition both in terms of the dominant deformation mechanisms for each glass and the induced stress components: an increased shear flow component is expected in glasses where densification is less dominant and where the impact tip geometry is sharper, reducing the hydrostatic pressure. This is reflected in the experiment in terms of the energy loss ratio enveloped by the open fused silica structure at the lower and the dense bulk metallic glass at the upper end as well as an increase in energy loss ratio from the flat Berkovich geometry to the sharper cube corner tip.

These data suggest that an increasing strain rate shifts the governing mechanism of deformation towards shear flow in the investigated glasses showing both densification and shear. We then measured the hardness and viscosity across seven orders of magnitude. At high temperatures, measurements of the viscosity reported in the literature have identified non-Newtonian flow[22]. A central question is therefore how this non-Newtonian flow might change, or not, as the temperature is reduced to room temperature, i.e. the brittle regime where macroscopically deformation is governed by fast fracture from statistically distributed flaws.

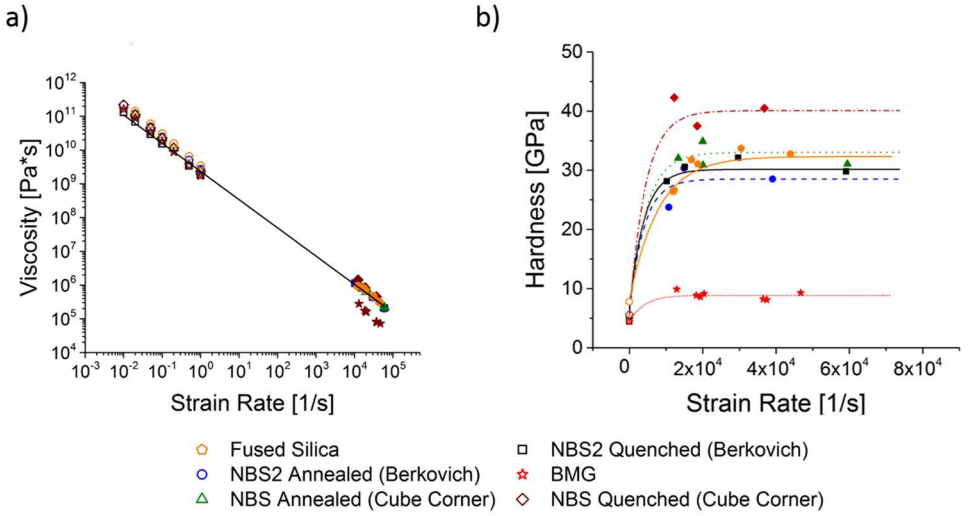

Figure 3. Dependence of (**a**) viscosity and (**b**) hardness on increasing strain rate for different materials tested by quasi-static and impact nanoindentation across seven orders of magnitude. The viscosity exhibits a linear change with strain rate in double logarithmic presentation (see Fig. 4 for a double logarithmic plot of the normalised hardness). The filled symbols correspond to the impact indentation tests, the empty ones to quasi-static indentation.

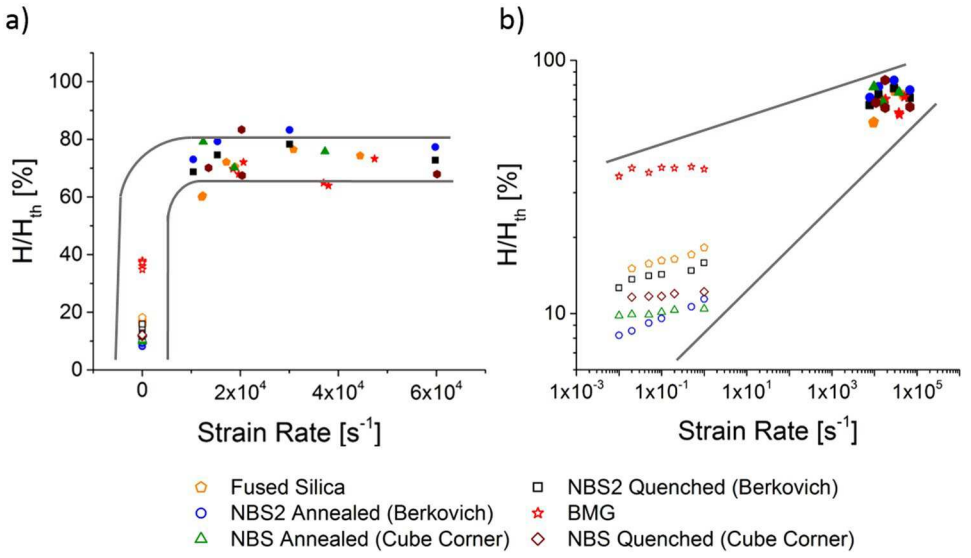

Figure 4. Hardness during quasi-static and impact nanoindentation of different materials normalized by their theoretical hardness over indentation/impact strain rate. The normalized hardness converges to approximately 75% H_{th} at high rates for all glasses. The high and low rate regimes are expanded for clarity in an (**a**) linear and (**b**) logarithmic scaling of the rate axis, respectively.

Non-Newtonian behaviour manifests in two characteristic trends: a decreasing viscosity and therefore a decreasing rate of stress increase with strain rate, after which the stress converges to a constant value at high strain rates. Over the complete range of measurements, the viscosity decreases linearly (Fig. 3), connecting the quasi-static and the impact measurements across seven orders of magnitude from indentation/impact strain rates of $10^{-2}s^{-1}$ to $10^{4}s^{-1}$. This linear drop in viscosity is in excellent agreement with the expected change in viscosity for a typical shear thinning material, as has been shown for glasses near T_g but has not been possible to show directly in experiments at room temperature before[4,5,23–25].

Parallel to this linear drop in viscosity, the hardness rises towards higher rates and at the highest rates, converges towards a single value or, in a linear representation, exhibits a plateau stress (Fig. 3b). Together with the decreasing viscosity, the transition between these two deformation regimes demonstrates for the first time the existence of non-Newtonian behaviour with shear thinning at room temperature.

In absolute terms, the limit stresses for each of the different glasses varies, just as the other physical parameters describing structure, bond strength or density. Most commonly, the limit strength at high rates and temperatures

has been associated with structural rearrangements and it is assumed that the stress level is determined by the theoretical strength, σ_{th}, which can be derived as[5]:

$$\sigma_{th} = \sqrt{\frac{E\gamma}{r_o}} \tag{1}$$

with E the elastic modulus, γ the interface energy and r_o the atomic equilibrium distance.

Taking the theoretical strength and modulus, the theoretical hardness for every material tested was derived. According to Marsh[26], the glass strength can be converted into a hardness using a constraint factor, which depends on the material and in particular the relative importance of plastic and elastic deformation, i.e. the ratio of strength to elastic modulus (values used for each glass are given in the Materials and Methods section). All four glasses show a plateau at approximately 75% of their theoretical hardness (Fig. 4). This implies not only that non-Newtonian flow takes place in all samples at room temperature but also that the way it develops is similar in all of them. This result is of particular interest as the samples chosen span the complete range of deformation modes in glasses starting at the anomalous extreme in fused silica over two boro-silicate glasses showing both densification and shear in different amount to the normal, shear dominated extreme of a BMG.

Conclusions

Despite a manifold of experimental and theoretical evidence near the glass transition, it has not been possible to extract the exact mechanisms governing non-Newtonian flow and the importance of the theoretical strength in glasses. The extension of the experiments to a temperature far below T_g will therefore support the quest for the atomistic mechanisms of deformation at high rates by legitimizing interpretation of atomistic simulations at small scales and at short time scales via the now available experiments and additional insights at room temperature. These not only give evidence to continuous flow mechanisms across temperatures at high rates, where thermal activation becomes limited, but also provide an essential approach to guide modelling of glass deformation. In extending the large available datasets and models for mechanical properties at low rates, it is now possible to derive an approximate strength at high strain rates in a simple way from basic glass properties by deriving the theoretical strength.

The approach and insights presented here, employing impact nanoindentation to reveal shear thinning in different glasses at room temperature, therefore offer the possibility to choose glasses and characterize or model their performance in the highly relevant room temperature impact regime more efficiently. In particular, an easily applied method to characterize flow at high rates and low temperature is now available to researchers, as well as for developers facing a choice of glass system for devices or components exposed to impact loading. It has been demonstrated that modelling of high rate deformation may perhaps simply be approximated by non-Newtonian flow limited by the theoretical strength across glass structures.

Materials and Methods

Different glass samples were investigated: fused silica, a bulk metallic glass (BMG) and two sodium-borosilicate (NBS) samples of the same glass, but subjected to different thermal treatments. The NBS glass ($74SiO_2$–$20.7B_2O_3$-$4.3Na_2O$-$1Al_2O_3$) was melted and homogenized at 1650 °C. The melt was then cast either onto a brass block (left at room-temperature) or into a graphite mould, which had been preheated to 700 °C. The 700 °C mould was furthermore slowly cooled down to room temperature with 30 K/h, resulting in a relaxed, compact structure, this state is henceforth referred to as "annealed"[16,17]. The sample cast onto the brass block was additionally quenched by another brass stamp to quickly dissipate the heat, resulting in an open structure, and is henceforth referred to as "quenched"[27]. The BMG used in this study was a 'Vitreloy' from Liquid metals, a $Zr_{41.2}Be_{22.5}Ti_{13.8}Cu_{12.5}Ni_{10.0}$ metallic glass.

For quasi-static indentation (iNano, Nanomechanics Inc., USA), a maximum load of 45 mN was chosen and strain rates ranging from 0.01 to 1 s^{-1} were applied using a diamond Berkovich tip.

AFM measurements (XE-70 , Park Systems) were conducted with scan speeds of 0.1 µm/s and a resolution of 512 × 512 pixels.

For impact nanoindentation, a pendulum-based system was used (Fig. 5a) (NanoTest Platform III, Micromaterials Ltd.). By applying a voltage to the coil on the top end of the pendulum, a rotation around the pivot is induced, resulting in a forward movement of the tip. Prior to this, the lower electromagnet can be used to stress the pendulum. By releasing it, the pendulum swings forward with a high acceleration, resulting in a nano-impact indentation on the sample. These impact nanoindentation experiments were conducted using loads between 10 mN and 100 mN with an initial distance between tip and sample in the stressed state of 5 µm. At every load 15 tests were conducted per sample. A flat Berkovich tip and a sharp cube corner tip were used, both consisted of diamond.

In impact nanoindentation, the tip hits the sample with a high velocity, indenting by producing elastic and plastic deformation. At the point of maximum indentation depth, the elastic deformation will be reversed, resulting in a backward movement of the tip. This will even cause the tip to leave the sample and be stressed again. This procedure repeats several times until all energy is absorbed by the sample. Figure 5b displays a typical depth-time curve. Although this results in repeated impacts of the sample, only the first impact is considered in the analysis of the materials: dynamic hardness, energy loss ratio and strain rate (detailed subsequently) are all calculated from the initial contact.

Several important parameters can be determined from these data: from the depth-time curve, velocity-time curves can be derived. By using an effective mass of the pendulum, the kinetic energy can be estimated. With this information the dynamic hardness and the energy loss ratio are calculated. To derive the dynamic hardness,

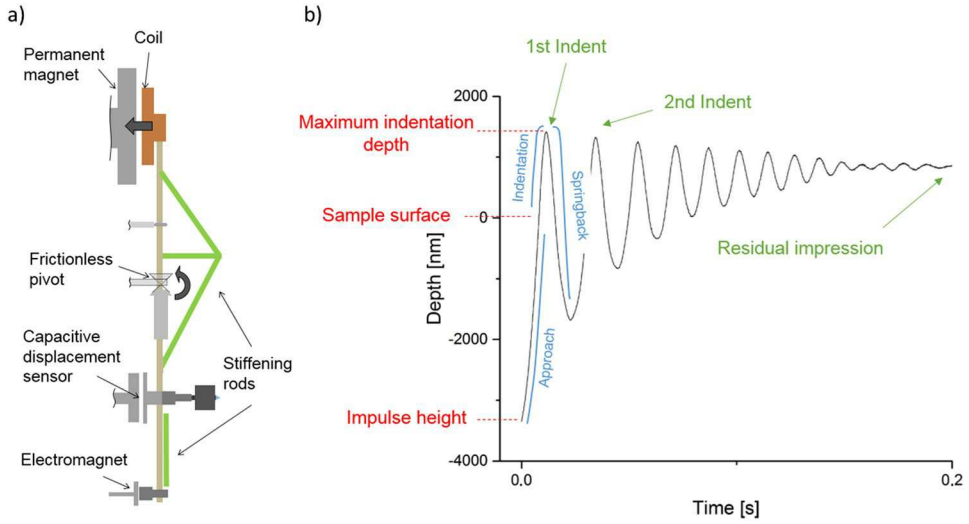

Figure 5. Experimental setup of the impact nano-indenter (**a**). By applying voltage to the coil on the top end of the pendulum, a rotation around the pivot will be induced, resulting in a forward movement of the tip. The lower electromagnet can be used to stress the pendulum and accelerate it quickly towards the sample. A typical depth-time curve (**b**) is displayed with the important parameters marked in the graphs.

H_{dyn}, the energy loss between the first and the second indent is taken, derived from the maximum velocities right before the indenter hits the sample for the first and the second time[12,28]. Here improved data quality allows us to use the plastic volume of the first impact, V_{plast}, rather than the conventionally used volume of the final impression, giving:

$$H_{dyn} = \frac{\frac{1}{2} m_{eff} (v_{in,2}^2 - v_{in,1}^2)}{V_{plast}} \tag{2}$$

with m_{eff} the effective mass of the pendulum, $v_{in,1}$ and $v_{in,2}$ the maximum velocities right before the indent hits the sample for the first and the second time, respectively, and V_{plast} the plastic volume after the first impact.

The second important parameter is the energy loss ratio (ELR):

$$ELR = \frac{E_{kin,2} - E_{kin,1}}{E_{kin,1}} \tag{3}$$

with $E_{kin,1}$ and $E_{kin,2}$ being the kinetic energy of the pendulum right before the first and second indent, respectively. This value describes the amount of energy lost during the first impact, i.e. the amount of plastic deformation. By normalising it to the kinetic energy of the pendulum before the first impact, the ratio between elastic and plastic deformation can be analysed with a high ELR corresponding to a high amount of plastic deformation. It can be shown that the maximum kinetic energy right after leaving the sample and hitting it the next time is the same so that it can be stated that no energy is lost during the springback of the pendulum between two indentations. Also the ELR shows similar trends for the samples tested with a Berkovich and a cube corner tip. Interestingly, the Berkovich indents do not show cracking while the cube corner indents all show cracking. This means that the effect of cracking on the ELR is not dominant.

To analyse the data in a physically meaningful way, the strain rate must be determined. For this, the typical indentation strain rate[29] was used:

$$\dot{\varepsilon} = \frac{\dot{h}}{h} \tag{4}$$

with h being the indentation depth and $\dot{h}$ being the velocity. As the strain and stress field during indentation is spatially inhomogeneous, the strain rate, hardness, viscosity or even the modulus have to be considered as a representative value for a certain volume (and direction in anisotropic materials), in analogy to the hardness being interpreted as the flow stress at a specific strain of 8%[30]. This makes direct comparison of indentation test to uniaxial measurements challenging. Nevertheless, it has been shown that the indentation strain rate determined by equation 4 can be set to be constant during an indentation experiment and under these conditions good correlation with uniaxial testing is commonly observed[29,31–33].

Different to quasi-static indentation, where the strain rate can be controlled throughout the complete experiment, the strain rate decreases constantly with increasing indentation depth in impact nano-indentation. To compare different measurements, one depth must be selected at which the strain rate is measured as the representative strain rate of the experiment. As tip rounding will have a very strong influence on the measured values

Material	Theoretical strength [GPa]	Constraint factor	Theoretical hardness [GPa]
BMG	5.46	2.33	12.73
Fused Silica	35.54	1.25	44.50
NBS Quenched (Berkovich)	30.45	1.36	41.37
NBS Annealed (Berkovich)	30.45	1.28	38.89
NBS Quenched (cube corner)	30.45	1.52	46.17
NBS Annealed (cube corner)	30.45	1.77	53.92

Table 1. Theoretical Strength, constraint factor and theoretical hardness for the different materials tested.

below 50 nm, especially in impact mode, in this study the strain rate at 50 nm was taken as the strain rate of the complete indentation cycle to compare different experiments. With these dynamic hardness and strain rate values, the viscosity can be determined in indentation experiments by the following equation[34]:

$$\eta = \frac{H_{dyn}}{2(1+\nu)\dot{\varepsilon}} \tag{5}$$

with η the viscosity and ν the Poisson ratio.

In order to investigate the amount of shear and densification, AFM measurements were conducted. When glasses are subjected to temperatures near the glass transition, here 0.9 T_g for 2 hours, it has been shown that densification can be fully reversed[18] while shear deformation is still overwhelmingly present. By measuring the volume using AFM before and after annealing, the amount of unrecovered volume can be determined and in this way a recovery ratio, the unrecovered volume divided by the initial volume, can be derived constituting the amount of unrecovered deformation, produced by shear that is largely — if not entirely — unaffected by a short annealing treatment[18].

In order to compare the different materials, the theoretical strength was calculated and transferred into a theoretical hardness using a constraint factor according to Marsh[26]. Table 1 lists the parameters for theoretical strength, constraint factor and hardness used for the different materials:

References

1. Arora, A., Marshall, D. B., Lawn, B. R. & Swain, M. V. Indentation deformation/fracture of normal and anomalous glasses. *Journal of Non-Crystalline Solids* **31**, 415–428, https://doi.org/10.1016/0022-3093(79)90154-6 (1979).
2. Peter, K. W. Densification and flow phenomena of glass in indentation experiments. *Journal of Non-Crystalline Solids* **5**, 103–115, https://doi.org/10.1016/0022-3093(70)90188-2 (1970).
3. Cook, R. F. & Pharr, G. M. Direct observation and analysis of indentation cracking in glasses and ceramics. *Journal of the American Ceramic Society* **73**, 787–817, https://doi.org/10.1111/j.1151-2916.1990.tb05119.x (1990).
4. Yue, Y. & Brückner, R. A new description and interpretation of the flow behaviour of glass forming melts. *Journal of Non-Crystalline Solids* **180**, 66–79, https://doi.org/10.1016/0022-3093(94)90398-0 (1994).
5. Simmons, J. H., Mohr, R. K. & Montrose, C. J. Non-Newtonian viscous flow in glass. *Journal of Applied Physics* **53**, 4075–4080, https://doi.org/10.1063/1.331272 (1982).
6. Schuh, C. A. & Nieh, T. G. A nanoindentation study of serrated flow in bulk metallic glasses. *Acta Materialia* **51**, 87–99, https://doi.org/10.1016/S1359-6454(02)00303-8 (2003).
7. Dubach, A., Raghavan, R., Löffler, J. F., Michler, J. & Ramamurty, U. Micropillar compression studies on a bulk metallic glass in different structural states. *Scripta Materialia* **60**, 567–570, https://doi.org/10.1016/j.scriptamat.2008.12.013 (2009).
8. Harmon, J. S., Demetriou, M. D., Johnson, W. L. & Samwer, K. Anelastic to plastic transition in metallic glass-forming liquids. *Physical Review Letters* **99**, 135502 (2007).
9. Griffith, A. A. The phenomena of rupture and flow in solids. *Philosophical Transactions of the Royal Society A* **221**, 163–198, https://doi.org/10.1098/rsta.1921.0006 (1921).
10. Chaudhri, M. M. & Liangyi, C. The catastrophic failure of thermally tempered glass caused by small-particle impact. *Nature* **320**, 48–50, https://doi:10.1038/320048a0 (1986).
11. Jennett, M. & Nunn, J. High resolution measurement of dynamic (nano) indentation impact energy: a step towards the determination of indentation fracture resistance. *Philosophical Magazine* **91**, 1200–1220, https://doi.org/10.1080/14786435.2010.485585 (2010).
12. Wheeler, J. M. & Gunner, A. G. Analysis of failure modes under nano-impact fatigue of coatings via high-speed sampling. *Surface and Coatings Technology* **232**, 264–268, https://doi.org/10.1016/j.surfcoat.2013.05.028 (2013).
13. Somekawa, H. & Schuh, C. A. High-strain-rate nanoindentation behavior of fine-grained magnesium alloys. *Journal of Materials Research* **27**, 1295–1302, https://doi.org/10.1557/jmr.2012.52 (2012).
14. Harris, A. J., Beake, B. D. & Armstrong, D. E. J. Extreme nanomechanics: vacuum nanoindentation and nanotribology to 950 °C. *Tribology - Materials, Surfaces & Interfaces* **9**, 174–180, https://doi.org/10.1080/17515831.2015.1107345 (2015).
15. Lee, S.-W., Meza, L. & Greer, J. R. Cryogenic nanoindentation size effect in [0 0 1]-oriented face-centered cubic and body-centered cubic single crystals. *Applied Physics Letters* **103**, 101906, https://doi.org/10.1063/1.4820585 (2013).
16. Zehnder, C. *et al*. Influence of Cooling Rate on Cracking and Plastic Deformation during Impact and Indentation of Borosilicate Glasses. *Frontiers in Materials* **4**, https://doi.org/10.3389/fmats.2017.00005 (2017).
17. Malchow, P. *et al*. Composition and cooling-rate dependence of plastic deformation, densification, and cracking in sodium borosilicate glasses during pyramidal indentation. *Journal of Non-Crystalline Solids* **419**, 97–109, https://doi.org/10.1016/j.jnoncrysol.2015.03.020 (2015).
18. Yoshida, S., Sanglebœuf, J.-C. & Rouxel, T. Quantitative evaluation of indentation-induced densification in glass. *Journal of Materials Research* **20**, 3404–3412, https://doi.org/10.1557/jmr.2005.0418 (2005).
19. Schuh, C. A., Hufnagel, T. C. & Ramamurty, U. Mechanical behavior of amorphous alloys. *Acta Materialia* **55**, 4067–4109, https://doi.org/10.1016/j.actamat.2007.01.052 (2007).
20. Demetriou, M. D. *et al*. A damage-tolerant glass. *Nature Materials* **10**, 123–128, http://www.nature.com/nmat/journal/v10/n2/abs/nmat2930.html#supplementary-information (2011).

21. Kermouche, G., Guillonneau, G., Michler, J., Teisseire, J. & Barthel, E. Perfectly plastic flow in silica glass. *Acta Materialia* **114**, 146–153, https://doi.org/10.1016/j.actamat.2016.05.027 (2016).
22. Simmons, J. H. What is so exciting about non-linear viscous flow in glass, molecular dynamics simulations of brittle fracture and semiconductor–glass quantum composites. *Journal of Non-Crystalline Solids* **239**, 1–15, https://doi.org/10.1016/S0022-3093(98)00741-8 (1998).
23. Simmons, J. H., Ochoa, R., Simmons, K. D. & Mills, J. J. Non-Newtonian viscous flow in soda-lime-silica glass at forming and annealing temperatures. *Journal of Non-Crystalline Solids* **105**, 313–322, https://doi.org/10.1016/0022-3093(88)90325-0 (1988).
24. Kato, H., Kawamura, Y. & Inoue, A. Newtonian to non-Newtonian master flow curves of a bulk glass alloy $Pd_{40}Ni_{10}Cu_{30}P_{20}$. *Applied Physics Letters* **73**, 3665–3667, https://doi.org/10.1063/1.122856 (1998).
25. Brückner, R., Yue, Y. & Habeck, A. Determination of rheological properties of high-viscous glass melts by the cylinder compression method. *Glass Science and Technology* **67** (1994).
26. Marsh, D. M. Plastic flow in glass. *Proceedings of the Royal Society A* **279**, 420–435, https://doi.org/10.1098/rspa.1964.0114 (1964).
27. Möncke, D. Tricot, G., Ehrt, D., Efstratios, I. & Kamitsos, E.I. Connectivity of borate and silicate groups in a low-alkali borosilicate glass by vibrational and 2D NMR spectroscopy. *Journal of Chemical Technology and Metallurgy* **50**, 381–386 (2015).
28. Trelewicz, J. R. & Schuh, C. A. The Hall–Petch breakdown at high strain rates: Optimizing nanocrystalline grain size for impact applications. *Applied Physics Letters* **93**, 171916, https://doi.org/10.1063/1.3000655 (2008).
29. Lucas, B. N. & Oliver, W. C. Indentation power-law creep of high-purity indium. *Metallurgical and Materials Transactions A* **30**, 601–610 (1999).
30. Tabor, D. The hardness of solids. *Review of Physics in Technology* **1**, 145 (1970).
31. Maier, V. *et al.* Nanoindentation strain-rate jump tests for determining the local strain-rate sensitivity in nanocrystalline Ni and ultrafine-grained Al. *Journal of Materials Research* **26**, 1421–1430, https://doi.org/10.1557/jmr.2011.156 (2011).
32. Schwaiger, R., Moser, B., Dao, M., Chollacoop, N. & Suresh, S. Some critical experiments on the strain-rate sensitivity of nanocrystalline nickel. *Acta Materialia* **51**, 5159–5172, https://doi.org/10.1016/S1359-6454(03)00365-3 (2003).
33. Maier-Kiener, V. & Durst, K. Advanced nanoindentation testing for studying strain-rate sensitivity and activation volume. *JOM* **69**, 2246–2255, https://doi.org/10.1007/s11837-017-2536-y (2017).
34. Guin, J.-P. *et al.* Indentation creep of Ge–Se chalcogenide glasses below Tg: elastic recovery and non-Newtonian flow. *Journal of Non-Crystalline Solids* **298**, 260–269, https://doi.org/10.1016/S0022-3093(01)01053-5 (2002).

Acknowledgements

We are grateful to the Deutsche Forschungsgemeinschaft (DFG) for funding (KO4603/1-1) within the framework of the Priority Programme SPP 1594 – "Topological Engineering of Ultrastrong Glass". We would also like to express our thanks to Prof. Conradt (GHI, RWTH Aachen) and Dr. Chaudhri (University of Cambridge) for many fruitful discussions.

Author Contributions

S.K.-K. conceived the project, C.Z. and J.-N.P. conducted the experiments, D.M. produced the samples, C.Z., J.S. K.-L.G. and S.K.-K. analyzed the results, C.Z., J.S. K.-L.G. and S.K.-K. wrote the manuscript, all authors reviewed the manuscript.

Additional Information

Competing Interests: The authors declare that they have no competing interests.

Publisher's note: Springer Nature remains neutral with regard to jurisdictional claims in published maps and institutional affiliations.

On extracting mechanical properties from nanoindentation at temperatures up to 1000 ◦C

James S.K.-L. Gibson, Sebastian Schröders, Christoffer Zehnder, Sandra Korte-Kerzel
Extreme Mechanics Letters, Volume 17, 2017, Pages 43-49
https://doi.org/10.1016/j.eml.2017.09.007.

Short Summary

Alloyed MCrAlY bond coats, where M is usually cobalt and/or nickel, are essential parts of modern turbine blades, imparting environmental resistance while mediating thermal expansivity differences. Nanoindentation allows the determination of their properties without the complexities of traditional mechanical tests, but was not previously possible near turbine operating temperatures.
Here, we determine the hardness and modulus of CMSX-4 and an Amdry-386 bond coat by nanoindentation up to 1000 ◦C. Both materials exhibit a constant hardness until 400 ◦C followed by considerable softening, which in CMSX-4 is attributed to the multiple slip systems operating underneath a Berkovich indenter. The creep behaviour has been investigated via the nanoindentation hold segments. Above 700 ◦C, the observed creep exponents match the temperature-dependence of literature values in CMSX-4. In Amdry-386, nanoindentation produces creep exponents very close to literature data, implying high-temperature nanoindentation may be powerful in characterising these coatings and providing inputs for material, model and process optimisations.

The authors contribution to this paper comprised conceptualization, methodology of the experimental work and performing the nanoindentation experiments.

Extreme Mechanics Letters 17 (2017) 43–49

Contents lists available at ScienceDirect

Extreme Mechanics Letters

journal homepage: www.elsevier.com/locate/eml

On extracting mechanical properties from nanoindentation at temperatures up to 1000 °C

James S.K.-L. Gibson *, Sebastian Schröders, Christoffer Zehnder, Sandra Korte-Kerzel *

RWTH Aachen University, Institut für Metallkunde und Metallphysik, Aachen, Germany

ARTICLE INFO

Article history:
Received 8 June 2017
Received in revised form 8 August 2017
Accepted 21 September 2017
Available online 4 October 2017

Keywords:
Nanoindentation
Hardness
Creep
Nickel superalloy

ABSTRACT

Alloyed MCrAlY bond coats, where M is usually cobalt and/or nickel, are essential parts of modern turbine blades, imparting environmental resistance while mediating thermal expansivity differences. Nanoindentation allows the determination of their properties without the complexities of traditional mechanical tests, but was not previously possible near turbine operating temperatures.

Here, we determine the hardness and modulus of CMSX-4 and an Amdry-386 bond coat by nanoindentation up to 1000 °C. Both materials exhibit a constant hardness until 400 °C followed by considerable softening, which in CMSX-4 is attributed to the multiple slip systems operating underneath a Berkovich indenter.

The creep behaviour has been investigated via the nanoindentation hold segments. Above 700 °C, the observed creep exponents match the temperature-dependence of literature values in CMSX-4. In Amdry-386, nanoindentation produces creep exponents very close to literature data, implying high-temperature nanoindentation may be powerful in characterising these coatings and providing inputs for material, model and process optimisations.

1. Introduction

Gas turbines are widely used in both the aerospace industry and in land-based power generation. In both these sectors, there exists a strong driving force to increase operating temperatures for both fuel efficiency and a reduction in carbon emissions. In power generation, a one-percent improvement in efficiency can save $20 million in fuel over the lifetime of the plant [1]. In order to facilitate these increases, refinement of the coatings used in the turbine blades is required, as this prevents premature component failure from chemical attack and oxidation. Due to the small thickness of these coatings, traditional mechanical testing is extremely challenging.

Nanoindentation – whereby an indenter of a specific geometry is driven into the surface of a material under an applied load – has been widely used to determine the mechanical properties of thin films, either in the form of hard coatings [2,3] or modified surface layers [4,5]. The application of this technique and related nanomechanical testing at elevated temperatures is a relatively recent, but increasingly popular field, with indentation temperatures and publications rapidly increasing year-on-year [6–16]. It is also a potential breakthrough in the development of high temperature materials. As a technique, nanoindentation allows the quick determination of hardness, indentation modulus and creep resistance [17] on small volumes, enabling the mechanical testing of thin coatings to be carried out. Operation in vacuum additionally prevents deleterious oxidation of the sample or the indenter tip [12,15,16]. Nanoindentation has been applied to superalloy materials [18,19] and their bond coats [20–23] with high-temperature nanoindentation recorded on CMSX-4 up to 400 °C [7] and René N4 up to 800 °C [24]. However, both works on high-temperature nanoindentation note the experimental difficulties – particular in the measurement of Young's modulus – due to creep during nanoindentation.

This work demonstrates the extension of high-temperature nanoindentation up to 1000 °C, allowing mechanical data, including creep exponents, to be determined at operationally-relevant temperatures on a sample of CMSX-4 and a 200 μm thick Amdry-386 bond coat. In application, this bond coat provides environmental resistance and mediates thermal stresses between the superalloy and thermal barrier coating. The single crystalline CMSX-4 serves as a well-studied, but highly anisotropic reference material, while the polycrystalline bond coat is well suited to this and future studies by nanoindentation due to the more isotropic behaviour with small grain sizes, its intrinsically small size with regards to the thickness, and the interest in its high temperature properties for coating design.

* Corresponding authors.
E-mail addresses: gibson@imm.rwth-aachen.de (J.S.K.-L. Gibson), korte-kerzel@imm.rwth-aachen.de (S. Korte-Kerzel).

https://doi.org/10.1016/j.eml.2017.09.007
2352-4316/

2. Experimental methods

Single-crystal CMSX-4 (Ni-9.6Co-6.5Cr-6.5Ta-6.4W-5.6Al-0.6 Mo-1Ti-3Re-0.1Hf, wt%) was grown with an orientation close to [001] and subjected to a standard heat treatment to form the γ–γ' structure. The sample was polished to a mirror finish using standard metallographic techniques, finished with 20 nm colloidal silica. An FEI Helios focussed ion beam (FIB) with EDAX EBSD (electron backscatter diffraction) and EDX (energy dispersive X-ray) detectors was used to determine the grain orientations of the sample and to cross-section an indent for analysis (Fig. 4). An Amdry-386 (Ni-22Co-17Cr-12Al-0.5Y-0.5Hf-0.2Si, wt%) bond coat was thermally-sprayed onto the superalloy. EBSD performed on the superalloy and bond coat (see supplementary material, Appendix A) showed the Amdry-386 consists mainly of 2–3 μm, equiaxed grains.

Tests were performed using a MicroMaterials NanoTest P-3 system modified by a custom-built vacuum chamber ($\sim 10^{-5}$ mbar). Indents were performed to a depth of 1 μm using an independently-heated Berkovich sapphire tip at a constant load rate of 2 mN/s, followed by a 30 s dwell period and 5 mN/s unloading rate. Up to 700 °C, at least 18 indents were made in the CMSX-4 and 12 indents in the bond coat at each temperature. At 900 °C and 1000 °C only two indents were made in each of the CMSX-4 and Amdry-386 as a larger number of indents at 1000 °C resulted in blunting of the tip due to tip-sample reactions and/or deposition of sample material as confirmed by atomic force microscopy (AFM) (see supplementary material, Appendix A). The diamond area function (DAF) of the tip was determined prior to testing and after testing at 700 °C by indenting into fused silica at room temperature. Additional indents to 500 mN in fused silica were used to calibrate the stiffness of the load frame. The initial DAF was used to analyse the data [25] up to 700 °C and the post-700 °C DAF – which was only minimally different – was used for the data obtained at 900 °C and 1000 °C. Due to the extreme temperatures used, the temperature-dependent Poisson's ratios (ν) of CMSX-4 and Al_2O_3 and temperature-dependent Young's modulus (E) of Al_2O_3 were used for the conversion of reduced modulus to Young's modulus for the CMSX-4 and Amdry-386 (ν from [26] and [27], E from [28]). This temperature-dependence corresponds to a change of ~8% in $E_{Al_2O_3}$ and $\nu_{CMSX\text{-}4}$, and ~5% in $\nu_{Al_2O_3}$.

3. Results

3.1. Nanoindentation data analysis

No variation of hardness with position was observed in either material at a given temperature. This is unsurprising for single-crystal CMSX-4 and the small grain size of the bond coat relative to the indent size [29]. The crystal structure of the bond coat was not explicitly determined, but the successful indexing by EBSD with a nickel input file, as well as literature data [30], strongly suggests an FCC structure is present. No plastic anisotropy is therefore expected. As a result, data from each material were averaged for better statistics.

Load–displacement behaviour with temperature is shown in Fig. 1, with all data plotted with the same scale and the time of each segment (at 25 °C) given in Fig. 1(a). Thermal drift is measured at 90% unload, where the load–displacement data imply that above 550 °C, thermal drift becomes significantly worse. There is, however, a strong influence of creep on these data. As shown inset – particularly in the 700 °C and 1000 °C curves – there is a significant amount of initial unloading due to (reverse) creep, before the measured displacement is only from thermal drift, analogous to the viscoelastic effects noted in the ASTM ISO14577-1 standard for nanoindentation [31].

The driving force for this reverse movement of the indenter is given by the confined material around the tip. The effect of stress-state is shown directly by a comparison of drift segments on CMSX-4 at 630 °C on a micropillar, i.e. without confining pressure driving reverse creep (for further experimental details, see [12], from where this data is taken and re-analysed), and away from the pillar using the same temperature settings and flat punch, producing a three-dimensional stress field similar to pyramidal indentation (Fig. 2(a)). Indents made using a Berkovich tip are shown, with the indenter at three different temperatures during tuning of the indentation contact, resulting in negative, zero and positive thermal drift rates. While a near-constant depth is maintained in the thermally stable pillar compression, the drift segment of the flat punch shows the same displacement out of the sample as observed in nanoindentation, before the depth reaches a near-constant value. The drift data from the Berkovich indentations demonstrate that this reverse movement is not due to thermal mismatch: it is present in all three drift segments before the true mismatch drift is measured in the system. This demonstrates the necessity of a 'stabilisation period' before drift rates are measured and drift corrections are applied. When measured over the last 40% of the indentation displacement–time data – the highlighted region of the insets in Fig. 1 – a thermal drift rate of −0.12 nm/s and +0.17 nm/s is measured at 700 °C and 1000 °C, respectively.

3.2. Mechanical data

The hardness-temperature behaviour of the sample is shown in Fig. 3(a). The hardness of the materials was measured at 4 GPa at room temperature, matching well with other nanoindentation tests [7]. This hardness is constant until 400 °C, before steadily falling to 0.5 GPa at 1000 °C. The indentation modulus as determined by an Oliver–Pharr fit [25] is shown in Fig. 3(b). There are small deviations from the literature values from acoustic resonance, the largest at 400 °C. However, nanoindentation elsewhere [7] measured near-identical values before the authors applied a creep correction. As little creep was measured here at these temperatures, we did not apply such a correction, and the data are overall consistent with the literature up to 700 °C. At 900 °C and 1000 °C the measured moduli are extremely low, due to an improper Oliver–Pharr fit to the unloading data, namely the assumption that the unloading is purely elastic, where in fact there is still significant time-dependent deformation occurring. The creep rates at these temperatures are extremely high (see Fig. 5) and this time-dependent deformation is still visibly present in the unloading data (Fig. 1(d)).

To confirm the validity of the mechanical data, a 3D cross-section of an indent made at 1000 °C was carried out using focussed ion beam milling to measure the residual indentation depth. Slices were cut at 20 nm intervals to ensure the deepest part of the indent could be accurately found, and the slice showing the deepest part is shown in Fig. 4 with a measured indent depth of 1.29 μm. Comparison with the hysteresis data from this indent (not shown in Fig. 1(d)) shows a final depth, after the creep hold period of 1.20 μm, thereby in good agreement. The backscattered electron (BSE) image shows the γ–γ' microstructure is largely undistorted, with the exception of the loss of some γ channels directly below the indent, but there is a small amount of contamination – likely aluminium oxide – above the indent.

3.3. Nanoindentation creep

The dwell period at the peak load was used to calculate the indentation strain rate $\dot{\epsilon}$ according to Eq. (1) [35], where h is indentation depth and t the time during the dwell period.

$$\dot{\epsilon} = \left(\frac{1}{h}\right)\left(\frac{dh}{dt}\right). \quad (1)$$

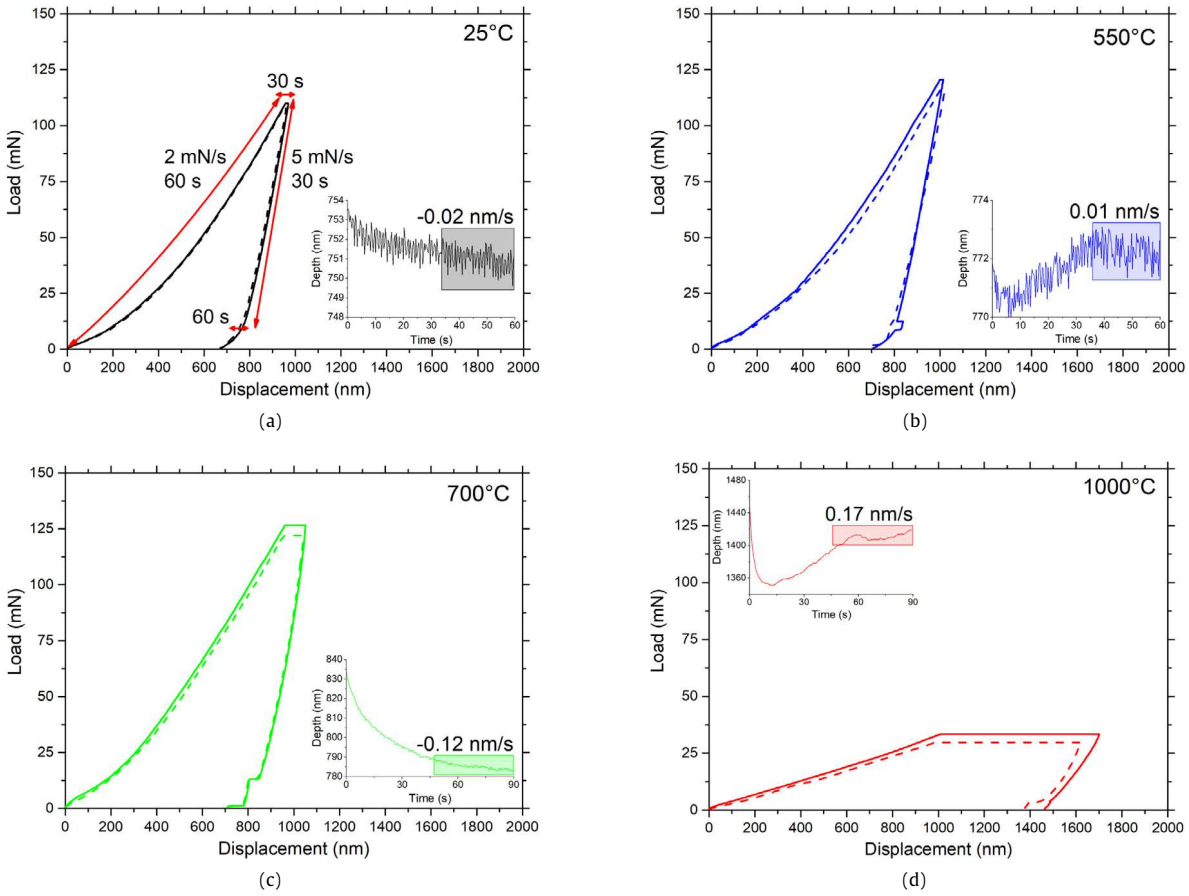

Fig. 1. An individual load–displacement data at 25 °C (a), 550 °C (b), 700 °C (c) and 1000 °C (d) from Amdry-386 and CMSX-4 (Amdry data shown dashed). For the data at 25 °C, the labels show the times for each indentation segment. (N.B. the rates were kept constant, so that the loading and unloading segments change accordingly, while the hold segments remain the same.) Inset: the drift hold segments, measured at 90% unload at the end of indentation. Note the significant change in Y axis at 700 °C (c) and above (d) due to the influence of creep on the unloading data. The measurement of thermal drift is carried out over the last 40% of the curve, highlighted. The significant, negative change in depth before this is the influence of creep.

The apparent stress exponent for creep, n, is given by Eq. (2) [36], where A is the uniaxial pre-exponential term.

$$\dot{\epsilon} = A\sigma^n. \tag{2}$$

The stress exponent was calculated using the indentation hardness in-lieu of the stress, as shown in Fig. 5. The indenter system used does not support a dynamic measurement of hardness throughout the hold period, therefore hardness was calculated simply as the peak load divided by the contact area from the diamond area function evaluated at the current depth to give Eq. (3), where H is the indentation hardness.

$$\dot{\epsilon} = A[H(h)]^n. \tag{3}$$

As the indents were performed under a constant loading rate, these hold periods begin at differing values of strain rate. As the hold period continues, the indentation depth increases and therefore the hardness and strain rate drops. The first data point of the curve, at the beginning of the hold period, is therefore the highest and furthest to the right.

4. Discussion

4.1. Hardness

The nanoindentation hardness of the single-crystal CMSX-4 can be compared with the yield stress of [001]-oriented CMSX-4 as well as single-crystal γ' (Ni_3Al) compression data in different crystal orientations. These data are indicated in Fig. 3 (literature data as lines for clarity, see supplemental material (Appendix A) for full data). The hardness plateau measured here is consistent with the yield stress of CMSX-4, apart from a small size effect due to nanoindentation, also seen by other authors [7]. The plateau, as opposed to the increasing yield stress seen in γ', is due to the precipitation strengthening present in CMSX-4.

The main discrepancy is the early drop in hardness: here after 400 °C but after 800 °C in the CMSX-4 yield stress and [001]-oriented compression data for Ni_3Al. To explain this, one must consider the different mechanisms and stress states during testing and the effect this has on the dislocation motion in the γ' precipitates. According to the theory of Paidar, Pope, and Vitek (PPV theory) [37], the shear stresses acting upon the primary (111) slip plane, the secondary $(1\bar{1}1)$ slip plane, and on the {100} cube planes all influence the anomalous yielding [38]. As a result, the peak stress is strongly dependent on crystallography. For alloys close to ⟨111⟩ under tension, the peak flow stress is seen around 400 °C [33], as shown in the supplementary material, Fig. A.9.

The strain underneath a Berkovich indenter extends in all directions [39], allowing multiple slip planes to be stressed, and many more slip systems to operate, than in a [100] compression test. Additionally, underneath the indenter, there exist high strains (taken commonly as a representative ∼8% strain [40]), which will lead to significant differences when comparing with bulk tension or compression tests that often use a 0.2% proof stress to indicate

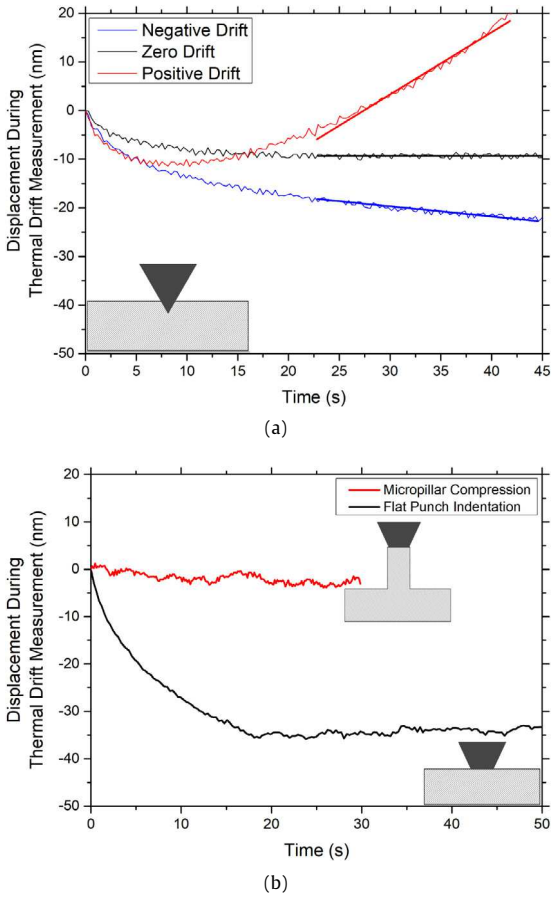

Fig. 2. (a) Three indents made into the sample (confining pressure) using a Berkovich tip during tuning at high temperature. (b) A comparison of the post-indentation thermal drift measurement for a micropillar (no confining pressure) and an indent made locally to the pillar at the same temperature (confining pressure). In all cases, the confining pressure drives reverse creep causing the initial rapid unloading, before a near-constant displacement rate is seen due to the thermal (in)stability. Note even when drift in the opposite direction is seen due to thermal mismatch between the tip and sample, this reverse creep remains. The micropillar data was collected as part of a previous publication [12] and re-analysed here.

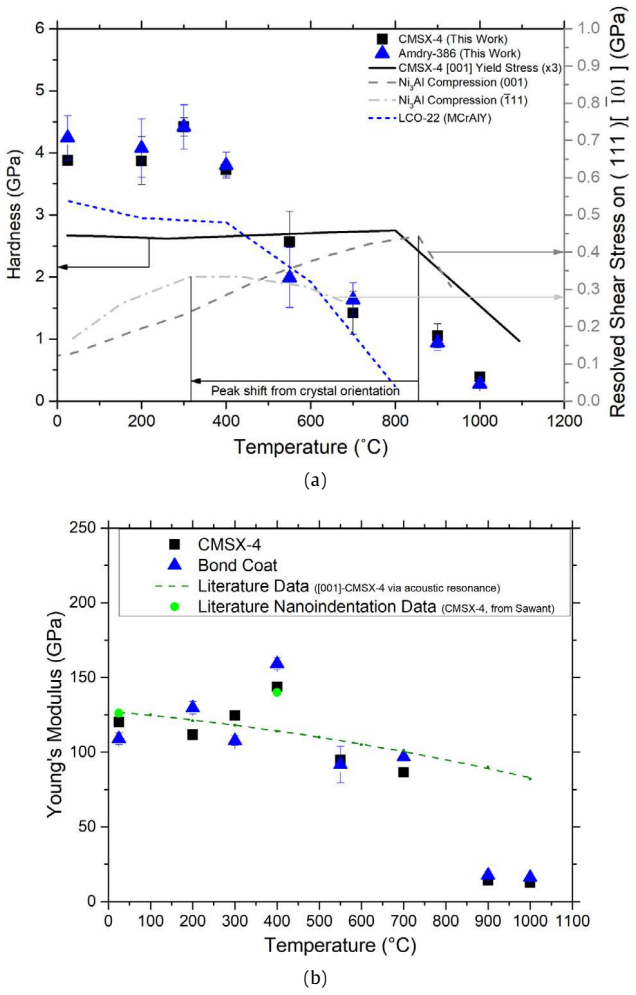

Fig. 3. (a) Hardness with temperature of CMSX-4 and Amdry-386. A constant hardness is seen up to 400 °C. The error bars given are one standard deviation of the scatter in hardness. A comparison of nanoindentation hardness with literature data is given: three times the yield stress of [001]-oriented CMSX-4 [32] and resolved shear stresses under compression of the 0.2% off-set yield stress of two single-crystal samples of Ni_3Al [33]. To compare with the Amdry-386, the conventionally-measured hardness of LCO-22 [34] is also shown. (b) Young's Modulus with temperature of CMSX-4 and Amdry-386. The error bars are one standard deviation of the scatter in modulus. The line shows the modulus of [001]-oriented CMSX-4 with temperature as found in the literature [26] and values of Young's modulus measured by nanoindentation [7]. Neither the data from this work nor the data from Sawant [7] have been corrected for creep.

yield. The strain-dependence of cross slip has been investigated by Hirsch [41], who showed that the strain rate in $L1_2$ alloys is given by Eq. (4), where $\dot{\varepsilon}$ is the strain rate, $\dot{\varepsilon}_0$ is the strain rate under zero applied stress, k the Boltzmann constant, T the temperature, and H_u and H_l are the activation enthalpies for unlocking and locking of macrokinks in the superdislocations.

$$\dot{\varepsilon} = \dot{\varepsilon}_0 \exp\left(-\frac{H_u - H_l}{kT}\right). \tag{4}$$

The enthalpy of unlocking is given by Eq. (5), where ${}^0H_u$ is the enthalpy with no applied stress, σ the applied stress and V^* the activation volume.

$$H_u = {}^0H_u - \sigma V^*. \tag{5}$$

These equations show – somewhat intuitively – that as the applied stress increases, dislocation motion becomes easier. The important consideration of this work is that it applies to cross-slipping superdislocations, thus explaining the observed, consistent decrease in hardness after the peak hardness at a lower temperature, as measured by nanoindentation.

To summarise: unlike uniaxial tensile data taken from yield stresses, there are high strains and a complex stress state underneath a Berkovich indenter, which in particular lead to a deviation from the zero resolved shear stress conditions on the 100 planes preventing cross-slip that occurs in uniaxial testing along $[001]\langle 001\rangle$. This therefore leads to indentation hardness measurements being strongly influenced by multiple slip systems, and cross-slip occurring in γ' at lower temperatures which accounts for the observed drop-off in hardness. Indentation, whether at room or extreme temperatures, of the single crystal superalloy (or in fact any other strongly anisotropic material) is therefore limited in value with regards to transferability to applications where a near-uniaxial stress in a fixed direction is encountered, such as in high pressure turbine blades. However, the data presented here show that the methods employed nevertheless show good agreement with the extensive literature data available on CMSX-4.

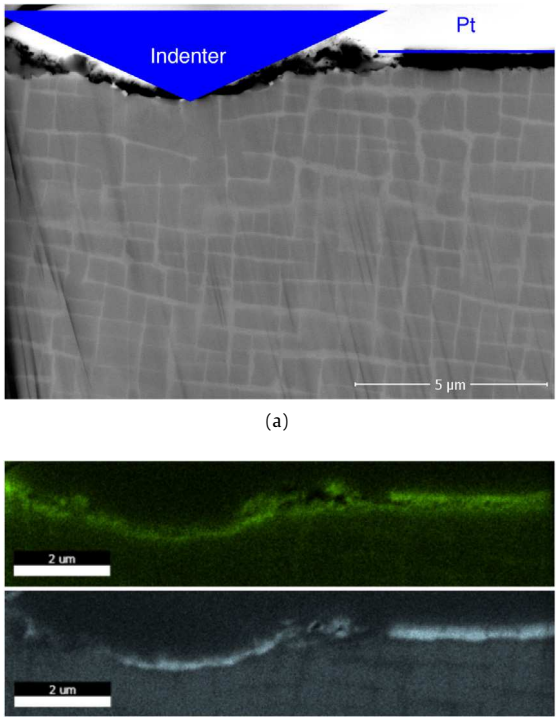

Fig. 4. (a) BSE image taken at 30°during 3D cross-sectioning of an indent made at 1000 °C. The $\gamma - \gamma'$ microstructure is largely undistorted, with the exception of the loss of some γ channels directly below the indent. (b) Oxygen (green) and aluminium (light blue) signals from an EDX map, suggesting the dark contrast in the BSE image is aluminium oxide contamination, likely from the high-temperature cements used for tip and sample fixing that formed during indentation above 700 °C. (For interpretation of the references to colour in this figure legend, the reader is referred to the web version of this article.)

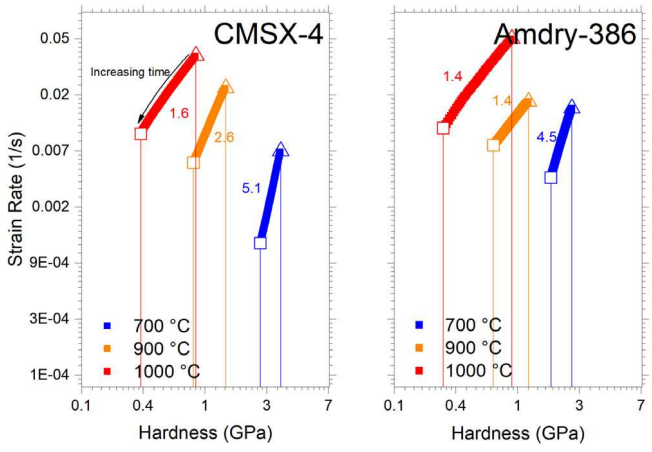

Fig. 5. Natural log of hardness against natural log of strain rate. The gradient at each temperature, i.e. the creep exponent, is shown. Open triangles mark the hardness at the start of the creep hold period and open squares the hardness at the end of the hold period, calculated using the instantaneous depth.

Due to its random texture and small grain size, indentation on MCrAlY bond coats will be directly relevant for material performance in application. Although the bond coat may not carry the full centrifugal forces encountered in the blade, it is essential to the adherence of the thermal barrier coating and also used to hold abrasive particles where a shroud-design is to be avoided at the blade tip in modern engine designs. It has been shown that mechanical performance at operating temperatures is vital to retain the abrasive during operation [42,43]. Some of the scarce literature data for MCrAlY bond coats are shown in Fig. 3, with more detail again given in the supplementary material (see Appendix A). The hot hardness of LCO-22 (an CoNiCrAlY alloy) also shows a similar trend to the indentation data, with the hardness dropping quickly after 400 °C.

The modulus data from the two samples are also shown in Fig. 3, along with literature data for the [001]-direction from acoustic resonance measurements on CMSX-4. The data obtained here matches that of the nanoindentation data by Sawant and Tin [7] very closely, when their 'creep correction' has not been applied. Overall, the data match closely where creep deformation is not overly significant, namely below 700 °C. Despite the aforementioned effects of indenter stress state, in CMSX-4 one would expect only a 10% difference between the reduced modulus of polycrystalline and [001]-single crystalline [44] samples. As the bond coat is intrinsically similar in composition, it is reasonable to find approximately the same modulus as the CMSX-4.

As previously mentioned, it is not possible to obtain reliable values of modulus from data at 900 °C and 1000 °C, where the rates of creep are significant. The hysteresis curves show significant curvature in the unloading segment, and therefore the Oliver–Pharr method is invalid. In order to obtain reliable modulus values from indentation in the case where creep is significant, the generally recommended practice [31,45] is to increase the hold segment and choose the highest possible unloading rate yielding sufficient data points for the analysis. ISO 14577-1 recommends an unloading rate ten times greater than the ratio of the contact creep rate and contact compliance at maximum load. The latter may be estimated from the reduced modulus of the material from literature data (see Fig. 3) and the diamond area function of the tip.

Considering the creep rates found here at the three highest temperatures, namely 1 nm/s at 700 °C, 13.5 nm/s at 900 °C and 16 nm/s at 1000 °C, target unloading rates of 19, 275 and 335 mN/s are necessary to measure the modulus. The values exceeding 100 mN are not reliably accessible in practice due to the inertia and data acquisition rate of conventional nanoindenters. Additionally, at 900 °C and 1000 °C the peak dwell segments contain no indication of the required reduction in creep rate, and dwell periods of several minutes or more might be required to achieve creep rates at which a measurement of the modulus may be feasible. Given that at high temperatures not only the accuracy of the displacement signal at long times but also sample-tip reactions are an issue, even where efficiency of the method or microstructural changes in the material need not be considered, it appears that measurement of the modulus of materials with similar creep behaviour or chemical reactivity is out of reach of nanoindentation at extreme temperatures, at least where the conventional unloading analysis is applied. Of course, a continuous stiffness measurement may improve the situation, however, this is not available for the indenter system used here.

These results therefore demonstrate an important consideration for high-temperature nanoindentation: that a single indentation test cannot reliably determine all the standard parameters, namely hardness, elastic modulus and creep resistance. These indents capture hardness and creep resistance, albeit a slightly lower hardness due to the creep hold period. However, at the highest temperatures and creep rates they are unable to capture accurate values of elastic modulus and whether measurements are likely to be successful using nanoindentation under these conditions requires careful consideration of the available methods of analysis, acquisition and unloading rates, quality of the thermal equilibrium and possible contact times between tip and sample on a case-to-case basis.

4.2. Creep

During the analysis of the creep data, the indentation depth was simply taken 'as-is', once the hysteresis data had been corrected for thermal drift based upon the post-test thermal drift measurement. As the indent time was relatively short, the effects of thermal drift on the data are minimal and novel depth corrections used in long-term creep tests using continuous stiffness measurement [46] should not be required. Where creep is most significant (at 700 °C, 900 °C and 1000 °C) the determined exponents are compared with the literature in Fig. 6.

A log–log plot of strain rate and hardness used to calculate the creep exponent in CMSX-4 and Amdry-386 is shown in Fig. 5. The 1000 °C curves can be seen to have a slight curvature. Kang [60] attributes a 'concave' curve like this in an Mg–Sn alloy to be due to grain boundary sliding behaviour, with a 'convex' curve being a result of grain matrix deformation. Similar curvatures to Kang are seen in indentation creep experiments by Mathur [61] in the $Mg_{17}Al_{12}$ phase and Maier [46] in ufg-Au. Grain boundary sliding cannot be taking place in a single crystal of CMSX-4, unless significant dynamic recrystallisation is taking place. Therefore, the question is as to whether this is an effect from the sample, or one from nanoindentation. In CMSX-4, the amount of primary creep, accommodated by $\langle 11\bar{2}\rangle$ {111} slip, increases with increasing stress [62]. Secondary creep then proceeds, at a time that decreases as the applied stress increases [62]. Given the high stresses present, it is therefore possible that this curvature is the start of the transition to secondary creep, with the associated decrease in creep strain rate. Microstructural characterisation using TEM is needed to take place in order to confirm this. However, the curvature could simply be an artefact of the indenter velocity during rapid creep, as recent modelling results have shown [63].

Fig. 6 shows the creep stress exponents as determined by nanoindentation testing compared with values found in the literature. Apart from the data from Carry [52], the values of stress exponent determined by nanoindentation in CMSX-4 are different to those found in the literature; a common problem in nanoindentation creep [64]. These differences are often attributed to the high, changing stresses during nanoindentation creep and significant degree of primary creep. Additionally in this work, similar orientation issues to the hardness data are present: the literature is mostly concerned with [100]-oriented single crystals in tension, rather than the complex stress states present here. This may go some way to explaining the significant differences seen.

Mitchell [47] shows that in materials such as Ni_3Al with a high Peierls barrier, the apparent activation energy is strongly dependent on temperature, also seen here. Despite the aforementioned problems with the value of creep exponent, the rate of change in exponent with temperature measured by Mitchell [47] and Glock [48] in tension is the same as measured by indentation at 700 °C and above. This indicates that the nanoindentation creep is determined by the same processes as traditional creep experiments, namely double-kink nucleation to allow glide of $\langle 110\rangle$ dislocations.

In the bond coat, the indentation exponents match very closely to those measured by tensile testing. It is not fully clear why the punch-test by Chen [59] produces significantly higher values of creep exponent, given the bond coats from Wereszczak [57] have the same composition (Co-32Ni-21Cr-8Al-0.5Y), but is likely due to the extremely complicated stress fields present in such a test. Hebsur [55] states that creep in the bond coat is likely a mixture of dislocation climb ($n > 5$) and viscous flow ($n = 3$), and therefore it is possible that similar creep mechanisms are occurring under both macro-scale creep tests and nanoindentation. More investigation is clearly required, but it is an encouraging first result.

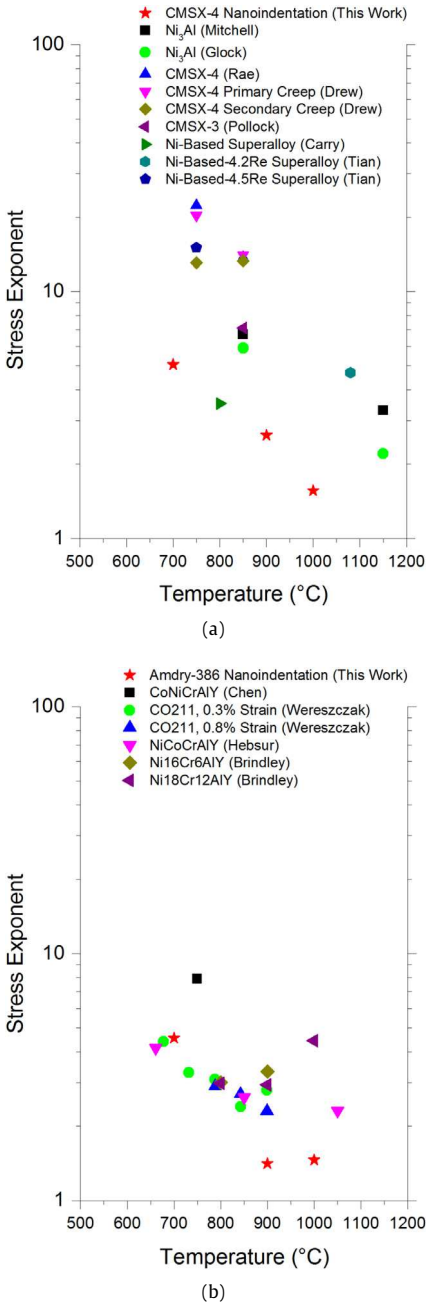

Fig. 6. (a) A comparison of the stress exponents in CMSX-4 determined by nanoindentation and those found in the work of Mitchell [47], Glock [48], Rae [49], Drew [50], Pollock [51], Carry [52], and Tian [53,54]. (b) Amdry-386 exponents are compared with the work of Hebsur [55,56], Wereszczak [57] (Stress relaxation under tension), Brindley [58] (Stress relaxation under tension), and Chen [59] (Punch). All tests were macroscopic tensile tests, unless otherwise stated.

5. Conclusions

A CMSX-4 superalloy and its Amdry-386 bond coat were tested up to 1000 °C by nanoindentation. The hardness is seen to drop steadily past 400 °C, compared with a hardness peak at 800 °C as seen in single-crystal tensile tests. This differing behaviour is likely due to the complex stress field underneath a Berkovich indenter. In contrast, the hardness behaviour of the Amdry-386 is comparable to the limited literature data on other MCrAlY bond coats. The stress exponents associated with indentation creep have

also been determined from the hold segments during nanoindentation. While the CMSX-4 exponents are somewhat different – again likely due to large, complex stress fields under the indenter – those determined in the bond coat match other MCrAlY coefficients closely.

Further work such as TEM analysis is required to examine the mechanisms of creep and deformation in the bond coat in order to determine the applicability of these data to in-service conditions. However, this work clearly demonstrates that relative comparisons of both hardness and creep resistance are able to be made on these thin layers at operationally relevant temperatures. The work thus shows that high temperature nanoindentation is well suited for future investigations of these MCrAlY coatings, in emerging new applications such as turbine sealing using abrasives [42] or blade repair [43].

Regarding high-temperature nanoindentation, these results demonstrate the difficulty of a 'one-size-fits all' approach, particular due to the influence of creep on the drift correction and modulus data. Tailored, rapid indents with no, or minimal, hold periods are ideal for the measurement of hardness, while modulus and creep information requires the use of much longer indentation time scales where possible. Finally, single crystals with strong anisotropies, such as the nickel superalloy investigated here, will show significant deviations from macroscopic investigations due to the indenter stress field and the materials to be investigated within the field of high temperature applications should therefore be selected carefully.

Acknowledgements

The authors would like to thank R. Vaßen, FZJ, Germany for supplying the materials, and A. Ziemons and T. Burlet of the IMM for technical assistance. This work was supported by the Deutsche Forschungsgemeinschaft (DFG) within project KO4603/2-1.

Conflict of interest

The authors declare that they have no conflict of interest.

Appendix A. Supplementary data

Supplementary material related to this article can be found online at https://doi.org/10.1016/j.eml.2017.09.007.

References

[1] A. Saini, T. Pollock, MRS Bull. 37 (2012) 550.
[2] B. Bhushan, X. Li, Int. Mater. Rev. 48 (2003) 125.
[3] S.J. Bull, J. Phys. D: Appl. Phys. 38 (2005) R393.
[4] D. Kiener, et al., J. Mater. Res. 27 (2012) 2724.
[5] D.E.J. Armstrong, P.D. Edmondson, S.G. Roberts, Appl. Phys. Lett. 102 (2013).
[6] B. Beake, J. Smith, Phil. Mag. A 82 (2002) 2179.
[7] A. Sawant, S. Tin, Scr. Mater. 58 (2008) 275.
[8] J.C. Trenkle, C.E. Packard, C.A. Schuh, Rev. Sci. Instrum. 81 (2010).
[9] N.M. Everitt, M.I. Davies, J.F. Smith, Phil. Mag. 91 (2011) 1221.
[10] D.E.J. Armstrong, E. Tarleton, JOM (2015).
[11] J.M. Wheeler, D.E.J. Armstrong, W. Heinz, R. Schwaiger, Curr. Opin. Solid State Mater. Sci. 19 (2015) 354.
[12] S. Korte, R.J. Stearn, J.M. Wheeler, W.J. Clegg, J. Mater. Res. 27 (2012) 167.
[13] U. Hangen, C.L. Chen, A. Richter, Adv. Energy Mater. 17 (2015) 1683.
[14] Z.J. Huang, A. Harris, S.A. Maloy, P. Hosemann, J. Nucl. Mater. 451 (2014) 162.
[15] J.S.K.L. Gibson, S.G. Roberts, D.E.J. Armstrong, Mater. Sci. Eng. A 625 (2015) 380.
[16] A.J. Harris, B.D. Beake, D.E.J. Armstrong, M.I. Davies, Exp. Mech. (2016) 1–12.
[17] X. Li, B. Bhushan, Mater. Charact. 48 (2002) 11.
[18] K. Durst, A. Goken, Mater. Sci. Eng. A 387 (2004) 312.
[19] H.U. Rehman, et al., Mater. Sci. Eng. A 634 (2015) 202.
[20] N. Zotov, M. Bartsch, G. Eggeler, Surf. Coat. Technol. 203 (2009) 2064.
[21] S. Saeidi, K.T. Voisey, D.G. McCartney, J. Therm. Spray Technol. 20 (2011) 1231.
[22] G.D. Girolamo, et al., J. Mater. Eng. Perform. 21 (2012) 1989.
[23] P.J. Terberger, et al., Surf. Coat. Technol. 276 (2015) 360.
[24] Y. Li, et al., Mater. Sci. Eng. A 678 (2016) 65.
[25] W. Oliver, G. Pharr, J. Mater. Res. 7 (1992) 1564.
[26] D. Siebörger, H. Knake, U. Glatzel, Mater. Sci. Eng. A 298 (2001) 26.
[27] N. Soga, O.L. Anderson, J. Am. Ceram. Soc. 49 (1966) 355.
[28] J.B. Wachtman, D.G. Lam, J. Am. Ceram. Soc. 42 (1959) 254.
[29] J. Chen, S.J. Bull, Surf. Coat. Technol. 201 (2006) 4289.
[30] W.S. Rathod, A.S. Khanna, J. Karthikeyan, R.C. Rathod, Surf. Eng. 30 (2014) 432.
[31] ISO/TC 164/SC 3 Hardness testing, ISO 14577-1:2015, ASTM, ASTM, 2015.
[32] A. Sengupta, et al., J. Mater. Eng. Perform. 3 (1994) 73.
[33] S.S. Ezz, D.P. Pope, V. Paidar, Acta Metall. 30 (1982) 921.
[34] T.A. Taylor, D.F. Bettridge, Surf. Coat. Technol. 86–87, Part 1 (1996) 9.
[35] B.N. Lucas, W.C. Oliver, Metall. Mater. Trans. A 30 (1999) 601.
[36] P.S. Phani, W.C. Oliver, Acta Mater. 111 (2016) 31.
[37] V. Paidar, D.P. Pope, V. Vitek, Acta Metall. 32 (1984) 435.
[38] V. Vitek, D.P. Pope, J.L. Bassani, Chapter 51 Anomalous yield behaviour of compounds with $L1_2$ structure, vol. 10, Elsevier, 1996, pp. 135–185.
[39] L. Min, C. Wei-Min, L. Nai-Gang, W. Ling-Dong, J. Mater. Res. 19 (2004) 73.
[40] A.C. Fischer-Cripps, Nanoindentation (2011).
[41] P. Hirsch, Phil. Mag. A 65 (1992) 569.
[42] J. Davenport, et al., Mater. Sci. Technol. 30 (2014) 1877.
[43] C. Hardwicke, Y.C. Lau, J. Therm. Spray Technol. 22 (2013) 564.
[44] J.J. Vlassak, W.D. Nix, Phil. Mag. A 67 (1993) 1045.
[45] T. Chudoba, F. Richter, Surf. Coat. Technol. 148 (2001) 191.
[46] V. Maier, A. Leitner, R. Pippan, D. Kiener, JOM (2015).
[47] T. Mitchell, J. Hirth, A. Misra, Acta Mater. 50 (2002) 1087.
[48] K. Glock, C. Knobloch, U. Glatzel, Metall. Mater. Trans. A 31 (2000) 1733.
[49] C.M.F. Rae, R.C. Reed, Acta Mater. 55 (2007) 1067.
[50] G.L. Drew, R.C. Reed, K. Kakehi, C.M.F. Rae, Proceedings of the International Symposium on Superalloys, pp. 127–136.
[51] T.M. Pollock, A.S. Argon, Acta Metall. Mater. 40 (1992) 1.
[52] C. Carry, J. Strudel, Acta Metall. 25 (1977) 767. Cited by 90.
[53] S. Tian, Z. Zeng, L. Fushun, C. Zhang, C. Liu, Mater. Sci. Eng. A 543 (2012) 104.
[54] S. Tian, et al., Mater. Des. 37 (2012) 236.
[55] M.G. Hebsur, R.V. Miner, Mater. Sci. Eng. 83 (1986) 239.
[56] M.G. Hebsur, R.V. Miner, Thin Solid Films 147 (1987) 143.
[57] A.A. Wereszczak, et al., American Society of Mechanical Engineers (Paper).
[58] W.J. Brindley, J.D. Whittenberger, Mater. Sci. Eng. A 163 (1993) 33.
[59] H. Chen, T.H. Hyde, K.T. Voisey, D.G. McCartney, Mater. Sci. Eng. A 585 (2013) 205.
[60] D. Kang, S. Park, Y.S. Oh, N.J. Kim, Mater. Sci. Eng. A 449–451 (2007) 318. Proceedings of the 12th International Conference on Rapidly Quenched & Metastable Materials.
[61] H.N. Mathur, V. Maier-Kiener, S. Korte-Kerzel, Acta Mater. 113 (2016) 221.
[62] R. Reed, The superalloys fundamentals and applications, 2006.
[63] J. Campbell, J. Dean, T.W. Clyne, Mech. Time-Depend. Mater. (2016) 1–13.
[64] R. Goodall, T. Clyne, Acta Mater. 54 (2006) 5489.

Further reading

[1] H. Waki, T. Kitamura, A. Kobayashi, J. Therm. Spray Technol. 18 (2009) 500.

Plastic deformation of the CaMg 2 C14-Laves phase from 50 - 250°C

Martina Freund, Doreen Andre, Christoffer Zehnder, Hanno Rempel, Dennis Gerber, Muhammad Zubair, Stefanie Sandlöbes-Haut, James S. K.-L. Gibson, Sandra Korte-Kerzel,

Materialia, Volume 20, 2021, 101237
https://doi.org/10.1016/j.mtla.2021.101237.

Short Summary

Intermetallic phases can significantly improve the creep resistance of magnesium alloys, extending their use to higher temperatures. However, little is known about the deformation behaviour of these phases at application temperatures, which are commonly below their macroscopic brittle-to-ductile-transition temperature. In this study, we therefore investigate the activation of different slip systems of the $CaMg_2$ phase and the occurrence of serrated yielding in the temperature range from 50°C to 250°C. A decreasing amount of serrated flow with increasing temperature suggests that solute atoms govern the flow behaviour when the $CaMg_2$ phase is off-stoichiometric.

The authors contribution to this paper comprised conceptualization, methodology of the experimental work, investigating and analyzing the experimental data as well as writing a first draft.

Materialia 20 (2021) 101237

Contents lists available at ScienceDirect

Materialia

journal homepage: www.elsevier.com/locate/mtla

Full Length Article

Plastic deformation of the $CaMg_2$ C14-Laves phase from 50 - 250°C

Martina Freund[a,*], Doreen Andre[a], Christoffer Zehnder[a], Hanno Rempel[a], Dennis Gerber[a], Muhammad Zubair[a,b], Stefanie Sandlöbes-Haut[a], James S. K.-L. Gibson[a], Sandra Korte-Kerzel[a]

[a] Institute for Physical Metallurgy and Materials Physics, RWTH Aachen University, Aachen, Germany
[b] Department of Metallurgical and Materials Engineering, UET, Lahore, Pakistan

ARTICLE INFO

Keywords:
Plasticity
Laves phase
Temperature
Stoichiometry
Nanoindentation
Microcompression

ABSTRACT

Intermetallic phases can significantly improve the creep resistance of magnesium alloys, extending their use to higher temperatures. However, little is known about the deformation behaviour of these phases at application temperatures, which are commonly below their macroscopic brittle-to-ductile-transition temperature. In this study, we therefore investigate the activation of different slip systems of the $CaMg_2$ phase and the occurrence of serrated yielding in the temperature range from 50°C to 250°C. A decreasing amount of serrated flow with increasing temperature suggests that solute atoms govern the flow behaviour when the $CaMg_2$ phase is off-stoichiometric.

1. Introduction

1.1. Application of $CaMg_2$ Laves phases

Magnesium, as the lightest structural metal, has great potential for light-weight applications, but the use of its alloys in applications above 100°C is limited due to their low creep resistance. Recently-developed alloys containing aluminium and calcium exhibit minimum creep rates up to three orders of magnitude lower than pure magnesium [1–10]. This improved creep resistance is due to the formation of an interconnected network of intermetallic phases [7-9,11-13]. This network reduces creep taking place via grain boundary sliding or other diffusion-dominated creep mechanisms along grain boundaries. However, once this network begins to crack, the creep rates significantly increase [14,15]. Consequently, there is a need to understand the mechanical response and plasticity mechanisms of the intermetallic phases to predict deformation and creep-related failure in these Mg-Al-Ca alloys from room- to application-temperatures and to pursue purposeful alloy design.

In Mg-Al-Ca alloys, several intermetallic phases form [10,16-20], including two hexagonal Laves phases C14 $CaMg_2$ and C36 $Ca(Mg,Al)_2$, the cubic C15 $CaAl_2$, the β-Mg_2Al_3 Laves phase and $Mg_{17}Al_{12}$ precipitates with a complex body-centred cubic structure (α-Mn type). The $Mg_{17}Al_{12}$ phase exhibits a significant hardness drop once temperatures reach 150°C [21]. Hence, it is assumed that for Mg-Al-Ca alloys with favourable high-temperature behaviour, the $Mg_{17}Al_{12}$ phase should be avoided, which can be realised by increasing the Ca content [15]. The mechanical properties of the Mg-Al-Ca alloy at high temperature will subsequently be determined by the deformation of the α-Mg matrix and the Laves phases.

1.2. Deformation mechanisms of Laves phases

Reports on macroscopic low-temperature deformation behaviour of the $Ca(Mg_x,Al_{1-x})_2$ and most other Laves phases are sorely lacking, with a solitary publication by Kirsten et al. [22] who reported slip on $\{01\bar{1}0\}\langle 2\bar{1}\bar{1}0\rangle$ at ambient temperature after their Brinell hardness tests on the $CaMg_2$ phase. However, extensive studies on the high temperature (HT) mechanical properties of Laves phases have been conducted by Paufler, Schulze, Kubsch and others [23–34]. Specifically, they have conducted compression and creep tests at high homologous temperatures, T_H, mainly on C14 $MgZn_2$ single crystals. Generally, these studies have shown that it is not possible to induce bulk plastic flow in macroscopic specimens at homologous temperatures lower than approximately $T_H = 0.6$. For lower temperatures, plastic deformation can only be introduced locally in Laves phases, such as in indentation or using micropillar compression [22,29,35,36]. As an example, a recent nanoindentation study by Lou et al. [37] analysed the influence of the orientation on the hardness of the C14 $NbCo_2$ phase. It was found that the hardness was about 5% higher for an orientation close to (0001) compared to the other investigated orientations.

For a long time, hardness tests were the only available method allowing the determination of the mechanical properties of Laves phases over a large range of temperatures. Kirsten et al. [22] conducted hardness tests on the $MgZn_2$ and the $CaMg_2$ C14 Laves phases and revealed a de-

* Corresponding author.
E-mail address: freund@imm.rwth-aachen.de (M. Freund).

https://doi.org/10.1016/j.mtla.2021.101237
Received 15 June 2021; Accepted 25 September 2021
Available online 30 September 2021

creasing hardness of approximately 10% up to a transition temperature, after which a pronounced loss in hardness was observed. This transition temperature was 0.59*T_m (T_m being the melting temperature) for the $CaMg_2$ phase also investigated within this study and 0.61*T_m for the $MgZn_2$ phase. Correspondingly, this trend was also found for the yield strength in dynamic compression tests on the $MgZn_2$ phase [28].

Regarding deformation mechanisms above the transition temperature, Paufler et al. [29] postulated a deformation regime at low stresses and high temperatures ($T > 0.7\ T_m$) where dislocation climb is thought to be active. However, Kubsch et al. [32] did not observe this in their experiments. Furthermore, Paufler et al. [26,27,31] showed that the dislocation velocity on basal and prismatic slip planes is exponentially dependent on the applied stress at conditions of constant temperature and stress (e.g. during creep) in Laves phases. From these findings, the authors concluded that a thermally activated Peierls mechanism is the limiting factor for dislocation motion at high temperatures [26,27,31]. It has also been observed that the critical stresses for dislocation motion associated with the lattice resistance (thermally activated flow over the Peierls barrier) for basal and prismatic slip are of the same order of magnitude at high temperatures [27]. Furthermore, a significant amount of thermally activated cross-slip has been found between 250°C and 500°C [31]. Most dislocations present after high temperature deformation were observed to be on the basal or the prismatic planes [31], however, it should be noted that the single crystals tested were purposely aligned for the activation of these slip systems. Recent atomistic simulations by Guénolé et al. [38] have shown that the propagation mechanism for dislocations on the basal plane is a synchroshear mechanism, rather than conventional dislocation glide.

Though experiments at several temperatures have revealed that $\langle a \rangle$-type dislocations on basal planes are the most frequently observed dislocation type [25,31,39-41], several studies have shown that non-basal slip systems can also be activated in Laves phases [39,42-45]. It has further been reported that slip planes normal to the basal plane can be activated when Laves phase containing alloys are deformed at elevated temperatures [46]. A publication by Paufler et al. [47] further listed the observed slip systems of several intermetallic phases at different temperature ranges. For $MgZn_2$, which has the same crystal structure (C14) as that of the $CaMg_2$ investigated here, basal slip was reported to occur for temperatures between 250°C and 550°C, whereas at temperatures of 500°C and above, prismatic and pyramidal slip were reported. Furthermore, uniaxial compression experiments by Paufler et al. [48] on nearly (0001) oriented $MgZn_2$ single crystals at 450°C revealed mechanical twinning as an additional deformation mechanism. Studies by Kazantzis et al. [49–51] on the deformation behaviour of the C15 $NbCr_2$ phase confirm the deformation via slip and twinning at elevated temperatures, which is assumed to be due to a low stacking fault energy.

In addition to these effects of crystal orientation and temperature, the stoichiometry – or rather the off-stoichiometry, i.e. the deviation from the exact stoichiometry – also has a significant effect on the deformation mechanisms and the mechanical properties of Laves phases. It has been seen that with increasing off-stoichiometry, deformation becomes less uniform in Laves phases and Lüders bands begin to form during plastic deformation [28,30-33,52]. Furthermore, several publications by Luo et al. [36,37,53] who studied the composition dependence of the mechanical properties of C14 and C36 $NbCo_2$, as well as C15 $NbCo_2$ Laves phases, revealed an effect of the composition on the critical resolved shear stress (CRSS), elastic modulus and hardness, but no effect on the fracture toughness. These effects were explained by a reduced shear modulus, stacking fault energy and Peierls stress, respectively. More information regarding the fundamental aspect of Laves phases can be found in a recent review by Stein et al. [54].

Kubsch et al. [31] reported a strong effect of the stoichiometry on the deformation mechanisms, reporting in $MgZn_2$ that slight deviations (±2 at.-%) from the stoichiometric composition cause a significant decrease of the dislocation velocity, particularly on the Mg-rich side. In intermetallic structures, off-stoichiometry can induce pinning points for dislocations, thus hindering the motion of dislocation kinks and therefore reducing the velocity of dislocations [26,31]. This is considered in the model proposed by Celli et al. [32] where the rate-controlling mechanism of plastic deformation is proposed to be the nucleation of double kinks and their lateral movement across pinning points [32]. A similar mechanism is reported by Kazantzis et al. [55] regarding the self-pinning nature of synchro-Shockleys in the C15 Laves phase at elevated temperatures.

Similar effects on the dislocation velocity have been reported elsewhere [28,30-33,52], implying that especially for the exact stoichiometric composition, dislocation starvation is a limiting factor at the beginning of deformation. Subsequently, dislocations are then able to travel large distances without being pinned [28,33]. This is in good agreement with micropillar compression experiments by Takata et al. [35,42] who found that the critical stress required to activate shear deformation in Fe_2Nb micropillars was drastically reduced when the pillars were slightly pre-deformed with a Berkovich indenter prior to compression, indicating that dislocation nucleation is a critical factor for plastic deformation of Laves phases [35,42]. In metals, this effect can also be observed, but only in samples that have been prepared to achieve a low dislocation density by solidification, annealing and avoidance of damage from the focussed ion beam (FIB) [56,57]. None of these special conditions have been applied in our work. It has been further reported that temperature does not affect the mean distance that dislocations travel before being pinned, but that the number of activated dislocation sources is instead increased with increasing temperature [28]. Finally, it has been shown that if several Laves phases are present in one system at the same temperature, the C15 phase can typically be found at the exact stoichiometric composition while the C14 and the C36 phase both tend to crystallise with an off-stoichiometric composition [58].

A previous study by the authors [59] elucidated the critical resolved shear stresses of different slip systems in the C14 $CaMg_2$ Laves phase at room temperature. The critical resolved shear stresses obtained for slip on these planes in microcompression follow the sequence: 1st order prismatic planes (0.44 GPa) < basal (0.52 GPa) and 1st order pyramidal (0.53 GPa) planes < 2nd order pyramidal planes (0.59 GPa) < 2nd order prismatic planes, for which no critical stress could be measured directly [59]. The authors further identified the presence of both $\langle a \rangle$ and $\langle c + a \rangle$-dislocations on the 1st order pyramidal planes by transmission electron microscopy of lamellae extracted from under nanoindents [59].

The aim of the present study is to extend these investigations and to study the activation and critical resolved shear stresses of slip systems in the $CaMg_2$ Laves phase at intermediate elevated temperatures where plastic deformation still cannot be achieved macroscopically. Hence, we aim to close the gap between deformation at room temperature and high temperatures. To this end, elevated temperature nanoindentation and micropillar compression between 50°C and 250°C (< 0.53 T_m) were performed in conjunction with microstructure characterisation using scanning electron microscopy (SEM), electron backscatter diffraction (EBSD) and transmission electron microscopy (TEM).

2. Experimental methods

As-cast samples of the $CaMg_2$ (C14) phase prepared from a pre-alloy were mechanically ground and polished with diamond paste down to 0.25 μm, followed by a final polishing step with 0.05 μm aluminium oxide polishing solution (OPA). EBSD (Hicari, EDAX (NJ, USA)) was used to determine the crystal orientations. Three grains with angles of 48°, 83° and 9° between the (0001) plane normal and normal direction (ND) were selected for micromechanical testing (Fig. 1). EDX measurements were performed on all three areas of interest. The mean Mg-content was measured as 68.7 ± 0.5 at.-% which is a deviation of approximately 2 at.-% from the exact stoichiometric composition. A wet-chemical analysis of the pre-alloy revealed an impurity content of <0.32 wt.-% with aluminium the major impurity element (0.24 wt.-%).

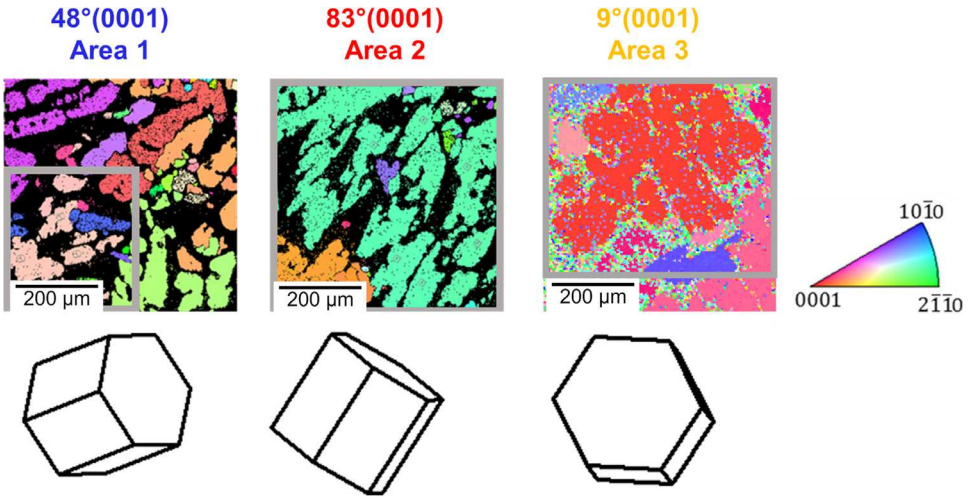

Fig. 1. EBSD maps of the three grain orientations with position of the investigated areas marked by grey rectangles. Their unit cell orientation viewed from the normal direction is also given.

2.1. Nanoindentation

Indentation experiments were performed between 50°C and 250°C in 50°C steps in the three crystal orientations resulting in a total of 80 indents using an in-situ SEM nanoindenter (InSEM-III, Nanomechanics Inc, TN, USA / Tescan Vega-3, TESCAN Brno, Czech Republic) using continuous stiffness measurements. A diamond Berkovich indenter tip (supplied by Synton MDP, Switzerland) was used, which was calibrated prior to indentation at room temperature on fused silica [60]. All indentation tests were performed at a constant strain rate of approximately 0.04 s^{-1} up to a maximum load of 20 mN or a maximum depth of 600 nm. Furthermore, for better visibility of potential slip traces, indents up to a maximum load of 1000 nm were performed using a loading rate of 0.2 s^{-1}. The thermal drift rate was below 0.4 nm/s for all measurements. The resulting data were then further evaluated according to the method published by Oliver and Pharr [60]. After indentation, secondary electron (SE) images of the indents were recorded by SEM (Helios Nanolab 600i, FEI, Eindhoven, NL) and the surface slip lines around the indents were compared to the plane traces of different slip planes obtained from the EBSD maps; a full description of this procedure is given elsewhere [61,62]. This approach gives the relative frequency of slip plane-surface intersections for the crystal orientations selected experimentally and, hence, elucidates the activation frequency of different slip planes. TEM investigations were conducted at 200 kV (Philips CM20) on lamellae taken from indents performed at 250°C in the 48°(0001) and the 83°(0001) orientations. The lamellae were cut using a focused ion beam.

2.2. Micropillar compression experiments

Micropillars were manufactured in all three grains using a focused ion beam (FIB) (FEI Helios Nanolab 600i, FEI, Eindhoven, NL) at a voltage of 30 kV and currents between 21 nA and 80 pA. The micropillars with a circular cross section had an average aspect ratio (height : top diameter) of 2.8 and were compressed 'in-situ' inside an SEM, using a diamond flat punch at a constant loading rate of 0.9 mN/s at temperatures of 150°C and 250°C. The thermal drift was below 0.4 nm/s for all measurements. After successful compression of 17 micropillars, they were imaged at 45° in a SEM (FEI Helios Nanolab 600i, FEI, Eindhoven, NL) and the angles of the slip events were measured, corrected for the stage tilt, and compared to the intersections of crystal planes with the pillar surface using Matlab® in order to assign them to possible slip planes [62]. It was further assumed that slip in the direction of the highest Schmid factor was activated. The resulting slip direction was then further verified with the post compression SE-images. Finally, the original upper diameter of the pillar was used to calculate the critical resolved shear stress (CRSS).

3. Results

3.1. Nanoindentation

Fig. 2 shows representative hardness-depth curves from indentation tests performed at 50°C and 250°C. These exhibit the commonly-observed indentation size effect, with a higher hardness towards smaller depths. To compare the hardness across different temperatures and orientations, the value at 500 nm was taken, as at the point the indentation size effect is vanishingly small for all measured orientations and temperatures. These data are given in Fig. 3a and show no clear trends over the studied temperature range. Averaging the hardness values over all temperatures and orientations gives a value of 3.5 ± 0.3 GPa. The indentation modulus was similarly constant within the standard deviation at all temperatures and orientations and amounts to 53.3 ± 4 GPa (Fig. 3b). For determining these values, a mean Poisson ratio of 0.24 was taken based on the values reported elsewhere [63,64].

Fig. 4 shows representative load-displacement curves for the 48°(0001) orientation between 50°C and 250°C revealing serrated flow at all testing temperatures, which decreases with increasing testing temperature. The occurrence of serrated flow causes a relatively high noise level when hardness is evaluated using a continuous stiffness measurement (Fig. 2a for example).

3.2. Slip line analysis

SE images of slip lines formed around the indents were compared to the traces of surface/crystal plane intersections of potential slip planes using the local orientation information from EBSD. This evaluation yields statistical information using a total number of 249 evaluated slip traces on the activation of different slip systems and presents a useful first step to guide and interpret subsequent uniaxial compression experiments [61,62]. Principally, all indents could be sorted into three categories depending on the amount and shape of slip lines around them. At low temperatures, clear and straight slip lines were observed that could unambiguously be correlated with potential crystallographic plane traces (**Fig.** 5, orange, straight lines). With increasing temperature either no slip lines formed (Fig. 5, no markings) or the slip lines followed a curved shape, presumably following the stress field in very narrow steps (Fig. 5, white, curved lines).

In this last case, the error from falsely assigning one slip line increased with a decreasing number of interpretable slip traces. Consequently, only those experiments where at least ten sufficiently straight

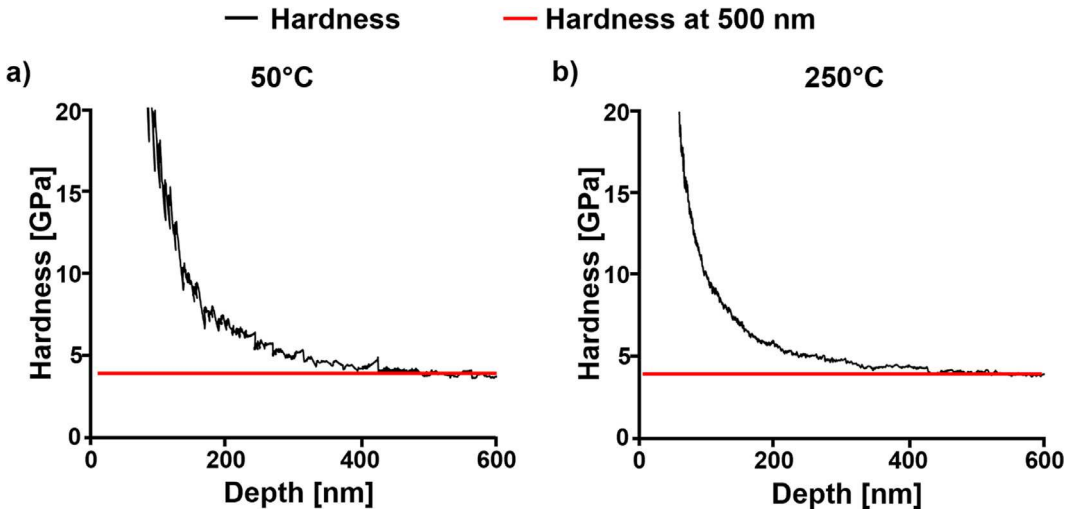

Fig. 2. Hardness with indentation depth for the 48°(0001) oriented grain at 50°C (a) and 250°C (b). The red line displays the average hardness value at 500 nm.

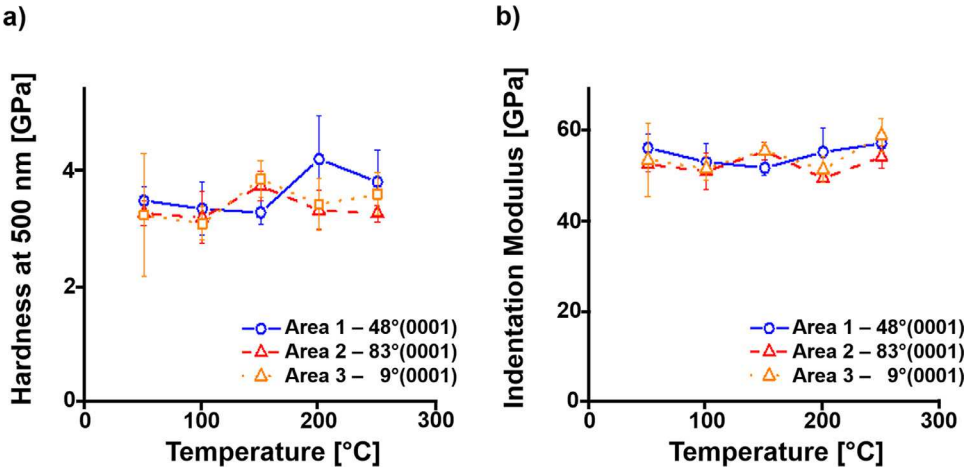

Fig. 3. a) Hardness at 500 nm and b) indentation modulus for all three orientations and temperatures between 50°C and 250°C including their standard deviation.

slip trace segments could be identified in total for each orientation were analysed further.

Fig. 6 shows the glide planes to which the slip lines were assigned for the 83° and 48°(0001) grain orientations that could be analysed as a function of temperature. Also included are CRSS values for each slip system which were determined via micropillar compression, as discussed later.

In the 83°(0001) oriented grain (red data points), the relative frequency of activation of basal slip traces first increased slightly, but then decreased to zero at temperatures above 100°C. The relative frequency of activation of 1st order prismatic slip traces decreased from 15% to 8% between room temperature and 200°C. The relative frequency of activation of 2nd order pyramidal and 2nd order prismatic slip traces stayed constant at around 40% and 10%, respectively. The fraction of 1st order pyramidal slip traces fluctuated around a value of 35%, but overall slightly increased with temperature.

In the grain with 48°(0001) orientation (blue data points), similar trends were seen: the occurrence of basal slip decreased with temperature, vanishing at 150°C. The relative frequency of activation of 1st order prismatic slip traces decreased slightly, from 26% at room temperature to 20% at 150°C, and similar to the 83°(0001) oriented grain, the fraction of 2nd order prismatic slip traces remained constant. Differences between the two grains occurred regarding the pyramidal slip systems. In the 48°(0001) orientation, the relative frequency of activation of 1st order pyramidal slip traces stayed constant with 33% up to a temperature of 100°C and then decreased to 20% at 150°C, while the relative frequency of activation of the 2nd order pyramidal slip traces increased sharply from 32% at room temperature to 50% at 150°C.

3.3. Micropillar compression

A total of seventeen micropillars were compressed and found to deform plastically within the course of this study. Eleven micropillars were compressed at 150°C and six at 250°C within the three differently orientated grains. For each orientation and temperature, one representative compressed micropillar including its simulated slip plane and engineering stress strain curve is given in Fig. 7. Note that for the 9°(0001) orientation, due to experimental difficulties, no micropillar analysis could be conducted at 250°C. The number of pillars exhibiting the indicated slip planes are given in Fig. 8 for each grain orientation.

The 48°(0001) oriented micropillars showed slip planes corresponding predominately to the basal plane for both elevated temperatures, which has a high Schmid factor of 0.49. However, slip on the 1st order prismatic and 1st and 2nd order pyramidal planes was also observed.

For the 83°(0001) orientated pillars, some pillars slipped along the basal and 1st order prismatic plane at ambient temperature, but more pyramidal slip was observed for all temperatures. Despite its high Schmid factor of 0.48, prismatic slip was only activated for two pillars.

For the 9°(0001) orientated micropillars, the activated slip planes correspond to the pyramidal slip systems, which also have the highest Schmid factor of 0.47 to 0.49. For the 9°(0001) orientation at ambient temperature, one pillar slipped on the 1st order pyramidal plane, vs two

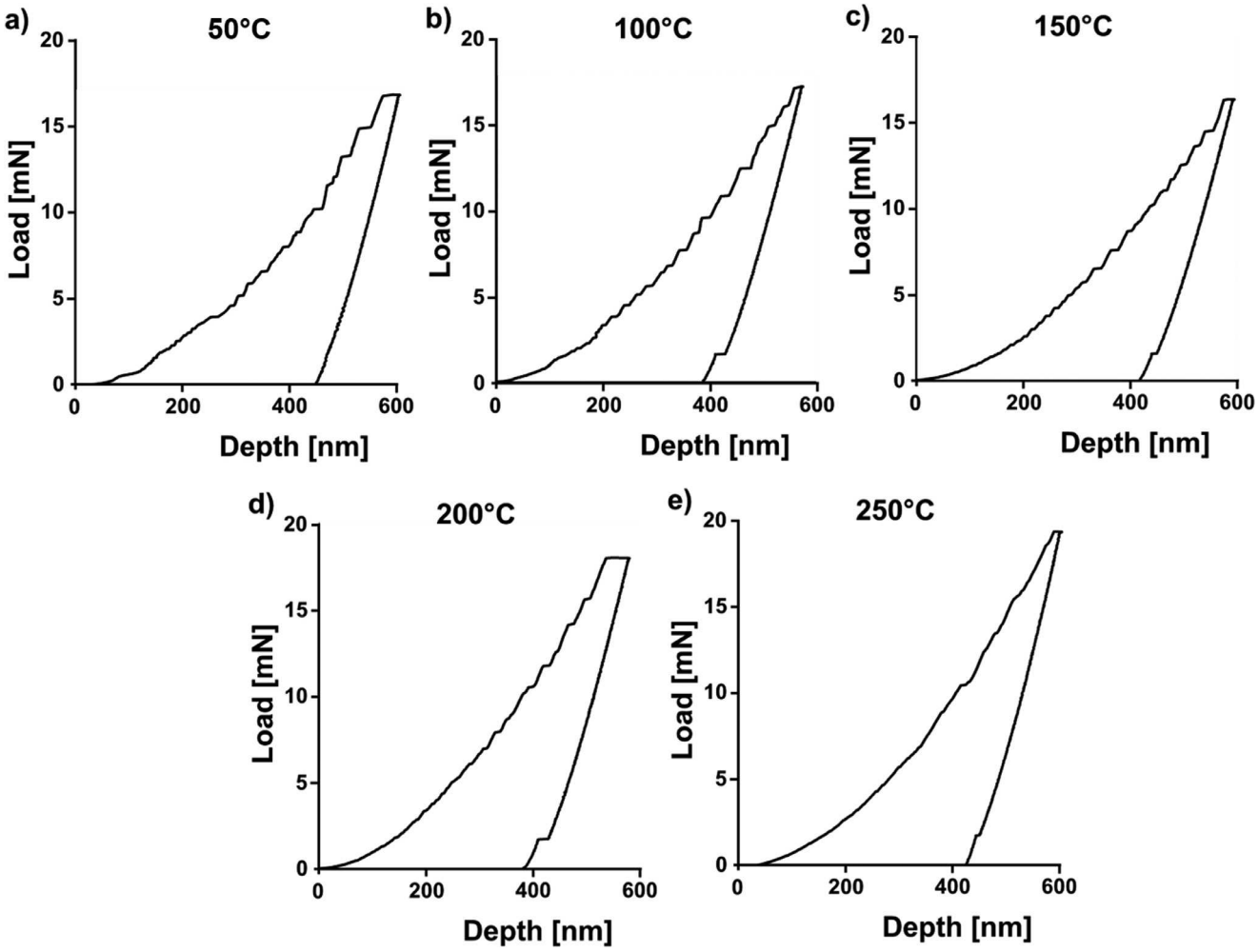

Fig. 4. Load-displacement curves performed under a constant strain rate of approximately 0.04 s^{-1} from the 48°(0001) oriented grain at 50°C (a), 100°C (b), 150°C (c), 200°C (d) and 250°C (e). Tests were performed until a limit of 600 nm was reached. At low temperatures, plastic instabilities are visible, which decrease with increasing temperature and almost vanish at 250°C.

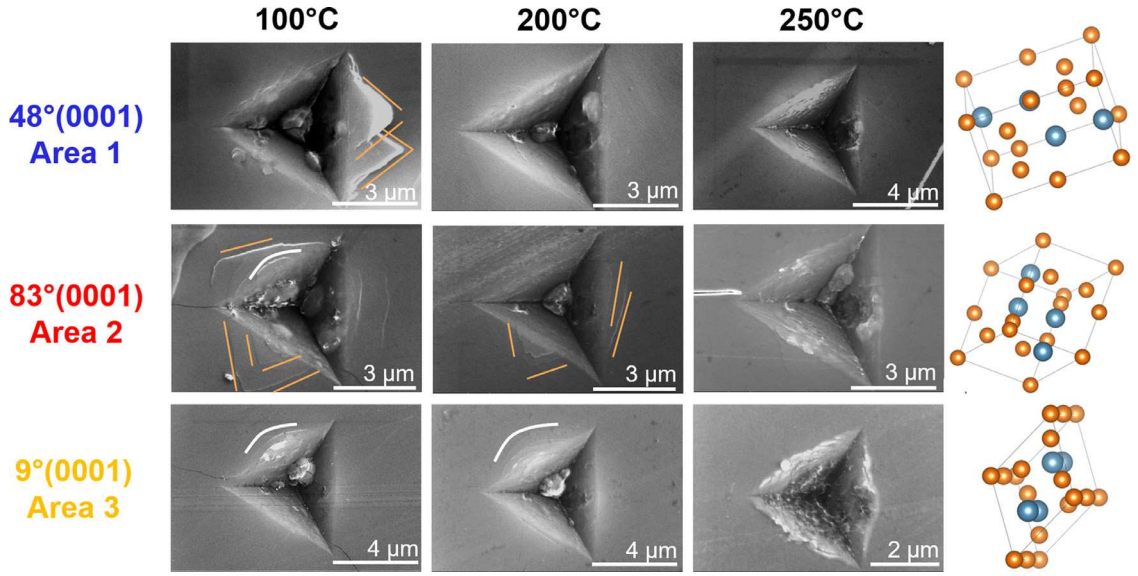

Fig. 5. SE images of indents performed at 100°C, 200°C and 250°C for all three orientations, as depicted on the right. Three different kinds of slip lines were observed: clear, straight lines (orange lines, e.g. 83°(0001) at 100°C and 200°C), no slip lines (e.g. 48°(0001) at 200°C and 250°C) and curved slip lines, presumably following the stress field in narrow steps (white, curved lines, e.g. 9°(0001) at 100°C and 200°C).

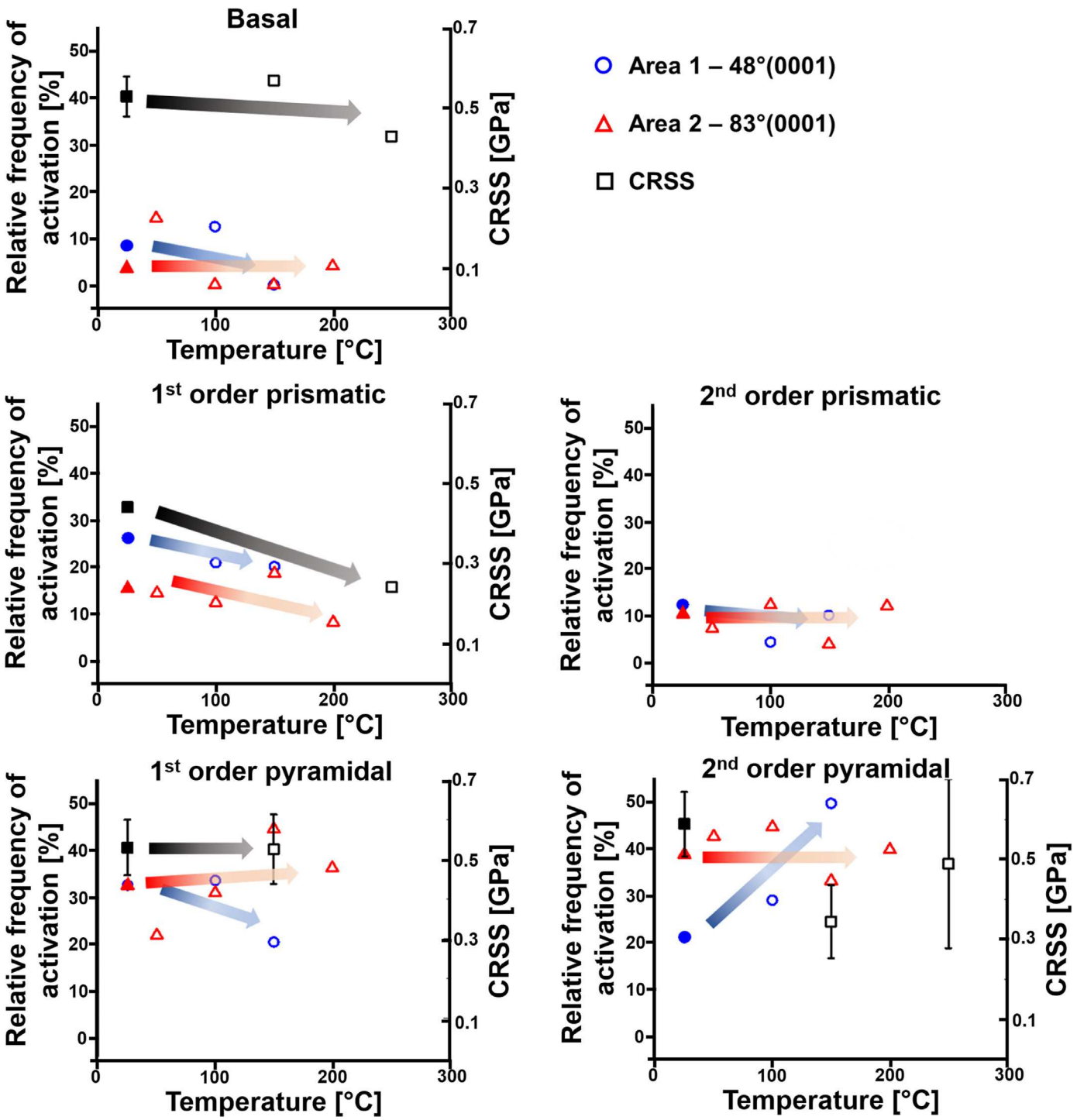

Fig. 6. Relative frequency of activation of different slip planes determined from the slip traces analysis in nanoindentation experiments for the 83°(0001) (red triangles) and 48°(0001) (blue circles) oriented grains at different temperatures. These data points refer to the left axis and the trends are highlighted by the same-coloured arrows. The CRSS values determined by micropillar compression are displayed in black squares and refer to the right axis. The filled symbols are room temperature data taken from reference [59] whereas all open symbols represent data from this work.

pillars on the 2nd order pyramidal plane, whereas at 150°C, three pillars slipped on the 1st order pyramidal plane and one pillar on the 2nd order pyramidal plane.

Consequently, CRSS values spanning the entire range of testing temperatures could only be determined for slip on 2nd order pyramidal and basal planes, shown by the black squares in Fig. 6.

4. Discussion

The hardness as well as the indentation modulus were measured for different temperatures and different orientations, see Fig. 3. Both only varied within the standard deviation over all measured temperatures. The hardness at 500 nm of 3.5 ± 0.3 GPa for temperatures between

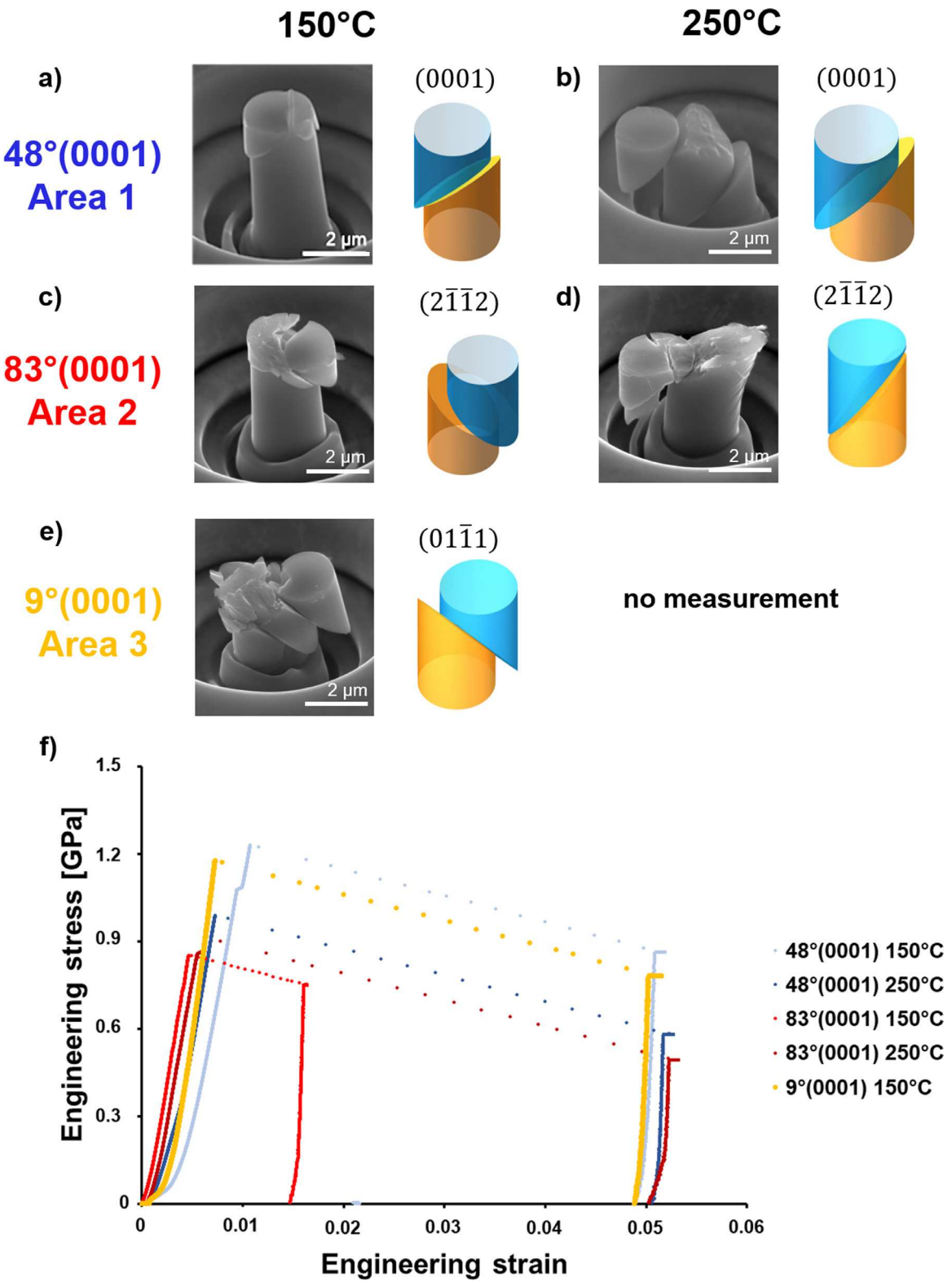

Fig. 7. a-e) SE-images of typical compressed micropillars for all three investigated orientations including the simulated slip planes for the same orientation. f) Representative stress-strain curves for different orientations and temperatures are also given. In almost all cases the loading is perfectly elastic until the critical stress is reached, after which uncontrolled deformation occurs (due to the use of a load-controlled nanoindenter) until the flat punch arrests at the bottom of the trench around the pillar, at approximately 5% strain.

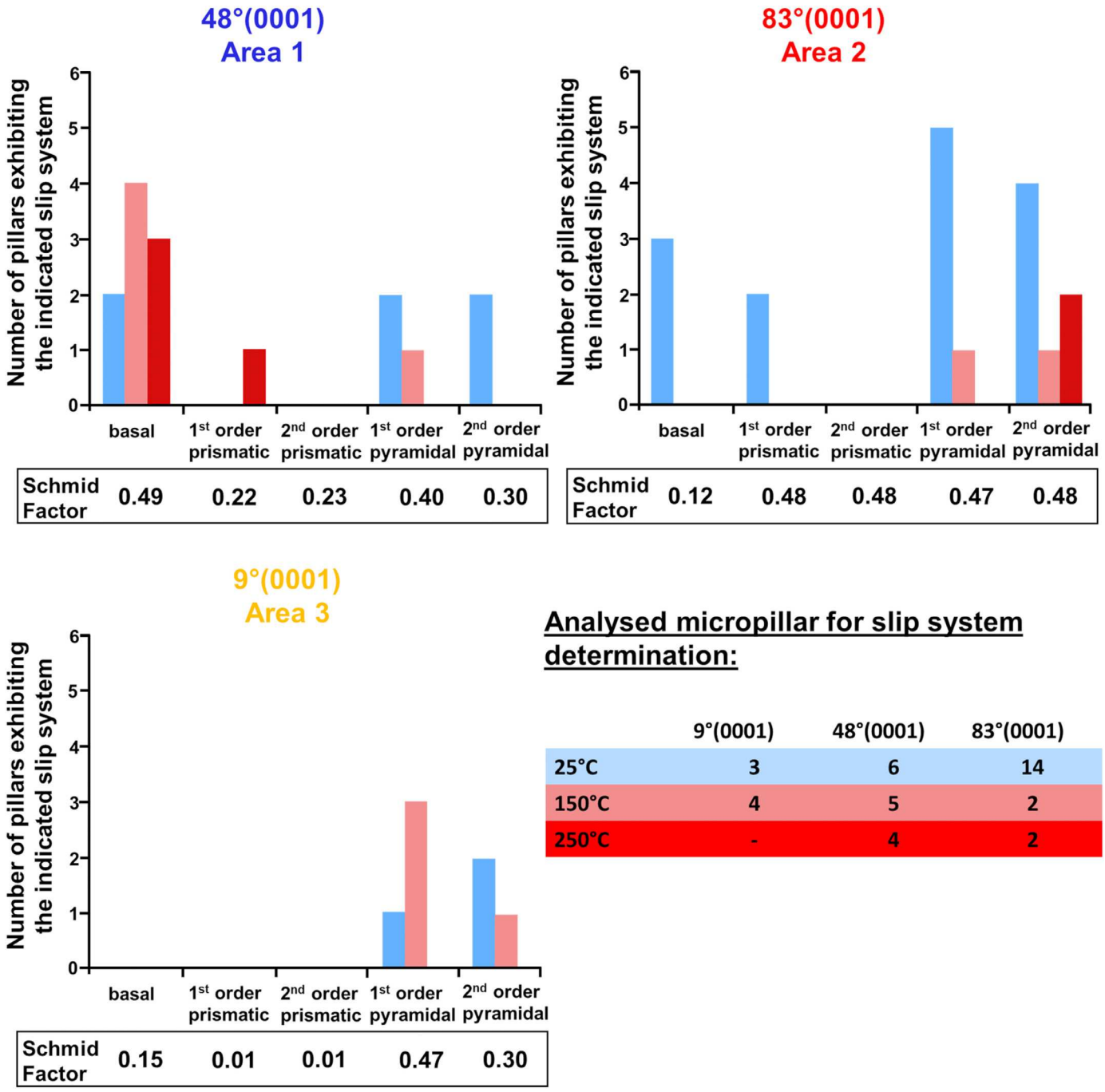

Fig. 8. Number of pillars exhibiting the indicated slip system in microcompression for all three orientations at different testing temperatures and their corresponding Schmid factors. The room temperature data have been taken from reference [59] and are represented in blue for each orientation.

50 and 250°C is in agreement with the authors' previously published ambient temperature hardness of 3.4 ± 0.2 GPa measured at the same indentation depth [59]. Furthermore, no strong effect of the crystallographic orientation occurred. Similar investigations on the hardness of the $CaMg_2$ phase over a vast range of temperatures were also performed by Kirsten et al. [22]. They measured the Brinell hardness from ambient temperature up to 800 K and reported a transition temperature above which the hardness decreased significantly. This transition temperature was found to be 0.59^*T_m. Since our results only cover the temperature range of 0.33^*T_m – 0.53^*T_m, they are below the transition temperature, and therefore our observed constant hardness trend is similar to the reported results by Kirsten et al. [22], who observed a loss in hardness of about 10 percent in a temperature range from 0.25^*T_m _ 0.59^*T_m.

However, the isotropy of our hardness values differs from results reported by Kirsten [65]. He found both anisotropic and lower microhardness values of 2.23 ± 0.06 and 1.87 ± 0.06 for (0001) and $(10\bar{1}1)$ oriented crystals, respectively. These are reasonably comparable orientations to Area 3 - 9°(0001) and Area 1 - 48°(0001). While the lower values are likely attributable to the indentation size effect, the anisotropy is difficult to explain. This might occur due to compositions deviating from stoichiometry, or possible alignment of the microindenter to activate specific slip systems. However, these exact details are unfortunately not available in the cited work. In a recently published work by Luo et al. [37], the orientation dependence of the hardness of the C14 $NbCo_2$ phase was also investigated using nanoindentation. They reported an increased hardness of about 5% for orientations close to (0001) compared

to the other investigated orientations. This much smaller variation compared to the results from Kirsten [65] corresponds to ~0.18 GPa, well within the scatter of the results given here. Luo et al. [37] also report that deformation behaviour only changes when the composition approaches a phase boundary (i.e. C14/C15 or C14/C36). Whether this is related to the exact composition – $NbCo_2$ compared to $CaMg_2$ – remains a subject of further investigation.

Similar to the hardness trend observed within our study, the measured indentation modulus neither varied significantly with temperature nor with crystallographic orientation. The average value over all temperatures and orientations was calculated to be 53.3 ± 4 GPa and is in good agreement with DFT calculations by Yu et al. [66] who calculated an elastic modulus of 55.74 GPa at 0K. The invariance of modulus with temperature observed here likely contributes to the agreement between the experimental data and these calculations.

4.1. Serrated yielding

It is further under discussion how an off-stoichiometric composition might affect the deformation behaviour of Laves phases [28,30-33]. So far, it is known that the dislocation velocity as well as the initial dislocation density can be affected by the chemical composition [31,67]. One reasonable explanation for the lowered dislocation velocity with increasing off-stoichiometry proposed by Kubsch is that off-stoichiometry might hinder the free motion of dislocation kinks and thus reduce the mobility of dislocations, which is indeed observed [31]. The dislocation velocity was further found to increase with increasing temperature due to thermally activated mechanisms [31]. Moreover, specimens with off-stoichiometric compositions are reported to have a higher dislocation density prior to deformation. This is assumed to be due to internal stresses induced by anti-site defects, i.e. substitutional solute atoms [67–69].

The $CaMg_2$ Laves phase investigated within this study has a 2 at.-% higher Mg content than the stoichiometric composition and contains aluminium as an impurity element (0.24 wt.-%), which would be expected to also occupy the same sites as the Mg atoms. It is therefore likely that the phase contains a high number of initial dislocations which move at a low velocity at ambient temperature. This, together with the excess Mg is the ideal prerequisite for serrated yielding, where solute atoms might hinder dislocation motion by pinning free dislocation segments.

With increasing temperature, the dislocation velocity as well as the diffusivity of solute atoms is increased, which lowers the pinning effects. In order to visualise the loss in displacement jumps, the number of observed displacement jumps is evaluated as function of temperature for all three investigated orientations (Fig. 9). Our findings indicate that in the investigated $CaMg_2$ phase solute atoms govern the movement of dislocations below the transition temperature at $0.59^{*}T_M$.

The off-stoichiometric crystallisation of the $CaMg_2$ phase is not surprising. It has already been reported by Stein et al. [58] that in systems where cubic and hexagonal polytypes are present at the same temperature (as in the Mg-Al-Ca system), the C15 phase usually forms at the stoichiometric composition while the C14 (investigated here) and the C36 phase crystallise off-stoichiometrically.

For the sake of completeness, we point out that the determined composition of 68.7 ± 0.5 at.-% Mg is subject to the typical systematic errors in EDX measurement accuracy [70,71]. Therefore, the exact extent as to which the sample is off-stoichiometric is impossible to quantify solely with this technique. Other techniques, such as atom probe tomography, are correspondingly much more involved and beyond the scope of this work. However, we are nevertheless confident that the sample is off-stoichiometric. As standardless EDX quantification, as performed here, can approach an accuracy of ±2% [72], our EDX measurements are above the threshold at which off-stoichiometry is present (i.e. the true composition lies between 68.7 at.% ±2%). This, in combination with previous, more detailed investigations on the off-stoichiometry of Laves phases [28,30-33,67], corroborates the assumption that the material tested in this study deviates from the exact stoichiometric composition and that plasticity in the $CaMg_2$ phase is strongly affected by the excess Mg atoms or trace Al atoms on presumably the same sites, i.e. the presence of solute atoms in the low temperature regime.

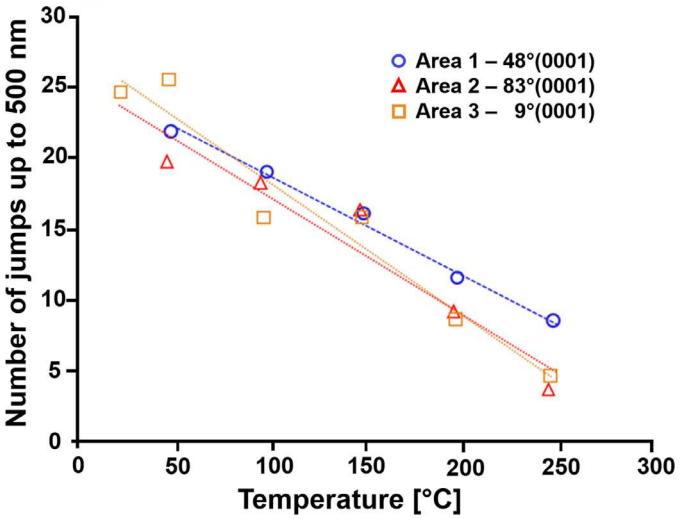

Fig. 9. Extent of serrated flow as a function of temperature for the three orientations. As a measure, the number of displacement jumps that occurred up to a depth of 500 nm is taken. The number of serrations diminishes with increasing temperature.

4.2. Slip line analysis

The slip line analysis showed a decreasing number of identifiable slip lines on the sample surface with increasing temperature for all orientations. Possible explanations of this effect could be surface oxidation, indenter orientation effects, dislocation climb, thermally activated cross-slip or an increase in the homogeneity of slip. We assume that surface oxidation does not play a significant role in the observed loss in slip traces during the elevated temperature deformation as the experiments were conducted under high vacuum (10^{-5} Pa) and surface features (e.g. within the indent) are still clear (Fig. 5).

We also assume that the orientation of the indenter faces with respect to the grain orientation also does not play a strong role in these materials. This relative orientation was not controlled between the data presented here at high temperature and that previously published at room temperature (Fig. 6 open and closed symbols), yet the data form consistent trends. Additionally, in studies of indenter orientation on deformation [73], deformation strongly confined to one face of the residual impression is reported. No such phenomenon has been observed in any of the indents in these materials in SE/BSE imaging. This might be related to deformation here forming discrete slip lines, rather than homogenous pile-up, but it remains to be explored.

Regarding dislocation climb, a similar loss in slip steps was already reported by Mathur et al. [21] around indents in the intermetallic $Mg_{17}Al_{12}$ phase. However, in their study, this activation of dislocation climb was accompanied not only by a change in dislocation structures without concentration on individual planes but also by a significant change in the strain rate sensitivity and a pronounced drop in hardness with temperature. These effects were not found for the $CaMg_2$ Laves phase studied here in the temperature range between 50°C and 250°C.

The third possibility of thermally activated cross-slip of screw dislocations causing a loss of slip lines at the sample surface was studied via TEM investigations on an ambient temperature indent and an indentation test performed at 250°C (Fig. 10). These investigations showed that the dislocation structures are similar for samples deformed at 25°C and 250°C. A change of the dominant slip system can be seen, but no sig-

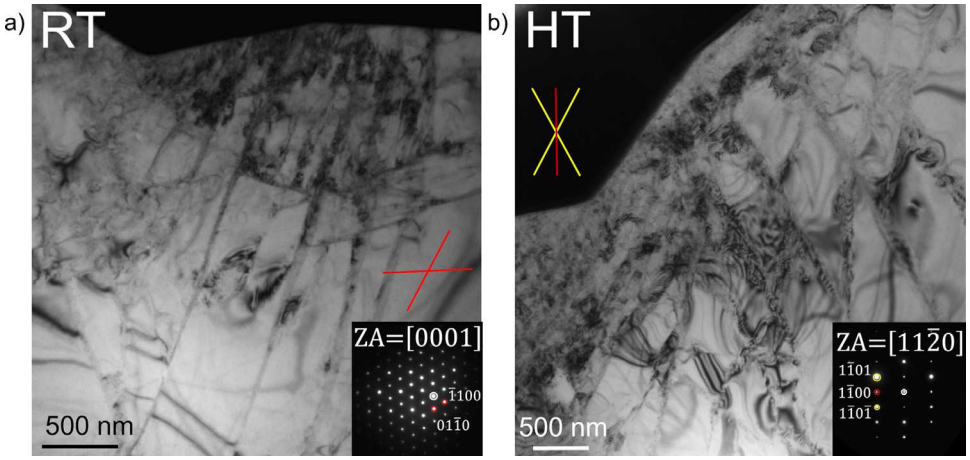

Fig. 10. TEM images of $CaMg_2$ samples deformed at room temperature (a) and 250°C (b). The orientation of $\{1\bar{1}00\}$ and $\{1\bar{1}01\}$ plane traces is indicated by the red and yellow lines respectively, based on the position of the corresponding diffraction spots in the inset selected area diffraction patterns with [0001] and $[11\bar{2}0]$ zone axis (ZA).

nificant change in dislocation structure is visible. Therefore, the results suggest no occurrence of cross-slip up to 250°C.

It seems most likely, therefore, that the activation of further slip systems (Fig. 6) together with a reduction in the amount of serrated yielding (Fig. 9) leads to less localised deformation and consequently less pronounced slip steps. Since the CRSS of slip systems can change with temperature, as discussed in the next section, the activation of further slip systems might lead to more evenly-distributed slip between a larger number of available slip systems, which consequently reduces the visibility of distinct slip traces. Furthermore, a decrease of localised deformation due to a diminishing amount of serrated yielding effect might result in more homogeneous deformation, as also reported by Klose et al. [74].

The relative frequency of activation of slip on different slip planes and their temperature-dependence was measured, though restricted to the 48°(0001) and 83°(0001) grains due to the rapid loss of visible slip lines in the 9°(0001) grain.

For the 48°(0001) orientation, basal slip has the highest Schmid factor of 0.49 and 1st order pyramidal slip also has a high Schmid factor of 0.4. For the 83°(0001) orientation, all prismatic and pyramidal slip systems have high Schmid factors of 0.47 - 0.48. The relative frequency of activation of basal slip was slightly higher for the 48°(0001) orientation than for the 83°(0001) orientation. A higher relative frequency of activation of the slip systems with higher Schmid factor can also be found for the 1st order pyramidal and 2nd order pyramidal slip systems, corresponding to the 83°(0001) orientation. However, for the 1st and 2nd order prismatic planes, this trend was not seen. This might be related to the sufficient accommodation of the induced strain by the activation of the pyramidal slip systems already.

A quantitative comparison of the relative frequency of activated slip planes between all slip systems can however not be easily drawn, as the anisotropy of the hexagonal unit cell and the consequently different numbers of equivalent slip planes need to be taken into account here too (see reference [59] for further details).

Furthermore, CRSS values for basal, 1st order prismatic and 1st and 2nd order pyramidal slip are given. However, due to the small number of compressed micropillars, no general conclusion on the development of the CRSS with temperature can be drawn.

Quantitative measurements of CRSS using micropillar compression are difficult due to the limited amount of data points over the range of orientation and temperature. However, these results suggest that basal and 1st order prismatic slip show a decreasing CRSS with temperature, whereas 1st and 2nd order pyramidal slip do not show significant changes.

Paufler et al. found that the lattice resistance due to the Peierls barrier for basal and prismatic slip is of the same magnitude at a temperature of 390°C [27]. Additionally, they found that most dislocations present after high temperature deformation were on the basal or prismatic planes [27], albeit in single crystals aligned for this purpose. However, the specific alignment as well as the different testing temperatures used compared to our tests, impede a direct comparison.

So far, the occurrence of basal slip was often reported after macroscopic elevated temperature tests on the C14 phase [23,25,27,31,33,41,47]. However, hardness tests on the $MgZn_2$ phase also revealed the basal plane as predominant slip plane at temperatures between room temperature and 500 K [22] and basal slip was found after ambient temperature indentation tests by Takata et al. [39]. Luo et al. [36] observed basal and non-basal slip by compressing $NbCo_2$ micropillars, which is consistent with our findings, where basal slip was found after nanoindentation as well as microcompression at all temperatures if the Schmid factor was high.

Prismatic slip was also mostly reported to occur at elevated temperatures (above 390°C) in macroscopic tests in the C14 phase [27,32,47]. However, a study by Kirsten et al. [22] on the $CaMg_2$ phase, which is also investigated here, reported 1st order prismatic slip after ambient temperature hardness tests. And indeed, slip traces corresponding to the 1st order prismatic planes were also observed for both, the 48°(0001) orientation and the 83°(0001) orientation, within our study. Micropillars in the 83°(0001) orientation, have a high Schmid factor of 0.48 for 1st order prismatic slip, and this system was also observed in ambient temperature micropillar compression.

Interestingly, 1st order prismatic slip could also be activated for the 48°(0001) orientation at 250°C even though the Schmid factor was as low as 0.22. However, if the decreasing CRSS of 1st order prismatic slip with increasing temperature (Fig. 7) is considered, the occurrence of 1st order prismatic slip at 250°C can be explained, suggesting that this slip system is thermally activated.

Slip on the 1st and 2nd order pyramidal plane in the C14 phase is, to the authors' best knowledge, only reported to occur above 500°C [47]. However, the lack of reported pyramidal slip at lower temperatures might also be a result of the limited number of studies on ambient temperature deformation of the C14 Laves-phases.

5. Conclusions

The deformation behaviour of the $CaMg_2$ C14 Laves phase at temperatures between 50°C and 250°C (0.33^*T_m – 0.53^*T_m) was investigated for different grain orientations. In-situ nanoindentation in conjunction with SE, EBSD and TEM imaging allowed an analysis of the deformation behaviour in various aspects:

- The average hardness and indentation modulus over all temperatures were 3.5 ± 0.3 GPa and 53.4 ± 4 GPa, respectively, with negligible anisotropy or temperature sensitivity.

- Up to 200°C, serrated yielding was observed in the indentation curves, which decreased with increasing temperature. This is associated with solute atoms governing the dislocation mobility by pinning slipping dislocation segments.
- The activation of different slip systems from nanoindentation was evaluated in a statistical manner between 50°C and 250°C. The number of identifiable slip traces around indents and the number of serrations decreased with increasing temperature, which is assumed to be due to the activation of additional slip systems at elevated temperatures together with a decreasing effect of solute atoms.
- CRSS values were determined by micropillar compression experiments for basal, 1st order prismatic and pyramidal as well as 2nd order pyramidal slip. While the data should be interpreted with caution due to the limited number of pillars, the results initially suggest that basal and 1st order prismatic slip show a decreasing CRSS with temperature, whereas 1st and 2nd order pyramidal slip do not show significant changes.

Declaration of Competing Interest

None.

Acknowledgement

The authors gratefully acknowledge the financial support of the Deutsche Forschungsgemeinschaft (DFG) within project A05 of the Collaborative Research Center (SFB) 1394 “Structural and Chemical Atomic Complexity - from defect phase diagrams to material properties” – project number 409476157. This project has received funding from the European Research Council (ERC) under the European Union’s Horizon 2020 research and innovation programme (grant agreement No. 852096 FunBlocks).

References

[1] Y. Terada, et al., A thousandfold creep strengthening by Ca addition in die-cast AM50 magnesium alloy, Metall. Mater. Trans. A 35 (9) (2004) 3029–3032.
[2] W. Qudong, et al., Effects of Ca addition on the microstructure and mechanical properties of AZ91magnesium alloy, J. Mater. Sci. 36 (12) (2001) 3035–3040.
[3] T. Sato, M.V. Kral, Microstructural evolution of Mg–Al–Ca–Sr alloy during creep, Mater. Sci. Eng.: A 498 (1–2) (2008) 369–376.
[4] M. Vogel, O. Kraft, E. Arzt, Creep behavior of magnesium die-cast alloy ZA85, Scr. Mater. 48 (8) (2003) 985–990.
[5] N.D. Saddock, et al., Grain-scale creep processes in Mg–Al–Ca base alloys: Implications for alloy design, Scr. Mater. 63 (7) (2010) 692–697.
[6] T. Rzychoń, Characterization of Mg-rich clusters in the C36 phase of the Mg–5Al–3Ca–0.7Sr–0.2Mn alloy, J. Alloys Compd. 598 (0) (2014) 95–105.
[7] A. Luo, B.R. Powell, M. Balogh, Creep and microstructure of magnesium-aluminum–calcium based alloys, Metall. Mater. Trans. A 33 (3) (2002) 567–574.
[8] B. Backes, et al., Particle Hardening in Creep-Resistant Mg-Alloy MRI 230D Probed by Nanoindenting Atomic Force Microscopy, Metall. Mater. Trans. A 40 (2) (2009) 257–261.
[9] D. Amberger, P. Eisenlohr, M. Göken, Microstructural evolution during creep of Ca–containing AZ91, Mater. Sci. Eng.: A (0) (2009) 398–402 510–511.
[10] H. Cao, et al., Experiments coupled with modeling to establish the Mg-rich phase equilibria of Mg–Al–Ca, Acta Mater. 56 (18) (2008) 5245–5254.
[11] A. Suzuki, et al., Precipitation Strengthening of a Mg-Al-Ca–Based AXJ530 Die-cast Alloy, Metall. Mater. Trans. A 39 (3) (2008) 696–702.
[12] H. Eibisch, et al., Effect of solidification microstructure and Ca additions on creep strength of magnesium alloy AZ91 processed by Thixomolding, Int. J. Mater. Res. 99 (1) (2008) 56–66.
[13] M.P. Liu, et al., Mechanical Properties and Creep Behavior of Mg–Al–Ca Alloys, Mater. Sci. Forum 488 (2005) 763–766.
[14] D. Amberger, P. Eisenlohr, M. Göken, On the importance of a connected hard-phase skeleton for the creep resistance of Mg alloys, Acta Mater. 60 (5) (2012) 2277–2289.
[15] M. Zubair, et al., On the role of Laves phases on the mechanical properties of Mg-Al-Ca alloys, Mater. Sci. Eng.: A 756 (2019) 272–283.
[16] S. Amerioun, S.I. Simak, U. Häussermann, Laves-Phase Structural Changes in the System CaAl2-xMgx, Inorg. Chem. 42 (5) (2003) 1467–1474.
[17] E. Deligoz, et al., The first principles investigation of lattice dynamical and thermodynamical properties of Al2Ca and Al2Mg compounds in the cubic Laves structure, Comput. Mater. Sci. 68 (0) (2013) 27–31.
[18] J. Gröbner, et al., Experimental investigation and thermodynamic calculation of ternary Al–Ca–Mg phase equilibria, Z. Metallkd. 94 (9) (2003) 976–982.
[19] S.M. Liang, et al., Thermal analysis and solidification pathways of Mg–Al–Ca system alloys, Mater. Sci. Eng.: A 480 (1–2) (2008) 365–372.
[20] A. Suzuki, et al., Structure and transition of eutectic (Mg,Al)2Ca Laves phase in a die-cast Mg–Al–Ca base alloy, Scr. Mater. 51 (10) (2004) 1005–1010.
[21] H.N. Mathur, V. Maier-Kiener, S. Korte-Kerzel, Deformation in the γ-Mg17Al12 phase at 25–278°C, Acta Mater. 113 (2016) 221–229.
[22] C. Kirsten, P. Paufler, G. Schulze, Zur plastischen Verformung intermetallischer Verbindungen, Monatsber Dt Akad Wiss Berlin 6 (2) (1964) 140–147.
[23] D. Hinz, P. Paufler, G. Schulze, Temperature change experiments during secondary creep of the intermetallic compound MgZn2, Phys. Status Solidi 36 (2) (1969) 609–615.
[24] U. Krämer, G. Schulze, in: Gittergeometrische Betrachtung der plastischen Verformung von Lavesphasen, 3, Kristall und Technik, 1968, pp. 417–430.
[25] P. Paufler, G. Schulze, Plastic deformation of the intermetallic compound MgZn2, Phys. Status Solidi 24 (1) (1967) 77–87.
[26] P. Paufler, J. Marschner, G.E.R. Schulze, The Mobility of Grown-in Dislocations in the Intermetallic Compound MgZn2 I. Stress Dependence for Edge Dislocations in Prism Slip at 390°C, Phys. Status Solidi 40 (2) (1970) 573–579.
[27] P. Paufler, J. Marschner, G.E.R. Schulze, The mobility of grown-in dislocations in the intermetallic compound MgZn2 II. Stress dependence of basal slip at 390°C, Physica Status Solidi 43 (1) (1971) 279–282.
[28] T.H. Mueller, P. Paufler, Yield strength of the monocrystalline intermetallic compound MgZn2, Phys. Status Solidi 40 (2) (1977) 471–477.
[29] P. Paufler, Deformation-mechanism maps of the intermetallic compound MgZn2, Krist. Tech. 13 (5) (1978) 587–590.
[30] P. Paufler, Early work on Laves phases in East Germany, Intermetallics 19 (4) (2011) 599–612.
[31] H. Kubsch, P. Paufler, G. Schulze, The Mobility of Grown-in Dislocations in the Intermetallic Compound MgZn2. III. Dependence of Basal Slip on Chemical Composition within the Homogeneity Range and on Temperature, Phys. Status Solidi 56 (1) (1973) 231–234.
[32] H. Kubsch, P. Paufler, G. Schulze, The mobility of grown-in dislocations in the intermetallic compound MgZn2 during prismatic slip, Phys. Status Solidi 25 (1) (1974) 269–275.
[33] T. Müller, et al., Gleitbanduntersuchungen während und nach Verformung der intermetallischen Verbindung MgZn2, Krist. Tech. 7 (11) (1972) 1249–1264.
[34] J. Livingston, E. Hall, E. Koch, Deformation and Defects in Laves Phases, MRS Online Proc. Lib. Arch. (1988) 133.
[35] N. Takata, et al., Effect of Dislocation Sources on Slip in Fe2Nb Laves Phase with Ni in Solution, MRS Proc. 1516 (2012) 269–274.
[36] W. Luo, et al., Crystal structure and composition dependence of mechanical properties of single-crystalline NbCo2 Laves phase, Acta Mater. 184 (2020) 151–163.
[37] W. Luo, et al., Composition dependence of hardness and elastic modulus of the cubic and hexagonal NbCo2 Laves phase polytypes studied by nanoindentation, J. Mater. Res. 35 (2) (2020) 185–195.
[38] J. Guénolé, et al., Basal slip in Laves phases: the synchroshear dislocation, Scr. Mater. 166 (2019) 134–138.
[39] N. Takata, et al., Nanoindentation study on solid solution softening of Fe-rich Fe2Nb Laves phase by Ni in Fe–Nb–Ni ternary alloys, Intermetallics 70 (2016) 7–16.
[40] L. Machon, G. Sauthoff, Deformation behaviour of Al-containing C14 Laves phase alloys, Intermetallics 4 (6) (1996) 469–481.
[41] S. Voß, Mechanische Eigenschaften von Laves-Phasen in Abhängigkeit von Kristallstruktur und Zusammensetzung am Beispiel der Systeme Fe–Nb–Al und Co–Nb, RWTH Aachen, Aachen, Germany, 2011.
[42] N. Takata, et al., Plastic deformation of the C14 Laves phase (Fe,Ni)2Nb, Scr. Mater. 68 (8) (2013) 615–618.
[43] S.M. Allen, Technical Progress Report: August 1, 1990 - January 31, 1997, MIT, Departement of Materials Science and Engineering, 1998.
[44] Y. Liu, S.M. Allen, J.D. Livingston, Deformation Mechanisms in a Laves Phase, MRS Proc. (1992) 288.
[45] Y. Liu, J.D. Livingston, S.M. Allen, Room-temperature deformation and stress-induced phase transformation of laves phases in Fe-10 At. Pct Zr alloy, Metall. Trans. A 23 (12) (1992) 3303–3308.
[46] Y. Liu, S.M. Allen, J.D. Livingston, Deformation of two C36 laves phases by microhardness indentation at room temperature, Metall. Mater. Trans. A 26 (5) (1995) 1107–1112.
[47] P. Paufler, G. Schulze, Gleitsysteme innermetallischer verbindungen, Krist. Tech. 2 (4) (1967) K11–K14.
[48] P. Paufler, G.E. Schulze, Zur Zwillingsbildung in MgZn2, Krist. Tech. 2 (2) (1967) 231–244.
[49] A. Kazantzis, et al., The mechanical properties and the deformation microstructures of the C15 Laves phase Cr2Nb at high temperatures, Acta Mater. 55 (6) (2007) 1873–1884.
[50] A. Kazantzis, M. Aindow, I. Jones, Deformation behaviour of the C15 Laves phase Cr2Nb, Mater. Sci. Eng.: A 233 (1–2) (1997) 44–49.
[51] A. Kazantzis, M. Aindow, I. Jones, Stacking-fault energy in the C15 Laves phase Cr2Nb, Philos. Mag. Lett. 74 (3) (1996) 129–136.
[52] T. Müller, Inhomogeneities of the plastic deformation of MgZn2 single crystals, Krist. Tech. 10 (8) (1975) 805–811.
[53] W. Luo, et al., Influence of composition and crystal structure on the fracture toughness of NbCo2 Laves phase studied by micro-cantilever bending tests, Mater. Des. 145 (2018) 116–121.
[54] F. Stein, A. Leineweber, Laves phases: a review of their functional and structural applications and an improved fundamental understanding of stability and properties, J. Mater. Sci. 56 (9) (2021) 5321–5427.
[55] A.V. Kazantzis, et al., On the self-pinning character of synchro-Shockley dislocations in a Laves phase during strain rate cyclical compressions, Scr. Mater. 59 (7) (2008) 788–791.

[56] M. Lowry, et al., Achieving the ideal strength in annealed molybdenum nanopillars, Acta Mater. 58 (15) (2010) 5160–5167.
[57] H. Bei, et al., Effects of pre-strain on the compressive stress–strain response of Mo-alloy single-crystal micropillars, Acta Mater. 56 (17) (2008) 4762–4770.
[58] F. Stein, M. Palm, G. Sauthoff, Structure and stability of Laves phases part II—structure type variations in binary and ternary systems, Intermetallics 13 (10) (2005) 1056–1074.
[59] C. Zehnder, et al., Plastic deformation of single crystalline C14 Mg2Ca Laves phase at room temperature, Mater. Sci. Eng.: A 759 (2019) 754–761.
[60] W.C. Oliver, G.M. Pharr, Measurement of hardness and elastic modulus by instrumented indentation: Advances in understanding and refinements to methodology, J. Mater. Res. 19 (1) (2004) 3–20.
[61] S. Schröders, et al., Room temperature deformation in the Fe7Mo6 μ-Phase, Int. J. Plast. 108 (2018) 125–143.
[62] J.S.-L. Gibson, et al., Finding and characterising active slip systems: a short review and tutorial with automation tools, Materials 14 (2) (2021) 407.
[63] P. Mao, et al., First-principles calculations of structural, elastic and electronic properties of AB2 type intermetallics in Mg–Zn–Ca–Cu alloy, J. Magnesium Alloys 1 (3) (2013) 256–262.
[64] M. De Jong, et al., Charting the complete elastic properties of inorganic crystalline compounds, Sci. Data 2 (1) (2015) 1–13.
[65] Kirsten, C., Über Festigkeitseigenschaften intermetallischer Verbindungen- Doctoral thesis in Technical University Dresden. 1963.
[66] W.-Y. Yu, et al., First-principles investigation of the binary AB2 type Laves phase in Mg–Al–Ca alloy: electronic structure and elastic properties, Solid State Sci. 11 (8) (2009) 1400–1407.
[67] K. Eichler, et al., Änderung von Verformungseigenschaften der intermetallischen Verbindung MgZn2 im Homogenitätsbereich, Krist. Tech. 11 (11) (1976) 1185–1188.
[68] J. Zhu, et al., Point defects in binary Laves phase alloys, Acta Mater. 47 (7) (1999) 2003–2018.
[69] J. Zhu, et al., Enthalpies of formation of binary Laves phases, Intermetallics 10 (6) (2002) 579–595.
[70] K.E. MacArthur, et al., Probing the effect of electron channelling on atomic resolution energy dispersive X-ray quantification, Ultramicroscopy 182 (2017) 264–275.
[71] K.E. MacArthur, et al., Quantitative energy-dispersive X-ray analysis of catalyst nanoparticles using a partial cross section approach, Microsc. Microanal. 22 (1) (2016) 71.
[72] P. Pinard, et al., Development and validation of standardless and standards-based X-ray microanalysis, in: IOP Conference Series: Materials Science and Engineering, IOP Publishing, 2020.
[73] S. Jakob, et al., Influence of crystal orientation and Berkovich tip rotation on the mechanical characterization of grain boundaries in molybdenum, Mater. Des. 182 (2019) 107998.
[74] F. Klose, et al., Analysis of portevin-le chatelier serrations of type bin Al–Mg, Mater. Sci. Eng.: A 369 (1–2) (2004) 76–81.